ВІСНИК
КИЇВСЬКОГО НАЦІОНАЛЬНОГО УНІВЕРСИТЕТУ ІМЕНІ ТАРАСА ШЕВЧЕНКА

ISSN 1728-2306

РАДІОФІЗИКА ТА ЕЛЕКТРОНІКА 1(24)/2016

Засновано 1999 року

УДК 517

Публікуються результати експериментальних і теоретичних досліджень у галузях фізичної електроніки, фізики плазми, фізики поверхні твердого тіла, емісійної електроніки, кріогенної та мікроелектроніки, нанофізики та наноелектроніки, високотемпературної надпровідності, квантової радіофізики, функціональної електроніки, твердотільної електроніки, мобільного зв'язку, медичної радіофізики, методів отримання діагностичної інформації та її комп'ютерної обробки.

Для науковців, викладачів вищої школи, студентів.

Публикуются результаты экспериментальных и теоретических исследований в областях физической электроники, физики плазмы, физики поверхности твердого тела, эмиссионной электроники, криогенной и микроэлектроники, нанофизики и наноэлектроники, высокотемпературной сверхпроводимости, квантовой радиофизики, функциональной электроники, твердотельной электроники, мобильной связи, медицинской радиофизики, методов получения диагностической информации и ее компьютерной обработки.

Для научных работников, преподавателей высшей школы, студентов.

Experimental and theoretical contributions are published in the following fields: physical electronics, plasma physics, solid-state surface physics, emission electronics, cryogenic electronics, microelectronics, nanophysics and nanoelectronics, high-temperature supercondactive electronics, solid-state electronics, functional electronics, microwave electronics, quantum electronics, mobile communication, medical radiophysics, methods of receipt and computer processing of diagnosis information.

Designed for researches, university teachers, students.

BULLETIN

TARAS SHEVCHENKO NATIONAL UNIVERSITY OF KYIV

ISSN 1728-2306

RADIO PHYSICS AND ELECTRONICS 1(24)/2016

Established in 1999

УДК 517

Experimental and theoretical contributions are published in the following fields: physical electronics, plasma physics, solid-state surface physics, emission electronics, cryogenic electronics, microelectronics, nanophysics and nanoelectronics, high-temperature supercondactive electronics, solid-state electronics, functional electronics, microwave electronics, quantum electronics, mobile communication, medical radiophysics, methods of receipt and computer processing of diagnosis information

Designed for researches, university teachers, students.

Публікуються результати експериментальних і теоретичних досліджень у галузях фізичної електроніки, фізики плазми, фізики поверхні твердого тіла, емісійної електроніки, кріогенної та мікроелектроніки, нанофізики та наноелектроніки, високотемпературної надпровідності, квантової радіофізики, функціональної електроніки, твердотільної електроніки, мобільного зв'язку, медичної радіофізики, методів отримання діагностичної інформації та її комп'ютерної обробки.

Для науковців, викладачів вищої школи, студентів.

Публикуются результаты экспериментальных и теоретических исследований в областях физической электроники, физики плазмы, физики поверхности твердого тела, эмиссионной электроники, криогенной и микроэлектроники, нанофизики и наноэлектроники, высокотемпературной сверхпроводимости, квантовой радиофизики, функциональной электроники, твердотельной электроники, мобильной связи, медицинской радиофизики, методов получения диагностической информации и ее компьютерной обработки.

Для научных работников, преподавателей высшей школы, студентов.

Address	Faculty of Radio Physics, Electronics and Computer Systems, 4G, Academician Glushkov avenue, Kyiv, 03127, Ukraine ☎ (38 044) 526 05 60
Approved by	The Academic Council of the Faculty of Radio Physics, Electronics and Computer Systems 12.10.15 (Protocol № 3)
Certified by	Resolution of the Presidium of HAC of Ukraine № 1-05/1 of 10.02.10
Registered by	Ministry of Justice of Ukraine. Registration certificate KV № 15797-4269P date 02.10.09
Founded and published	Taras Shevchenko National University of Kyiv, Publishing and Polygrafic center "University of Kyiv" DK № 1103 of 31.10.02
Address of publisher	PPC "Kyiv University" (off. 43), 14, Taras Shevchenko blv., Kyiv, 01601, Ukraine ☎ (38 044) 239 32 22; Fax 239 31 28

ЗМІСТ

Бех І., Новак С.
Аналогова модель нейронної мережі для прогнозування розвитку процесів у часі 6

Богданов Р., Костюкевич О., Стубров Ю., Якимов К.
Розміри вуглецевих нанокристалітів у плівках,
осаджених магнетронним методом на різних підкладках 10

Василенко Д., Григорук В., Сидоренко В.
Оптичне ближньопольове субнанополірування поверхні діелектриків
із використанням фотохімічної реакції 17

Гайдар В., Судаков О., Радченко С.
Детектування епілептичних нападів з використанням стаціонарного вейвлет-перетворення 20

Гандзюк В., Григорук В., Іщук Л., Онисько Ю., Павлюк С., Соломенко О.
Визначення температури розігріву кремнієвої структури з діелектричною ізоляцією 23

Дрозд І., Кузьмичів А., Пинькавський О.
Високовольтний повнокерований газорозрядний тетрод із холодним катодом 26

Мельник І., Чернятинський І., П'ясецька Н.
Ітераційна методика моделювання тріодних електродних систем високовольтного тліючого розряду
з урахуванням температури та рухомості електронів в анодній плазмі 30

Радченко С., Мамілов С., Глєбова І.
Моделювання впливу оптичного випромінювання на зменшення оксигемоглобіну в крові 35

Резчиков С.
Два простих алгоритми автоматизації вимірювань НЧ-шуму 38

Сіжук А.
Поглинальні властивості газів із квантово-оптичним механізмом взаємодії 42

Сулименко О., Прокопенко О.
Числове дослідження фазової синхронізації двох спінтронних магнітних наноосциляторів
із випадковими власними частотами та початковими фазами 46

Тітов Д., Кияшко Ю., Афанас'єва Т., Мамілов С.
Неінвазивний оптоелектронний пристрій для визначення отруєння монооксидом вуглецю 50

Тменова Т., Веклич А., Борецький В.
Калібрування спектральної чутливості спектрометра SDH-IV 54

Хилько О.
Розсіяння поверхневого плазмон поляритону на двовимірній напівпровідниковій наносмужці.
Ефективна сприйнятливість двовимірної наносмужки 61

СОДЕРЖАНИЕ

Бех И., Новак С.
Аналоговая модель нейронной сети для прогнозирования развития процессов во времени 6

Богданов Р., Костюкевич О., Стубров Ю., Якимов К.
Размеры углеродных нанокристаллитов в пленках,
осаженных магнетронным методом на различных положках....10

Василенко Д., Григорук В., Сидоренко В.
Оптическое ближнепольное субнанополирование поверхности диэлектриков
с использованием фотохимической реакции....17

Гайдар В., Судаков О., Радченко С.
Детектирование эпилептических припадков
с использованием стационарного вейвлет-преобразования 20

Гандзюк В., Григорук В, Ищук Л., Онысько Ю., Павлюк С., Соломенко Е.
Определение температуры разогрева кремниевой структуры с диэлектрической изоляцией 23

Дрозд И., Кузьмиче А., Пинькавский А.
Высоковольтный газоразрядный тетрод с полным управлением и холодным катодом 26

Мельник И., Чернятинский И., Пясецкая Н.
Итерацинная методика моделирования триодных электродных систем
высоковольтного тлеющего разряда с учетом температуры
и подвижности электронов в анодной плазме 30

Радченко С., Мамилов С., Глебова І.
Моделирование влияния оптического излучения на уменьшение оксигемоглобина в крови 35

Резчиков С.
Два простых алгоритма автоматизации измерений НЧ-шума 38

Сижук А.
Поглощательные свойства газов с квантово-оптическим механизмом взаимодействия 42

Сулименко О., Прокопенко А.
Численное исследование фазовой синхронизаци двух спинтронных магнитных наноосцилляторов
со случайными собственными частотами и начальными фазами 46

Титов Д., Кияшко Ю., Афанасьева Т., Мамилов С.
Неинвазивное оптоэлектроннное устройство для определения отравления монооксидом углерода 50

Тменова Т., Веклич А., Борецкий В.
Калибровка спектральной чувствительности спектрометра SDH-IV 54

Хилько А.
Рассеяние поверхностного плазмон-поляритона на двумерной полупроводниковой нанополоске.
Эффективная восприимчивость двумерной нанополоски....61

CONTENTS

Bekh I., Novak S.
Analog neural network for prediction of processes in time 6

Bogdanov R., Kostiukevych O., Stubrov Y., Yakimov K.
Carbon nanocrystallites sizes in films deposited by magnetron method on different substrates 10

Vasylenko D., Grygoruk V., Sydorenko V.
Optical near-field sub-nano-polishing the dielectrics surface using photochemical reaction 17

Gaidar V., Sudakov O., Radchenko S.
Detecting epileptic seizures using stationary wavelet transform 20

Gandzyuk V., Grygoruk V., Ishchuk L., Onysko Yu., Pavlyuk S., Solomenko O.
Heating temperature determination of the "silicon structure with dielectric insulation" 23

Drozd I., Kuzmichev A., Pinkavsky A.
High-voltage full-controlled gas discharge cold-cathode tetrode 26

Melnyk I., Chernyatynshkiy I., Piasetska N.
Iteratively methodic of simulation of troide high voltage glow discharge electrodes systems with taking into account the temperature and mobility of slow electrons in anode plasma 30

Radchenko S., Mamilov S., Hliebova I.
Simulation of effects of optical radiation on the oxyhemoglobin reduction in blood 35

Reschikoff S.
Two simple algorithms for automation of LF noise measurements 38

Sizhuk A.
Absorption properties of atoms with the quantum optical interaction 42

Sulymenko O., Prokopenko O.
Numerical study of the phase synchronization of two spin-torque nano-oscillators with random eigen frequencies and initial phases 46

Titov D., Kyiashko Y., Afanasieva T., Mamilov S.
Non-invasive optoelectronic device for determining the toxicity of carbon monoxide 50

Tmenova T., Veklich A., Boretskij V.
Calibration of spectral response of the SDH-IV spectrometer 54

Khylko O.
Scattering of surface plasmon polariton by two-dimensional semiconductor nanostripe. Effective susceptibility of two-dimensional nanostripe 61

UDC 621; 621.37/.39; 621.382.2/.3; 321.387

I. Bekh, Ph. D.,
S. Novak, post. stud.,
Department of Radio Engineering and Radio-Electronic Systems,
Faculty of Radio Physics, Electronics and Computer Systems,
Taras Shevchenko National University of Kyiv, Kyiv

ANALOG NEURAL NETWORK FOR PREDICTION OF PROCESSES IN TIME

Analog neural network model for parallel and serial topology that are predict a coordinates points trajectory of the object thrown at an angle to the horizontal was implemented and studied by using simulation in NI Multisim environment. It is shown that:

– neural networks and their analog models can be successfully used to predict the development process in time;

– universality neural network in predicting the development of a process over time is that the network is stable topology, with one the same learning algorithm can predict the various stages of the process development;

– for improve the accuracy of prediction for each stage of the process need to re-train the neural network to specify the values of weighting coefficients;

- when choosing artificial neural network(ANN) topology a preference should be given to parallel as a consistent topology is more complex than implementing a parallel, although the last has a larger number of components and less accurate prediction.

Keywords: artificial neural network, analog computers, forecasting.

Introduction. Great interest in the research of artificial neural networks (ANN) due to the fact that the way the human brain information processing is very different from the methods that are commonly used by digital computers. The brain is a highly complex, non-linear information processing system. He has the ability to organize their structural components, which called neurons, so that they can perform specific tasks (such as pattern recognition, signal processing senses, motor function) several times faster than that can perform the fastest modern computers [4].

Thanks to the achievements of biology, the theory of artificial neural networks (ANN) was appeared in the 40s of XX century, because artificial neurons made up of elements that model the basic function of biological neurons. Such networks can perform many different tasks, the most common of which are: non-linear approximation of multivariate functions, forecasting the development process that depends on many variables, in time, classification and recognition of input images, search associations, data compression and more.

Today is the ability to simulate the human brain using artificial neural networks created in various software packages for computers (PC). This has many advantages: exceptional versatility, high accuracy (and therefore predictability of algorithm), stability and many others. But for all these benefits have to pay a comparatively low speed and productivity.

Modern analog operational amplifiers can operate at frequencies of several gigahertz. The maximum frequency operational amplifier for calculation function is several times less than its cutoff frequency. If increase the number of links in the neuron model, say, twice, the performance of a digital model will decrease approximately in the same number of times, and the performance of analog model not hardly changed (though will be much more complicated scheme). The price of the processor is much greater than the price of analog circuit of close performance.

Thus the development of analog neural networks models is a promising task.

This work, based on previously designed and created analog model of neuron aims to show the fundamental possibility of analog neural network model to forecast the development process in time [1].

Analysis tools and models. Properties of biological neurons were fixed in basis of mathematical model of neuron. Often, formal neuron (Fig. 1) has input adder, nonlinear converter and branching point output.

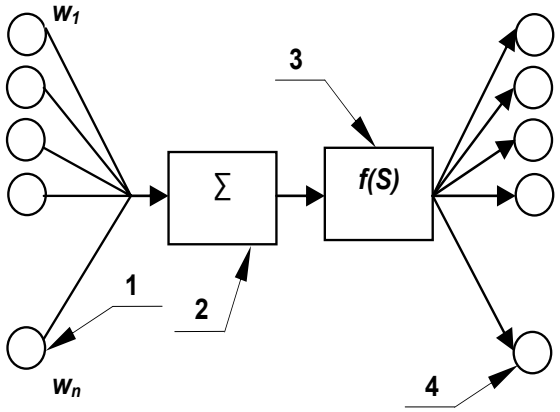

Fig. 1. Block diagram of neuron:
1 – neurons, whose output signals are coming to the input of the neuron;
2 – adder of the input signals;
3 – calculated activation function;
4 – neurons receiving output signal of neuron

The above simple elements of neural networks can be combined into more complex elements: block, layer, column. Layer used the most commonly. Layer is a set of neurons or adders, accepts input information and generating output signals at the same time.

There are several kinds of layers – inputs, outputs, hidden working layer (hidden), which is receiving input signals and generates output signals (Fig. 2).

A mathematical neuron is an adder, the unique exit of that is determined through his inputs and matrix of weighting coefficients as follows: $y = f(u)$, where

$$u = \sum_{i=1}^{n} w_i \cdot x_i + w_0 \cdot x_0. \qquad (1)$$

Here x_i and w_i – accordingly signals on the inputs of neuron and weighting coefficients of entrance, the function of u is called the state of neuron, and $f(u)$ – a transmission(activating) function. Inputs signals can be discrete and analog. The additional entrance of x_0 and corresponding to it weigher coefficient of w_0 are used for creation of change. Type of activating function of neuron of $y = f(u)$ and can be arbitrary and is chosen according to specific technical specification or specific task.

As the multiplier of neuron's input signals and weight coefficients was elected a micro scheme of multiplier on quadrants. An adder and function activation collected on operational amplifiers.

These elements became part of the neuron, which later was used for the creation and study of the neural network, which is based on Rumelhart's perceptron (Fig. 2) and approximates a mathematical function [1, 2].

In this paper implemented and studied analog neural networks models of parallel (Fig. 3) and serial topologies that are predict a coordinates points trajectory of the object thrown at an angle to the horizon by using NI Multisim simulation environment [3].

Simulation results and discussion. Analog ANN model consistent topology was implemented in the first phase of work. As it turned out, the implementation of serial topology is complex challenge of radio engineering, because we must use the time delay of output signal when it supplies on input instead of the original input signal.

To compare the simulation results with calculated analytically using mathematical expression that describes the work ANN [3] was selected start and end of plot the trajectory moving of the body.

Fig. 4 and 5 shows a plot of dependence coordinates *X* of body from time at the beginning of the movement and a plot of dependence coordinates *Y* of body from time at the end of the movement, respectively.

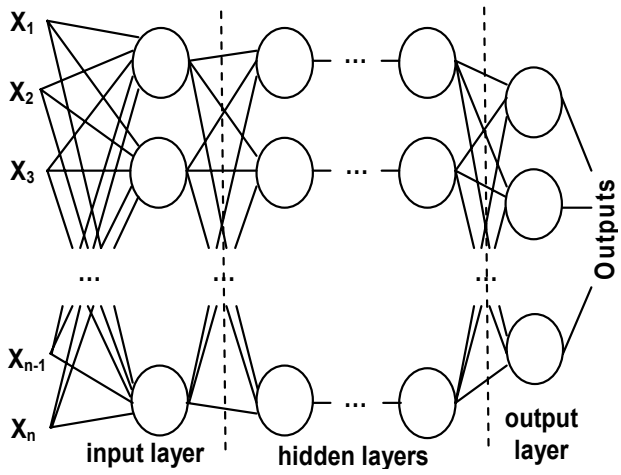

Fig. 2. Block diagram of a two-layer Rumelhart's perceptron

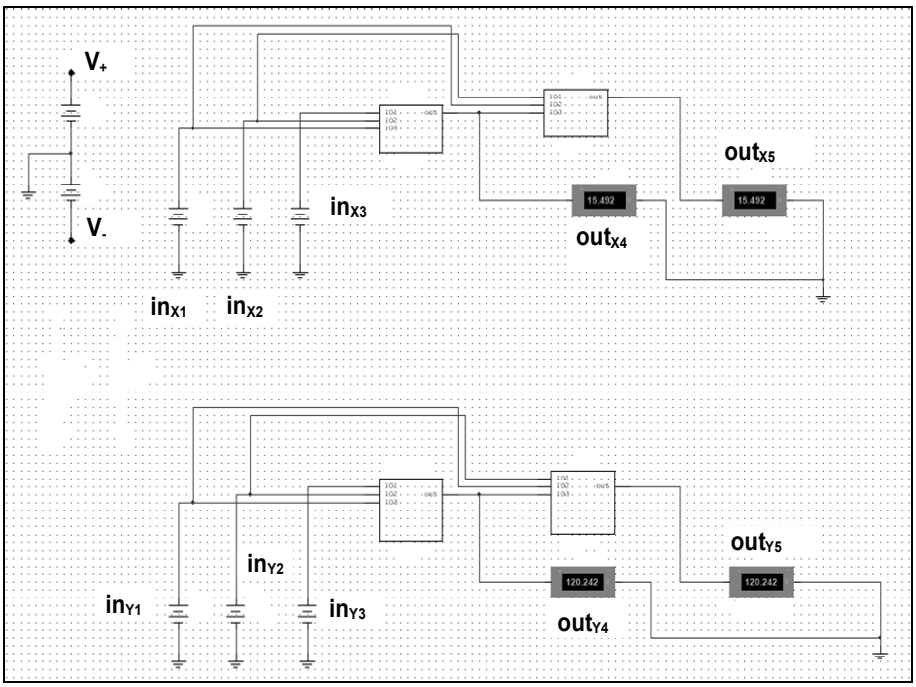

Fig. 3. Model of neural network for parallel predicting of coordinates *X* and *Y*

During analog simulation each subsequent coordinate value obtained with greater error than the previous one, which may be due to accumulation of systematic error calculating individual coordinate, it can be seen from the Fig. 4 and 5. This growth indicates that the mean relative error defined as for coordinates *X*: at the beginning of the movement, it was 0.28 %, and the final area – 0.48 %, and as for the coordinates *Y*: in the area, where body movement begins – 0.23 % and on the final area of 1.53 %.

This fact may indicate that in different parts of the trajectory of body for the forecast coordinates should set different weights, i.e. the need to re-train the neural network.

The implementation of an analog ANN model parallel topology was on the second stage. The results of analog simulation and data obtained analytically at the beginning of the body movement are showed in Table 1.

Mean relative error of determining the coordinates of *X* is 0.2 %, and the coordinates *Y* – 0.4 %. Apparently, analog neural network model with parallel topology is less accurate when predicting nonlinear dependencies are in the initial stages.

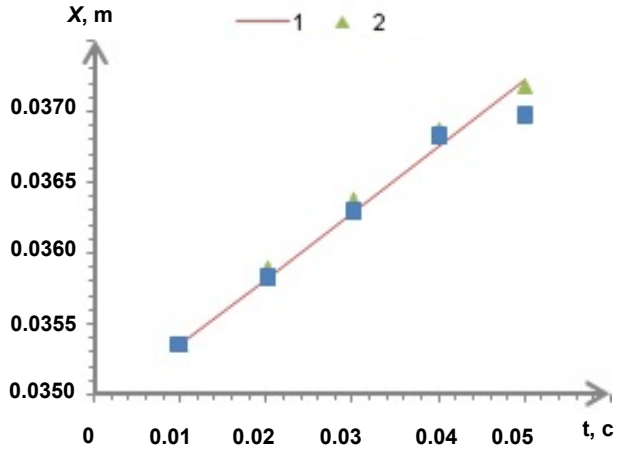

Fig. 4. Dependence coordinates *X* body from time at the beginning of the movement, Analytical (1), using a mathematical expression that describes the work ANN (2), during the analog simulation (3)

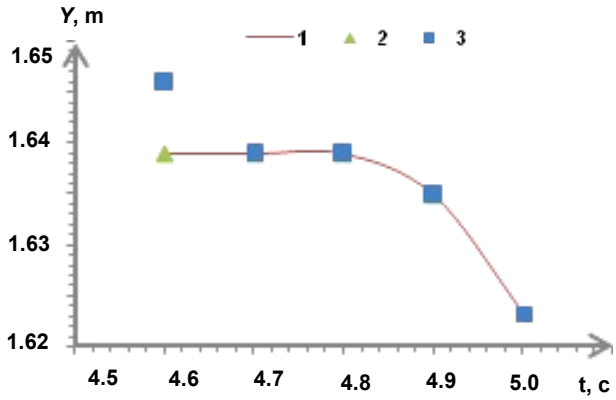

Fig. 5. Dependence coordinates *Y* body from time at the end of the movement, Analytical (1), using a mathematical expression that describes the work ANN (2), during the analog simulation (3)

Table 1

The results of analog simulation and data obtained analytically at the beginning of the body movement

№	Input data, V				Simulation results, V				Analytical calculations, V			
1	X1	0.005374	Y1	0.024426	X4	0.005597	Y4	0.024836	X4	0.005586	Y4	0.024703
	X2	0.005445	Y2	0.024529	X5	0.005618	Y5	0.024931	X5	0.005657	Y5	0.024775
	X3	0.005515	Y3	0.024621								
2	X1	0.005657	Y1	0.024775	X4	0.005663	Y4	0.024836	X4	0.005657	Y4	0.024837
	X2	0.005728	Y2	0.024837	X5	0.005826	Y5	0.024942	X5	0.005726	Y5	0.024837
	X3	0.005586	Y3	0.005597								
3	X1	0.005728	Y1	0.024837	X4	0.005785	Y4	0.024903	X4	0.005726	Y4	0.024837
	X2	0.005586	Y2	0.024837	X5	0.005826	Y5	0.024993	X5	0.005798	Y5	0.024889
	X3	0.005657	Y3	0.024837								

Conclusions. 1. Neural networks and their analog models can be successfully used to predict the development process in time.

2. The network stable topology, with one the same learning algorithm can predict the various stages of the process, this are versatility of neural network in predicting the development of a process over time. However, to improve the accuracy of prediction for each stage of the process need to re-train the neural network to specify the values of weights.

3. Comparison of results of analog simulation allows to opt for a parallel ANN topology because a consistent topology is more complex than implementing a parallel, although the latter has a larger number of components and less accurate prediction.

REFERENCES

1. *Bekh. I.* Approximation of mathematical functions based on the simulation of neural networks with the help of the analog calculating machines (ACM) / I. Bekh, S. Novak // Proc. of the XI Internat. Conf. "Intellectual Systems For Decision Making And Problems Of Computational Intelligence" (ISDMCI'2015). – Zaliznyj Port, Ukraine, 2015. – P. 231–232.

2. *Andrusenko V.* Simulation of Neural Networks by the Analog Calculating Machine (ACM) (in the task of approximation of mathematical functions) / V. Andrusenko, I. Bekh, S. Novak // Вісн. Київ. ун-ту, сер. Радіофізика і електроніка, 2015. – № (1) 21. – С. 10–13.

3. *Бех І. І.* Побудова апроксимаційної функції на основі алгоритму зворотного розповсюдження помилки як методу навчання штучних нейронних мереж / І. І. Бех, С. О. Новак, Ю. І. Хлапонін // Вісн. інженерної академії України, 2016. – № 1. – С. 198–201.

4. *Хайкин С.* Нейронные сети / С. Хайкин // М. : Изд. дом "Вильямс", 2006.

Submitted on 20.12.16

І. Бех, канд. фіз.-мат. наук, доц.,
С. Новак, асп.,
факультет радіофізики, електроніки та комп'ютерних систем,
Київський національний університет імені Тараса Шевченка, Київ

АНАЛОГОВА МОДЕЛЬ НЕЙРОННОЇ МЕРЕЖІ ДЛЯ ПРОГНОЗУВАННЯ РОЗВИТКУ ПРОЦЕСІВ У ЧАСІ

За допомогою середовища моделювання NI Multisim реалізовано і досліджено аналогові моделі нейронних мереж паралельної та послідовної топології, що прогнозують координати точок траєкторії руху об'єкта, кинутого під кутом до горизонту. Показано, що:

– нейронні мережі та їхні аналогові моделі можуть бути успішно використані для прогнозування розвитку процесів у часі;

– універсальність нейронної мережі в прогнозуванні розвитку якогось процесу у часі полягає в тому, що мережа сталої топології з одним і тим самим алгоритмом навчання може прогнозувати різні етапи розвитку процесу;

– для підвищення точності прогнозу для кожного етапу розвитку процесу необхідно знову навчати нейронну мережу для уточнення значень вагових коефіцієнтів;

– при виборі топології ШНМ перевагу слід надати паралельній, оскільки послідовна топологія є більш складною в реалізації ніж паралельна, хоча остання має більшу кількість компонентів і меншу точність прогнозування.

Ключові слова: штучна нейронна мережа, аналогова обчислювальна машина, прогнозування.

И. Бех, канд. физ.-мат. наук, доц.,
С. Новак, асп.,
факультет радиофизики, электроники и компьютерных систем,
Киевский национальный университет имени Тараса Шевченко, Киев

АНАЛОГОВАЯ МОДЕЛЬ НЕЙРОННОЙ СЕТИ ДЛЯ ПРОГНОЗИРОВАНИЯ РАЗВИТИЯ ПРОЦЕССОВ ВО ВРЕМЕНИ

С помощью среды моделирования NI Multisim реализовано и исследовано аналоговые модели нейронных сетей параллельной и последовательной топологии, которые прогнозируют координаты точек траектории движения объекта, брошенного под углом к горизонту. Показано, что

– нейронные сети и их аналоговые модели могут быть успешно использованы для прогнозирования развития процессов во времени;

– универсальность нейронной сети в прогнозировании развития какого-то процесса во времени заключается в том, что сеть постоянной топологии с одним и тем самым алгоритмом обучения может прогнозировать различные этапы развития процесса;

– для повышения точности прогноза для каждого этапа развития процесса нужно снова учить нейронную сеть для уточнения значений весовых коэффициентов;

– при выборе топологии ИНС предпочтение следует отдать параллельной, так как последовательная топология является более сложной в реализации, чем параллельная, хотя последняя имеет большее количество компонентов и меньшую точность прогнозирования.

Ключевые слова: искусственная нейронная сеть, аналоговая вычислительная машина, прогнозирование.

UDC 004.94:533:538.9

R. Bogdanov[1], eng.,
O. Kostiukevych[1], eng.,
Y. Stubrov[2], eng.,
K. Yakimov[1], sen. eng.,
[1]Faculty of Radio Physics, Electronics and Computer Systems,
Taras Shevchenko National University of Kyiv, Kyiv
[2]V. Lashkaryov Institute of Semiconductor Physics of NAS of Ukraine, Kyiv

CARBON NANOCRYSTALLITES SIZES IN FILMS DEPOSITED BY MAGNETRON METHOD ON DIFFERENT SUBSTRATES

Magnetron sputtering device (MSD) with two erosion zones used for carbon films obtaining on Ni, Cu(Cu_xO_x), Fe and NaCl substrates. The optimal deposition modes were chosen from Monte Carlo (MC) computer simulation. Characterizations of obtained carbon films were done by using of Raman spectroscopy and transmission electron microscopy (TEM). Demonstrated that Ni substrates provide a G-peak of Raman spectra closest to 1580 cm^{-1} and in some cases (Ni sputtered target) G peak of Raman spectra is over 1580 cm^{-1}. This means a noticeable nanocrystalline structure with sp^2 bonds.

Key words: carbon film, magnetron sputtering device, nanocrystallites, computer simulation, Monte Carlo method.

Introduction. Carbon films with nanomaterials (like carbon nanotubes – CNT) may have applications in fuel cells [25], OLED diodes and displays [13, 23] and FET transistors [22]. Some of the latest investigations have shown the possibilities of carbon films synthesis (also with CNT) by the magnetron sputter deposition method for wide sphere of technical applications [1–3, 16]. Magnetron sputtering devices on direct current (hereafter – MSD) had found a wide application in the technology of coating of the conductive materials and their composites [12, 19]. As advantages of method of magnetron sputter deposition of carbon nanomaterials usually highlighted a low substrate temperatures, minimized high energy particles bombardment of substrate, ability of deposition on non-conductive substrates, compatibility with integrated circuits production cycles.

In the current work magnetron sputtering device (MSD) with two erosion zones [4–8, 11] (here and after MSDTEZ) was used for carbon films obtaining on Cu, Cu_xO_x, Fe, Ni and NaCl substrates. Using of Cu as films substrate due to its applicability as conducting layers in integrated circuits, Fe and Ni – as a catalyst sublayers for applications of carbon nanotubes. Monocrystalline NaCl used by the convenience of obtaining of equal surface on cracked edges and their soluble properties, making it easy to separate the resulting film for investigation by transmission electron microscopy (TEM). Some optimal deposition modes were chosen from Monte Carlo (MC) computer simulation for experimental carbon film deposition [4]. Characterization of obtained carbon films was done by using Raman spectroscopy and transmission electron microscopy. From such methods are well known signs of the presence of carbon nanotubes and nanocrystalline structure [9, 10, 20, 21, 24,]. This measurements show of presence of a nanocrystalline structure in obtained films and provided estimation of nanocrystallites sizes.

Modeling and experiment. The magnetic and electric fields in the MSDTEZ are rather complicated, and this makes impossible an analytical description of the particles motion in them. The computer simulation programs of MSDs usually based on the integration of particle motion equations and Monte Carlo collisions description are widely used now to predict the shape of erosion zone of the cathode-target [14, 15]. In the work [15] the Monte Carlo method was used to find the starting positions of secondary electrons at the cathode, which correspond to the steady state discharge operation mode and for indirect prediction of current-voltage characteristics of the discharge. The numerical model of the MSD with two erosion zones (MSDTEZ) of the cathode-target (hereafter – CT), based on the Monte Carlo method, was built previously in the works [4–7] by authors. The searching algorithm of the self-consistent starting positions of the secondary electrons on the CT and the estimation of the cathode sheath thickness, based on the Child-Langmuir law, were presented in [6, 4]. Distribution of the discharge current could be associated to the ion distribution at CT surface, because only there ions define the discharge current. If the discharge current I_d is known experimentally in this discharge operation mode, the distribution of the discharge current could be estimated in easy way [4]. Also in previous work [4] was dedicated to the computer modeling of discharge and sputtering processes in MSD with two zones of erosion by Monte Carlo method.

The MSD with two zones of erosion has a flat disc-shaped cathode (cathode unit) with a diameter of about 80 mm, which contains a magnetic system (Fig. 1). The anode, made of an annular copper tube is placed above the cathode, and similar to the cathode it is cooled by oil, which flows through the cavity therein. The MSD and the above-placed substrate, on which the coating is deposited, are placed in a vacuum chamber of an industrial vacuum system VUP-5 (Fig. 2).

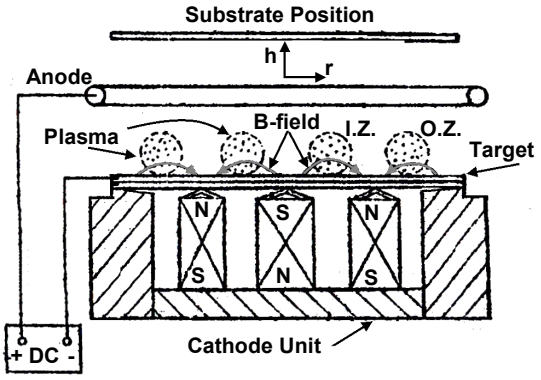

Fig.1. The scheme of MSD with two erosion zones (MSDTEZ) (I.Z. – means "inner discharge zone", O.Z. – means "outer discharge zone") [4, 11]

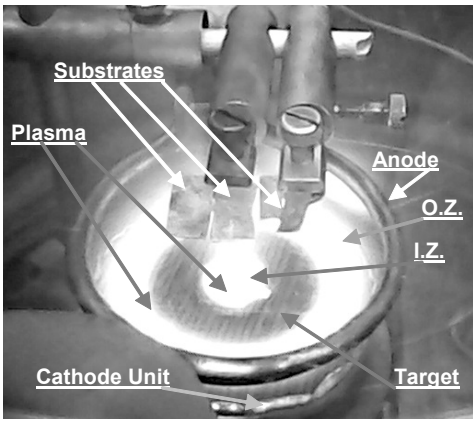

Fig. 2. The general view of MSD with two erosion zones (MSDTEZ) and discharge in vacuum chamber of VUP-5 (I.Z. – means "inner discharge zone", O.Z. – means "outer discharge zone")

The target is removable and placed on the cathode. So, the cathode with the mounted target is called "cathode-target". In the calculations, the origin of cylindrical coordinates has been placed in the center of the target surface. In this series of experiments, the target was made of a graphite pencil rods, which placed into a non-magnetic steel dish. On this stage of research, an analysis of influence of thickness of the graphite target current density distribution along the cathode-target radius between discharge zones provided (Fig. 3), with aim to complement results of the work [4].

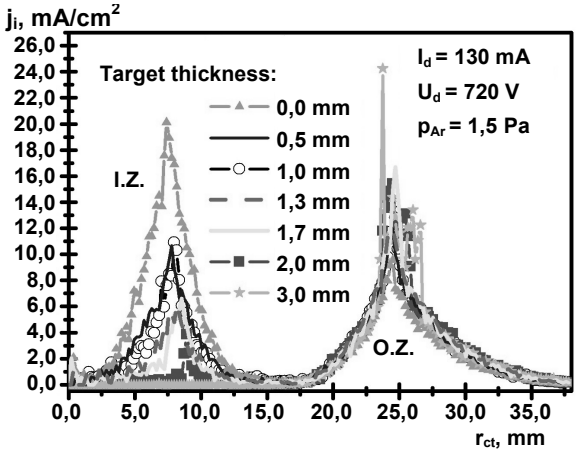

Fig. 3. Computer simulation results of ion current density distribution at different non-magnetic target thickness (I.Z. – "inner discharge zone", O.Z. – "outer discharge zone")

As shown by this simulation, variation of thickness of the target in ranges 0,5..1,0 mm or 1,3…1,7 mm weakly influences on the distribution current density between discharge zones. At the target thickness more than 2,0 mm noted a steep drop in current density in inner zone (Fig. 3). So, in next computer simulations the target thickness 1,785 mm applied. (Averaged experimental target thickness was chosen close to this value too).

With the help of computer simulation were analyzed the dependence of density uniformity of the flux of sputtered particles from the target-substrate distance (Fig. 4). Naturally there observed a decrease of the influence of the initial particles flow radial heterogeneity on away from the surface of the cathode-target at distance 2,0...4,0 cm.

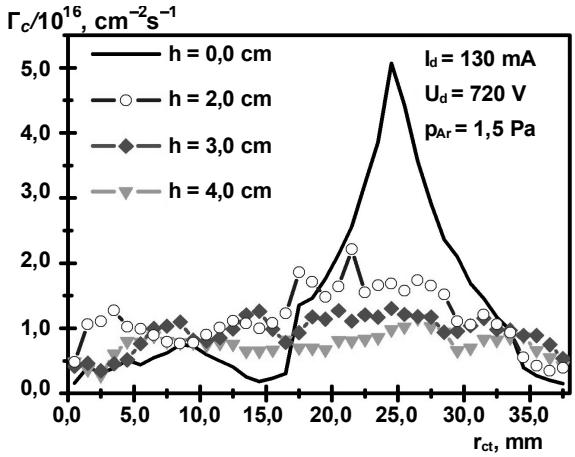

Fig. 4. Computer simulation results of simulation of the flux of carbon particles density at different distances h from the cathode-target of MSDTEZ (Value *h* = 0,0 cm means the cathode-target surface)

Comparison of changes of the average energy of sputtered particles W_c at variation of the distance between cathode-target and substrate demonstrated minimal differences. In all cases of the distance observed higher uniformity of energy along the radius of the MSD system against the corresponding distribution on the surface of cathode-target Fig. 5.

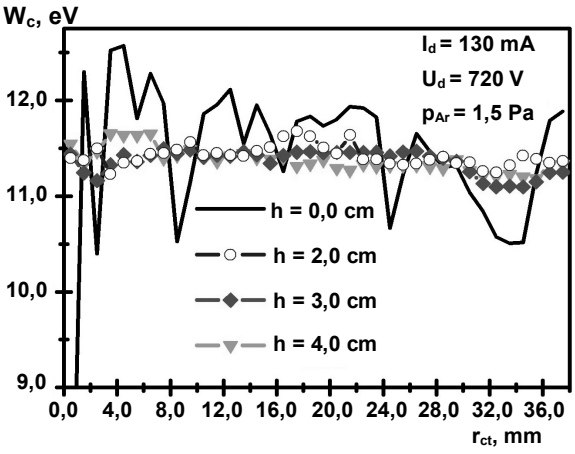

Fig. 5. The comparison of the average energy distributions of the carbon atoms along the radius of MSDTEZ at distances h from the cathode-target

From previous modeling [4] for this MSD discharge were identified modes in which carbon atoms reached of energy over 7,04 eV [18] (Fig. 6). Such energy is suitable for deposition of carbon films containing carbon nanotubes and other nanoparticles. Such criteria correspond to pressures up to 2,0 Pa and currents from 100 mA. Although, as the average value of energy allowable region can be slightly expand up to 4,0 Pa pressure, or at 70 mA current for pressure less than 2,0 Pa.

Additional energy for positive ions can be added at the self-biasing potential of the substrate, which is usually negative. So authors made a direct measurements of electric potential for of the ungrounded substrate under conditions of discharge in MSDTEZ, under conditions of

45…150 mA discharge's current (Fig. 7). These data showed that for pressure of Ar working gas 0,67 Pa and 1,33 Pa, the negative potential of the substrate is reduced on about –2,0 V at the mentioned discharge current variation, and at 6,65 Pa the negative potential increases slightly (by –0,5 V). Thus, under conditions of discharge currents that more than 70 mA can get an additional 3–5 eV for singly charged ions that bombard the substrate. (But these ions usually are from working gas plasma – not by sputtered material).

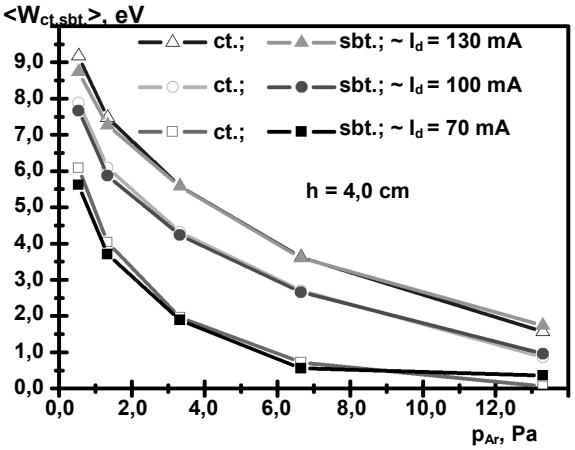

Fig. 6. Computer simulation results of average energy of the sputtered atoms <W_{ct}> and the average energy of atoms approaching the substrate <W_{sbt}> at different currents and pressures (from [4])

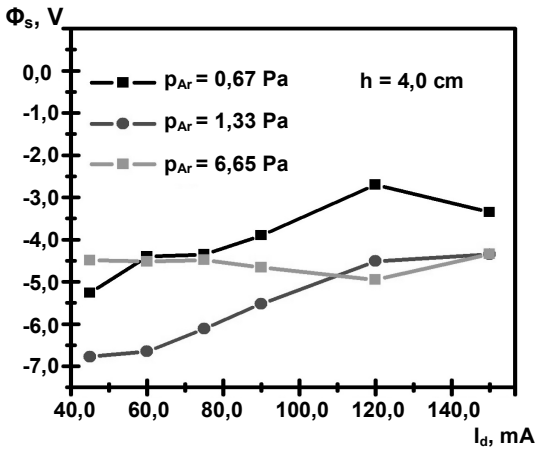

Fig. 7. The results of measurement of floating potential of ungrounded substrate at different discharge modes

The experimental modes of carbon films deposition and substrate-catalyst combinations presented in Table 1. From above computer simulations of discharge modes of MSD with two erosion zones were chosen the most useful for carbon films deposition – at currents I_d = 70..150 mA, U_d = 400..600 V and argon working gas pressure p_{Ar} = 1,33..1,8 Pa. Also some well-known catalysts for carbon nanotubes synthesis were chosen like Ni and Fe. Also the dependence of obtained films properties investigated in cases of different substrates (Ni, Cu, Fe and NaCl) with area near 0,5..2,0 cm^2 (Table 1). At case # 1 used a fragment of Ni target processed in this MSD from sputtered zone and has enhanced surface structure. Observed, that using of such catalysts plates never influenced on discharge voltages and currents.

Target-substrate gap usually was 4,0 cm (except experiment # 8 (Fe) in which 3,0 cm gap was used). NaCl targets were used because we need some thin, rather transparent for electrons films (less than 70,0 nm) for effective transmission electron microscopy (TEM) work. Soluble NaCl is easy way for such films preparing.

Table 1

Modes of experiments

Mode #	Substrate	Catalyst (S, cm^2)	t_s, °C	Experim. time, s	U_d, V	I_d, mA	p_{Ar}, Pa
1	Ni sp.	Ni (3,0)	n/a	2700	550..560	120	1,33
2	Ni						
3	Cu,Cu_xO_x	Ni (1,5)	70..144	1800	550..560	130	
4			70..90	4800	420..460	70	
5	NaCl	Ni (3,0)	n/a	70	540	150	
6				90	500	130	
7				192	400	70	
8	Fe	Fe (1,0)	n/a	1800	560	120	1,8
9	Graphite from the target						

In Table 2 presented carbon films synthesis modes from works of other authors [20, 21, 24] in which chemical vapor deposition (CVD) plasma-enhanced CVD (PECVD), and vacuum arc processes used for carbon films and nanoparticles synthesis.

Table 2

Modes of experiments from literature

Mode #	Substrate	Catalyst (S, cm^2)	t_s, °C	Exper. time, s	U_d, V	I_d, A	p_{mix}, Pa
10	SiO_2	Ni [20]	(600) 750	(120) 180	530	0,4	931
11	Cu_xO_x	Fe [21]	750	7200	None		Normal.
12	SiO_2	Co [24]	25	n/a	n/a	70(C), 120 (Co),	$1{,}33\times10^{-3}$
13			250				
14			500				
From literature PECVD [20], CVD[21], arc [24]							

On this stage of research the computer simulation results (from [4, 6, 7]) were also compared with experimental data of sputtering-deposition of graphite target with Ni catalyst plates (Fig. 8) like in modes # 5-7 (Table 1). Film thickness on glass substrate was evaluated by optical interference method. Mass density $\rho_{Gr} = 2{,}35$ g/cm^3 [17] defined as for some technical graphite, which enabled calculation of particles flux density on substrate Γ_{te} and make the comparison of it with average value estimated from computer simulation at such condition Γ_{tm} (Table 3).

Table 3

Carbon flux in some modes

	I_d = 70 mA	I_d = 130 mA
V, nm/s	0,08 (U_d = 385 V)	0,33 (U_d = 510 V)
$\Gamma_{te}\times10^{15}$, $cm^{-2}s^{-1}$	0,94 (U_d = 385 V)	3,9 (U_d = 510 V)
$\Gamma_{tm}\times10^{15}$, $cm^{-2}s^{-1}$	3,9 (U_d = 466 V)	7,0 (U_d = 566 V)
p_{Ar} = 1,33 Pa, ρ_{Gr}= 2,35 g/cm^3[17]		

In that time of use the graphite target were rather ruined and thinned. This decreases the discharge voltage at the same current in compare to modes #1–8 (Table 1). The comparison of Γ_{te} and Γ_{tm} demonstrates that modeling results are closely to real experimental at highest discharge currents and at comparable discharge voltage U_d.

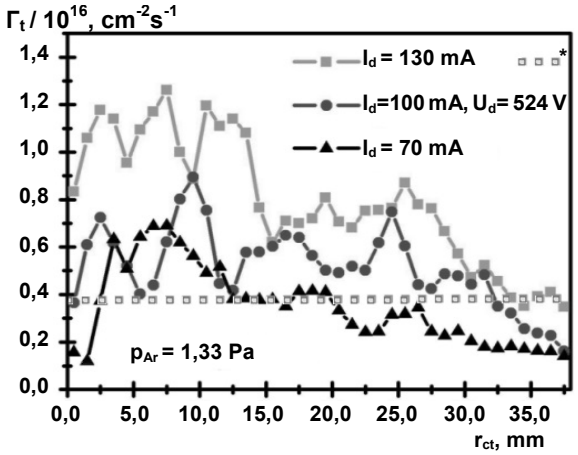

Fig. 8. The comparison of computer simulation results of carbon particles flux Γ_t on target placed on distance h = 4 cm from cathode at different discharge currents (from [4]) and particle flux from experiment at 130 mA (marked "*") from Table 3

Analysis and interpretation of Raman spectra of C-films. The characterization of carbon films was done by well-known method of optical Raman spectroscopy [9, 10]. Micro-Raman spectra recorded in backscattering geometry at room temperature (T = 300 K) on triple spectrometer *T-64000 Horiba Jobin-Yvon* with a cooled CCD detector. The excitation of Raman spectra carried by Ar-Kr laser with wavelength $\lambda_e = 488$ nm. Focusing optical lens system 50x/0,75 provided a laser spot diameter of about 1 μm. The spectra were recorded by corresponding computer software of the spectrometer and analyzed by using of assumptions from [9, 10]. Examples obtained spectra are shown in Fig. 9. Examined Raman spectra for the films samples are demonstrate notable D (~1250 .. 1450 cm^{-1}) and G (~1500 .. 1600 cm^{-1}) bands. There were also analyzed relative values of peaks *I(V)* and *I(P)*. The results of the study of Raman spectra are shown in Table 4.

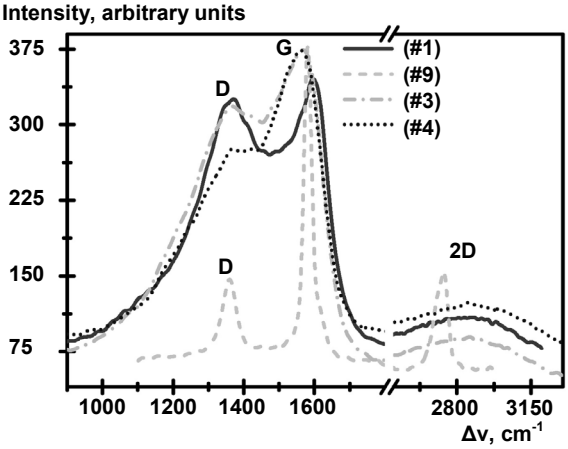

Fig. 9. Raman shift of carbon films samples in cases of films on Cu (Cu_xO_x) at 130 mA (mode #3) and 70 mA (mode #4) and on nickel (Ni) at 120 mA (mode #1), also some spectrum from graphite target fragment (mode #9 (Table 1))

G-band of Raman spectra associated with sp^2 bonds in carbon structures and has the highest frequency in graphite and at grinding of graphene layers in graphite-like materials the G-band frequency decreases. D-band associated with existence of separate aromatic rings of six carbon atoms. D-band in ideal graphite is absent through of infinite graphene planes. When there are limited sizes of nanocrystallites, exists so called correlation length or radius L_a, the intensity of D-band is growing and has a maximum value at $L_a = 2$ nm [9, 10]. If the D-band (Fig. 9.) is enough wide, it indicates to a significant degree of disorder in the carbon film sample (as in [21]).

According to [9,10], in the case of graphite or nanocrystalline graphite the G band frequency peak will be no less than 1580 cm^{-1}. Then from the known value $(I(D)/I(G))$ possible to estimate the radius L_a:

$$L_a = C(\lambda)\frac{I(G)}{I(D)} = 4{,}4\ nm \times \left(\frac{I(D)}{I(G)}\right)^{-1}. \qquad (1)$$

The sign of nanocrystalline graphite with transition in amorphous graphite is the peak frequency of band G, which is less than 1580 cm^{-1} [10]. Expression for La in this case is follows:

$$L_a = \sqrt{\frac{I(D)}{I(G)}\frac{1}{C'(\lambda)}} \approx 1{,}3484\ \text{nm} \times \left(\frac{I(D)}{I(G)}\right)^{0,5}. \qquad (2)$$

The experimental results obtained. The best cases from experiments with Ni and Cu substrates compared with graphite, which used in target ("mode" #9 from Table 1) and depicted on Fig. 9. The most samples have G-band peak lower than 1580 cm^{-1}, but some Ni (mode #1), have frequencies upper then 1580 cm^{-1} as the graphite sample.

Calculated from expressions (1) and (2) average values (from 3–5 points) *of* $<L_a>$ for every experimental modes are shown in Table 4. The relation of $<L_a>$ to G-peak frequency $<\Delta\nu(G)>$ depicted on Fig. 10 for every cases #1–14.

Table 4

Raman spectra data and correlation length

Experiment mode number (substrate)	$<\Delta\nu(D)>$, cm^{-1}	$<\Delta\nu(G)>$, cm^{-1}	$<I(D)/I(G)>$	$<L_a>$, nm
1. (Ni sput.)	1363,61	1589,645	0,916	4,8035
2. (Ni)	1359,172	1575,444	0,8958	1,2762
3. (Cu, Cu_xO_x)	1370,678	1560,28	0,8517	1,2444
4. (Cu, Cu_xO_x)	1380,429	1557,405	0,7408	1,1605
5. (NaCl)	1395,427	1560,096	0,8473	1,2412
6. (NaCl)	1383,891	1557,921	0,7916	1,1997
7. (NaCl)	1377,309	1562,383	0,8529	1,2453
8. (Fe)	1362,572	1571,636	0,7096	1,1359
9. Graphite	1359,725	1581,241	0,3888	11,318
10. (SiO_2) [20]	1341,667	1606,25	1,3205	3,332
11. (Cu_xO_x) [21]	1326,866	1589,552	1,4895	2,954
12. (SiO_2) [24]	~1350	1547	0,3	0,7386
13. (SiO_2) [24]	~1350	1557	0,68	1,1119
14. (SiO_2) [24]	~1350	1582	1,05	4,1905
Note: the brackets <..> mean averaged value.				

In cases of Cu substrate, at two different discharge current modes – 70 mA (mode #4, Table 1) and 130 mA (mode #3, Table 1), from comparison of Raman spectra observed strong dependence of nanocrystallites sizes – lower current mode with lower energy of carbon particles provides smaller $<L_a>$. But on NaCl the $<L_a>$ decreases strongly at increasing of discharge current to 150 mA.

Cases of Ni substrate with sputtered surface (mode #1, Table 1) are closer to results of other works in which C(:Me)-films and multiwall carbon nanotubes (MWCNT) are synthesized at higher temperatures 500-750°C (modes #10 .. #14 from works [20, 21, 24]) but in compare – in the current experiments substrate temperatures reached 90-144°C (Fig. 10). Ni mode # 2 on smooth surface as the Fe (#8)and Cu/Cu_xO_x (#3, 4) cases are similar to "low temperature" case #13 from work [24], and demonstrate bigger $<L_a>$ in comparison of the case #12 (at room temperature (RT)). All considered carbon films in cases with Fe (#8) and NaCl (as most Cu and Ni cases) substrates can be classified as disordered nanocrystalline graphite or amorphous graphite with high predominance of sp^2 faction because they $<\Delta\nu(G)>$ lower than 1580 cm^{-1} and wide D-bands (Fig. 8).

The size of nanocrystallites which exists in films, usually have a correlation length $<L_a>$ =1,1 .. 1,2 nm (Table 4). This means the average transverse dimensions near 2,4 nm. Such dimensions were verified by TEM of films, which deposited on NaCl substrates in cases of three currents: 70 mA, 130 mA (Fig. 11), 150 mA. Average L_a = 1,2 nm – means that same nanocrystalline structure is repeated in radius $<L_a>$. At TEM images of films we compared a circle with $2<L_a>$ = 2,4 nm diameter with such visible structures in film (Fig. 11). As we can see, the visible structures have a central symmetry. This also means that our assumptions about nanocrystallites sizes from Raman spectra data are true.

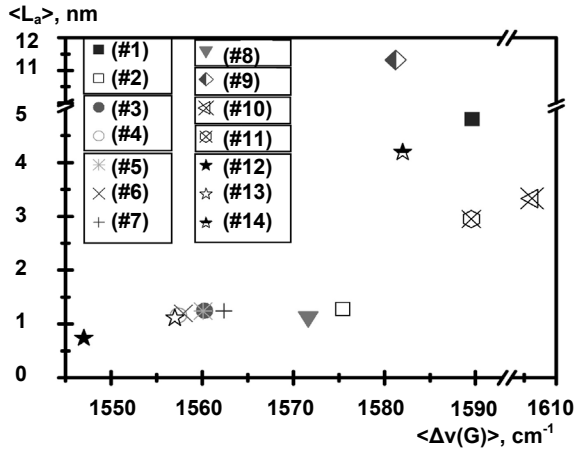

Fig. 10. Relation between averaged correlation length $<L_a>$ and $<\Delta\nu(G)>$ in different experimental modes (see Table 4, 1, 2)

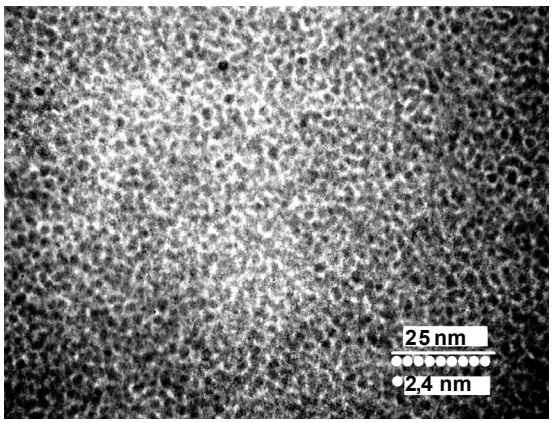

Fig. 11. Example of transmission electron microscopy (TEM) image of film, which deposited on NaCl at 130 mA

After this we can extrapolate this on case with that sputtered Ni surface (#1), which provides more ordered structure with G-band more than 1580 cm^{-1} and nanocrystallites sizes more than 9,6 nm. Another Ni sample demonstrates bigger (2,56 nm) sizes than cases #3 .. #8. This all shows the advantages of Ni substrates (as the catalysts) for carbon films with nanoparticles like in cases of another methods #10 .. #14 [20, 21, 24].

Logically, that the source of carbon – the graphite target has the biggest nanocrystals 22 nm and it is more ordered, as we can see from its G-peak frequency near to 1580 cm^{-1} and narrow width of bands G and D observed.

Conclusions. From the Monte-Carlo computer simulations of discharge modes of magnetron sputtering device with two erosion zones there were chosen the most useful discharge modes for carbon films deposition – currents I_d = 70..150 mA, voltages U_d = 400 .. 600 V and argon working gas pressure p_{Ar} = 1,33 .. 1,8 Pa. As shown by this simulation, variation of thickness of the graphite target in ranges 0,5 .. 1,0 mm or 1,3 .. 1,7 mm weakly influences on the distribution current density between discharge zones in this MSDTEZ. At the target thickness more than 2 mm noted a steep drop in current density in inner zone of the discharge (Fig. 2). So, in the next computer simulations the target thickness 1,785 mm applied and for experiments the graphite target with similar thickness used. Observed, that using of Ni and Fe catalysts small plates (1,0 .. 3,0 cm^2) never influenced seriously on the discharge voltages and currents.

Magnetron sputtering-deposition method was used for carbon films synthesis on different substrates at not very high temperatures (90 .. 144 ^oC). Here was shown that Cu_xO_x and Ni substrates provide a G-peak of Raman spectra closest to 1580 cm^{-1} and at the same discharge voltages and current in case of Ni sputtered target, G-peak is over 1580 cm^{-1}. The last means a noticeable nanocrystalline structure with sp^2 bonds, which is closer to carbon nanotubes samples, which obtained at another methods (like chemical vapor deposition (CVD), plasma enhanced CVD (PECVD) [20, 21, 24]). From Raman spectra analysis the nanocrystallites sizes were estimated. As shown in this series of experiments, variation of discharge current in range from 70 mA to 150 mA not seriously influenced on nanocrystallites, which vary near 2,4 nm. The nanocrystallites sizes on NaCl were confirmed by TEM. Appearance of larger nanocrystallites (>9,6 nm) in case of sputtered Ni substrate (with complex surface) meant that using of specially formed substrates with catalytic Ni nanoparticles, similarly to CVD/PECVD may provide more useful conditions for carbon nanotubes growth even at magnetron sputtering-deposition method.

REFERENCE

1. *Antonenko S. V.* Magnetronnaja tehnologija sozdanija grafitovyh pokrytij, nanotrubok, i nanostruktur na ih osnove / S. V. Antonenko // Nanotekhnologii. Nauka i proizvodstvo, 2012. – № 5. – P. 8–10 (in rus.).

2. *Antonenko S. V.* Issledovanie uglerodnyh nanostruktur, poluchennyh metodom raspylenija na postojannom toke / S. V. Antonenko, S. N. Mal'cev, A. A. Timofeev // Inzhenernaja fizika, 2002. – № 1. – P. 38–40 (in rus.).

3. *Antonenko S. V.* Poluchenie uglerodnyh nanotrubok metodom magnetronnogo raspylenija na postojannom toke / S. V. Antonenko, S. N. Mal'cev // Pribory i tekhnika eksperimenta, 2005. – № 3. – P. 150–152 (in rus.).

4. *Bogdanov R. V.* Computer simulation of sputtering of graphite target in magnetron sputtering device with two zones of erosion / R. V. Bogdanov, O. M. Kostiukevych // Materials Science-Poland, 2015. – № 33(1). – P. 82–94

5. *Bogdanov R. V.* Komp'yuterne modelyuvannya mahnetronnoho rozpylyuvanogo pristroyu z dvoma zonamy eriziyi / R. V. Bogdanov, O. M. Kostiukevych. // Visnik Kyyivskoho nacionalnoho universitetu imeni Tarasa Shevchenka. Seriya "Ffizyko-matematichni nauky", 2012. – № 1. – P. 249–260 (in ukr.).

6. *Bogdanov R.* Zoned target in the experimental investigation of the magnetron sputtering device with two erosion zones/ R. Bogdanov, O. Kostiukevich // Visnik Kiyivskoho nacionalnogo universitetu imeni Tarasa Shevchenka. : Radiofizyka ta electronika, 2013. – №(2)20. – P. 7–11.

7. *Bogdanov R. V.* Computer simulation of carbon film deposition in magnetron sputtering device with two erosion zones / R. V. Bogdanov, O. M. Kostiukevych, Y. Y. Stubrov // Abstracts of the XVth Internat. Young Sci.' Conf. of Applied Phys., June 10–13, 2015, Kyiv, Ukraine, Taras Shevchenko National University of Kyiv, Faculty of Radiophysics, Electronics and Computer Systems. – P. 59–60.

8. *Carbon* nanocrystallites sizes in films deposited by magnetron method on different substrates / R. V. Bogdanov, O. M. Kostiukevych, Y. Y. Stubrov, K. I. Yakimov // Abstracts of XII Internat. Conf. "Electronics and applied physics", Oct. 19–22, 2016, Kyiv, Ukraine, Taras Shevchenko National University of Kyiv Faculty of Radiophysics, Electronics and Computer Systems. – P.65–66.

9. *Ferrari A. C.* Interpretation of Raman spectra of disordered and amorphous carbon / A. C. Ferrari, J. Robertson // Phys. Rev. B, 2000, – Vol. 61, № 2. – P. 14095–14107.

10. *Ferrari A. C.* Raman spectroscopy of graphene and graphite: disorder, electron–phonon coupling, doping and nonadiabatic effects / Andrea C. Ferrari.// Sol. St. Communications, 2007. – № 143. – P. 47–57.

11. *Kucherenko E. T.* Magnetronnoe raspylitelnoe ustroystvo s dvumua zonams eriziyi : Sb. nauch. trudov. / E. T. Kucherenko // Plasmotehnologia-97. – Zaporozhye : RIP "Vidavets", 1997. – P. 121–124 (in rus.).

12. *Kuzmichev A. I.* Magnetronnyie raspilitenye systemy. Kniga 1. Vvedenie v fiziku i tehniku magnetronnogo raspilenija / A. I. Kuzmichev. – Kiev : "Avers", 2008. – 244 p. (in rus.).

13. *Liu D.* Organic light-emitting diodes with carbon nanotube cathode-organic interface layer / Deang Liu, Michael Fina, Jinghua Guo et al. // Applied Phys. Lett., 2009., – № 94 (013110). – P. 013110-1–013110-3.

14. *Influence* of the geometrical configuration on the plasma ionization distribution and erosion profile of a rotation cylindrical magnetron: a Monte Carlo simulation / J. Musschoot, D. Depla, J. Haemers, R. de Gryse // Plasma Sources Sci. Technol., 2006. – № 39, 015209. – P. 3989–3993.

15. *Investigation* of the sustaining mechanisms of dc magnetron discharges and consequences for I-V characteristics / J. Musschoot, D. Depla, J. Haemers, R. de Gryse. // Plasma Sources Sci. Technol., 2008. – № 41, 015209. – P. 1–5.

16. *Onoprienko A. A.* Relationship between structure and electrical resistivity in nano-structured copper-containing carbon films. / A. A. Onoprienko, I. B. Yanchuk, I. A. Kossko // Surface&Coatings Technology, 2010., – № 204. – P. 4091–4094.

17. *Razvitiye* product union : tekhnicheskiy spravochnik // [http://razvitie-pu.ru/?page_id=949], 2013 (in rus.).

18. *Shchur D. V.* Uglerodnyye nanomaterialy i fazovyye prevrashcheniya v nikh. : monografiya / D. V. Shchur, Z. A. Matysina, S. Yu. Zaginaychenko. – Dnepropetrovsk : Nauka i obrazovaniye, 2007 (in rus.).

19. *Harakteristiki* plazmy nesbalansirovannoj magnetronnoj raspylitel'noj sistemy i ih vlijanie na parametry pokrytij ZnO:Ga / A. A. Soloviev, A. N. Zaharov, S. V. Rabotkin, K. V. Oskomov, N. S. Sochugov // Fizika I khimija obrabotki materialov, 2009. – № 2. – P. 58–65 (in rus.).

20. *Sun X.* The effect of catalysts and underlayer metals on the properties of PECVD-grown carbon nanostructures / Xuhui Sun, Ke Li, Raymond Wu et al. // Nanotechnology, 2010. – Vol. 21, № 045201. – P. 1–6.

21. *Catalytic* Consequence of the Interface Between Iron Catalysts and Foils in Synthesis of Aligned Nanocarbons on Foils / E. Vanhaecke, F. Huang, Y. Yu et al. // Top Catal, 2011. – № 54. – P. 986–997.

22. *Wang C.* Wafer-Scale Fabrication of Separated Carbon Nanotube Thin-Film Transistors for Display Applications / Chuan Wang, Jialu Zhang, Koungmin Ryu et al. // *Nano Lett.*, 2009. – № 9 (12). – P. 4285–4291.

23. *Wu X.* Modification of carbon nanotube transparent conducting films for electrodes in organic light-emitting diodes / Xiaoming Wu and Hong-Zhang Geng // Nanotechnology, 2013. – № 24, 435201. – P. 1–8.

24. *Growth* of Carbon Nanotubes on Carbon/Cobalt Films with Different sp^2/sp^3 / Naiyun Xu, Siu Hong Tsang, Beng Kang Tay et al. // Hindawi Publishing Corporation : Journal of Nanomaterials, 2013. – Vol. Article ID 730952. – P. 1–5.

25. *Zhang W.*, Application of carbon nanotubes in polymer electrolyte based fuel cells / Wei Zhang and S. Ravi, P. Silva // Rev. Adv. Mater. Sci., 2011. – № 29. – P. 1–14.

Submitted on 20.12.16

Р. Богданов[1], інж.,
О. Костюкевич[1], інж.,
Ю. Стубров[2], інж.,
К. Якимов[1], пров. інж.,
[1] факультет радіофізики, електроніки та комп'ютерних систем,
Київський національний університет імені Тараса Шевченка, Київ
[2] Інститут фізики напівпровідників імені В. Є. Лашкарьова НАН України, Київ

РОЗМІРИ ВУГЛЕЦЕВИХ НАНОКРИСТАЛІТІВ У ПЛІВКАХ, ОСАДЖЕНИХ МАГНЕТРОННИМ МЕТОДОМ НА РІЗНИХ ПІДКЛАДКАХ

Магнетронний розпорошувальний пристрій (МРП) із двома зонами ерозії було використано для осадження вуглецевих плівок на Ni, Cu(Cu$_x$O$_x$), Fe та NaCl підкладках. Оптимальні режими осадження вибрано на основі комп'ютерного моделювання методом Монте-Карло. Дослідження отриманих вуглецевих плівок виконано за допомогою спектроскопії комбінаційного розсіювання світла та електронної просвітної мікроскопії. Показано, що Ni підкладки забезпечують G-пік спектра комбінаційного розсіювання світла близько 1580 см$^{-1}$, а у випадку Ni підкладки з розпорошеною поверхнею частота G-піку перевищує 1580 см$^{-1}$. Це свідчить про наявність нанокристалічної структури з sp^2-зв'язками.

Ключові слова: вуглецева плівка, магнетронний розпорошувальний пристрій, нанокристаліти, комп'ютерне моделювання, метод Монте-Карло.

Р. Богданов[1], инж.,
О. Костюкевич[1], инж.,
Ю. Стубров[2], инж.,
К. Якимов[1], вед. инж.,
[1] факультет радиофизики, электроники та компьютерных систем,
Киевский национальный университет имени Тараса Шевченко, Киев
[2] Институт физики полупроводников имени В. Е. Лашкарёва НАН Украины, Киев

РАЗМЕРЫ УГЛЕРОДНЫХ НАНОКРИСТАЛЛИТОВ В ПЛЕНКАХ, ОСАЖЕННЫХ МАГНЕТРОННЫМ МЕТОДОМ НА РАЗЛИЧНЫХ ПОДЛОЖКАХ

Магнетронное распылительное устройство (МРП) с двумя зонами эрозии было использовано для осаждения углеродных пленок на Ni, Cu (Cu$_x$O$_x$), Fe и NaCl подложках. Оптимальные режимы осаждения избраны на основе компьютерного моделирования методом Монте-Карло. Исследование полученных углеродных пленок выполнено с помощью спектроскопии комбинационного рассеивания света и электронной просветной микроскопии. Показано, что Ni подложки обеспечивают G-пик спектра комбинационного рассеивания света около 1580 см$^{-1}$, а в случае Ni подложки с распыленной поверхностью частота G-пика превышает 1580 см$^{-1}$. Это свидетельствует о наличии нанокристаллической структуры с sp^2-связями.

Ключевые слова: углеродная пленка, магнетронное распылительное устройство, нанокристаллиты, компьютерное моделирование, метод Монте-Карло.

UDC 535.217

D. Vasylenko, post grad. stud.,
V. Grygoruk, Dr. Sci.,
V. Sydorenko, Ph. D.,
Department of Quantum Radio Physics,
Faculty of Radio Physics, Electronics and Computer Systems,
Taras Shevchenko National University of Kyiv, Kyiv

OPTICAL NEAR-FIELD SUB-NANO-POLISHING OF THE DIELECTRICS SURFACE USING PHOTOCHEMICAL REACTION

In the paper we consider the method of polishing surface nano-roughness of quartz substrate using optical near-field dipole-dipole interaction of atomic chlorine with quartz molecules. Atomic chlorine obtained by photodissociation of molecular chlorine via optical near field of quartz substrate surface nano-roughness. Polarization of chlorine atoms and quartz molecules made by evanescent wave generated on the substrate surface when it is irradiated with a green laser light from the opposite side at an angle no less than the angle of total internal reflection.

Keywords: photodissociation, sub-nano-polishing, optical near field, evanescent wave, surface nano-roughness, dipole-dipole interaction.

Introduction. The optical elements (mirrors, prisms, lenses, etc.) are widely used in most optical device: lasers, gyroscopes, physical fields sensors and more. An important feature of the above elements is the degree of homogeneity of the surface. Devices measurement accuracy depends on it. Now known a variety of methods to reduce the surface roughness and thus increase its quality. However, these methods do not allow to eliminate surface defects on subnanometer scale. This can be done using optical near field. This makes the relevance of the research and the possible widespread practical use of the results.

Purpose of the research is to develop a method of reducing the quartz substrate surface roughness from the tens and units of nanometers to units of angstroms.

Experiment idea. In a vacuum chamber placed quartz (SiO_2) substrate with nanometer scale roughness (Fig. 1). The chamber filled with molecular chlorine Cl_2 up to the pressure of 100 Pa. The chemical activity of molecular chlorine is not enough to react with quartz [1]:

$$SiO_2 + Cl_2 \not\rightarrow$$

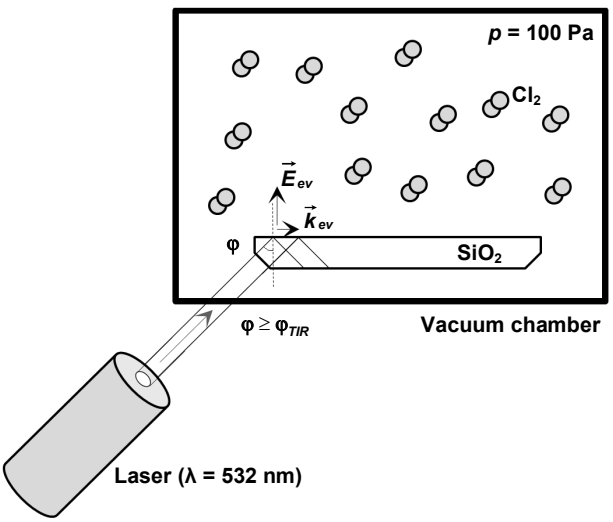

Fig. 1. Schematic of the experimental setup ($\vec{k}_{ev}$ and $\vec{E}_{ev}$ are wave vector and the electric field strength of evanescent wave respectively, φ is the angle of incidence of the laser radiation from the opposite side the quartz substrate surface, φ_{TIR} is the angle of total internal reflection)

Substrate is illuminated by beam of green laser light (λ = 532 nm) from the bottom at an angle of total internal reflection. Above the substrate surface at the distance of < λ/2π formed evanescent wave, which polarizes the molecules of Cl2 and SiO2. Obtained dipoles generate all three components of the electromagnetic field [4; 2] (Fig. 2).

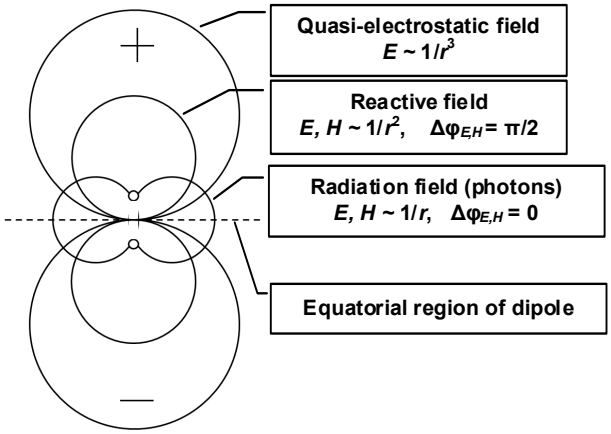

Fig. 2. Directional pattern of the three components of electromagnetic field generated by the dipole

The Fig. 3 shows that in the near zone the strongest component is ~1/r^3 (near-field component). It is much stronger than the radiation field is ~1/r, which is dominated by only in the far zone. The Fig. 4 shows that the graph of sum of all 3 components of the electric field (marked as "Σ") almost coincides with the graph of ~1/r^3 in the region I (components ~1/r^2 and ~1/r are very weak). Graph of sum of components in region III almost identical with the graph of ~1/r (components ~1/r^2 and ~1/r^3 are negligible). Thus the graph in regions I and III in logarithmic scale (both axes are logarithmic scale) should look almost straight as graphs ~1/r^3 and ~1/r respectively. All 3 components are commensurate in the region II. Thus the graph of sum of components in this region is a curved form. Regions I, II and III are not firmly fixed.

Near-field component ~1/r^3 of SiO_2 leading to dissociation of molecular chlorine [1]:

$$Cl_2 \xrightarrow{\text{Near field}} 2Cl\,.$$

Thus molecular chlorine getting into the near field, becomes much more reactive atomic chlorine. This process is irreversible in the near field. After the dissociation of molecular chlorine atomic chlorine becomes

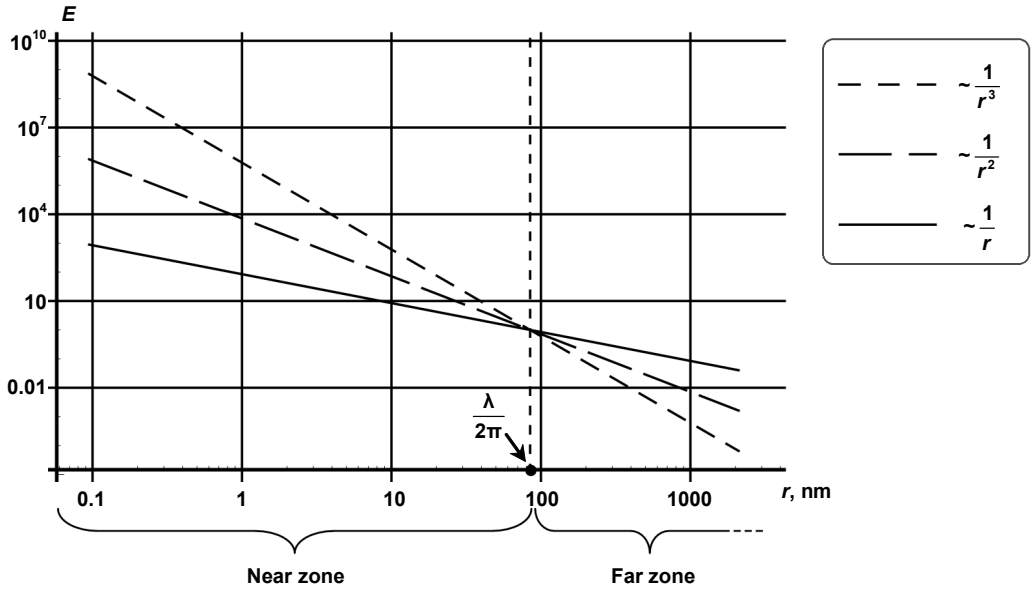

Fig. 3. Schematic illustration of the dependence of the electric field strength *E* on the distance *r* from the substrate surface nano-roughness of the quartz for the three components of the electric field generated by the dipole (both axes are logarithmic scale)

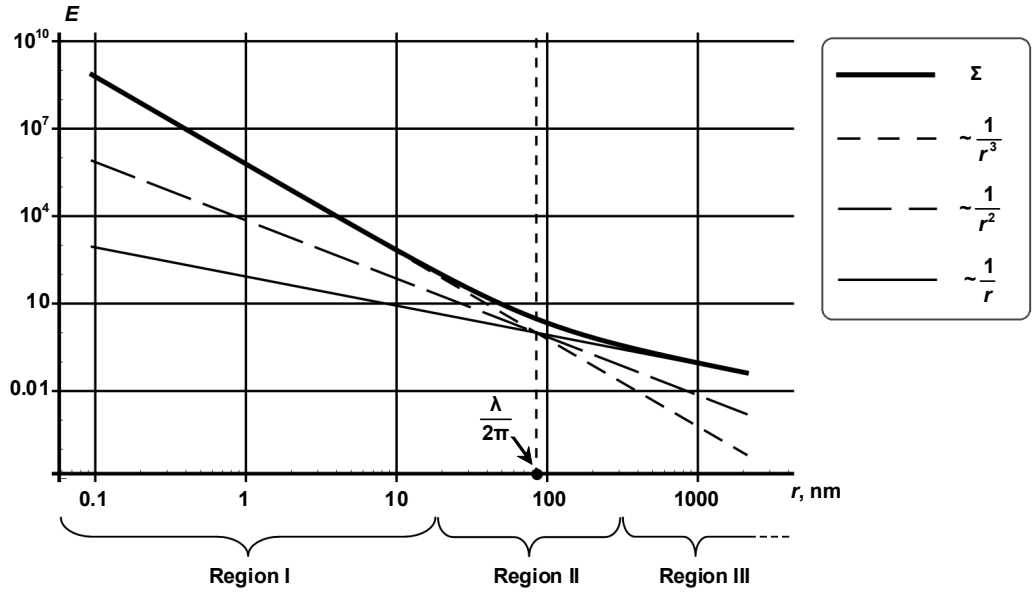

Fig. 4. Schematic illustration of the dependence of the full electric field strength *E* (the graph is marked as "Σ") on the distance *r* from the quartz substrate surface nano-roughness as a result of summing 3 components of the electric field generated by the dipole (both axes are logarithmic scale)

polarized by evanescent wave. Evanescent wave propagates along the surface (Fig. 1).

Therefore, the vector of the electric field strength is directed orthogonally to the surface plane. The dipoles (electric dipole moments) of Cl and SiO_2 are oriented parallel to the vector of the electric field strength. Since the near field is very inhomogeneous and decreases exponentially with distance from the substrate surface [3], it attracts dipoles of Cl to the substrate surface. Since dipoles of Cl (gas) is always located above the dipoles of SiO_2 (substrate surface), then we have a situation where indicated dipoles (electric dipole moments) are oriented along one straight line (Fig. 5). Thus the interaction of dipoles of Cl and SiO_2 is due to component of $\sim 1/r^3$, in contrast to previous experiments photochemical sub-nano-polishing [1], wherein the substrate was irradiated from above orthogonal surface plane through which the dipoles of Cl and SiO_2 were oriented parallel to the equatorial regions to each other (Fig. 6). Such a mutual arrangement the dipoles their interaction was due only component of $\sim 1/r$.

Atomic chlorine reacts with nano-roughness of the quartz substrate. The resulting reaction produces silicon tetrachloride and oxygen that are gases:

$$SiO_2 + 4Cl \xrightarrow{\text{Near field}} SiCl_4\uparrow + O_2\uparrow .$$

Because of this quartz substrate roughness is etched. Notability and unusual of this reaction consists of that each molecule of quartz surface nano-roughness should interact with four atoms of atomic chlorine before they interact with each other, which is possible only in the near field. Thus, if you turn off the laser and in this way to remove the near field, the four chlorine atoms surrounding quartz molecule interacts primarily with each other and forms a conventional two molecules of molecular chlorine which does not react with the quartz. Therefore photochemical sub-nano-polishing process will stop.

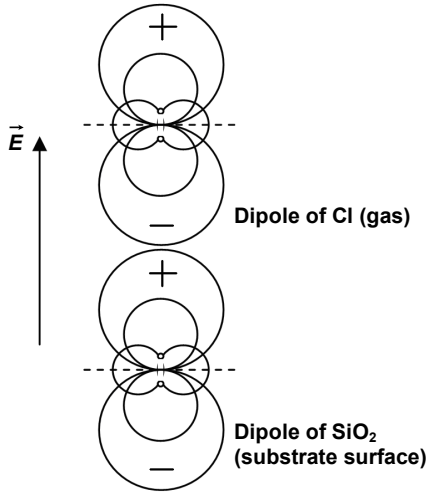

Fig. 5. The orientation of the dipoles of Cl and SiO_2 under the action of evanescent wave when using total internal reflection

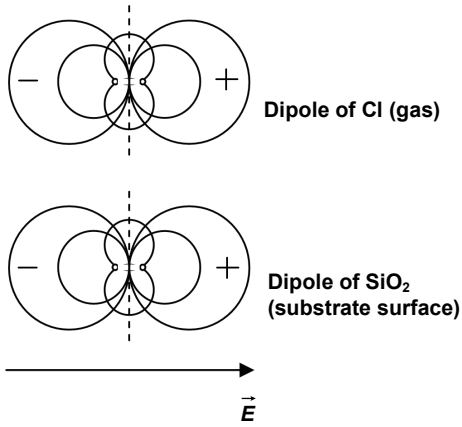

Fig. 6. The orientation of the dipoles of Cl and SiO_2 in the near field while irradiating the substrate from above orthogonal surface plane

Conclusion. We propose a method of photochemical sub-nano-polishing using evanescent wave, which allows to use near-field component of the electromagnetic field is ~$1/r^3$, is much more effective than the previous [1], wherein was used only the radiation field component is ~$1/r$, which is much weaker than the near-field component in the near zone. As a result, the velocity of photochemical sub-nano-polishing process using the evanescent wave will be much higher than in previous experiments.

At constant external pressure of arbitrary molecular gas optical near field enables to continuously transform it into an atomic gas with subsequent local use of the latter. Using the optical near field (including evanescent wave) enables nano-localization of chemical reactions. This method can be used in nanotechnology and nanochemistry.

REFERENCES

1. *Nomura W.* Nonadiabatic Near-Field Optical Polishing and Energy Transfers in Spherical Quantum Dots / W. Nomura, T. Yatsui, M. Ohtsu // Progress in Nano-Electro-Optics VII. – Berlin : Springer-Verlag (Springer Series in Optical Sciences), 2010. – Vol. 155. – P. 113–130.

2. *Никольский В. В.* Электродинамика и распространение радиоволн / В. В. Никольский. – М. : Наука, 1973.

3. *Огенко В. М.* Теория колебаний и переориентаций поверхностных групп атомов / В. М. Огенко, В. М. Розенбаум, А. А. Чуйко. – К. : Наук. думка, 1991.

4. *Сидоренко В. С.* Особливості ближнього поля диполя Герца / В. С. Сидоренко, Ю. О. Гайдай, С. В. Жила. // Вісн. Київ. нац. ун-ту імені Тараса Шевченка, 2005. – С. 365–372.

Submitted on 12.10.16

Д. Василенко, асп.,
В. Григорук, д-р фіз.-мат. наук,
В. Сидоренко, канд. фіз.-мат. наук,
кафедра квантової радіофізики,
факультет радіофізики, електроніки та комп'ютерних систем,
Київський національний університет імені Тараса Шевченка, Київ

ОПТИЧНЕ БЛИЖНЬОПОЛЬОВЕ СУБНАНОПОЛІРУВАННЯ ПОВЕРХНІ ДІЕЛЕКТРИКІВ ІЗ ВИКОРИСТАННЯМ ФОТОХІМІЧНОЇ РЕАКЦІЇ

Розглянуто спосіб полірування нанонеоднорідностей поверхні кварцевої підкладинки за допомогою оптичної ближньопольової диполь-дипольної взаємодії атомарного хлору з молекулами кварцу. Атомарний хлор отримано шляхом фотодисоціації молекулярного хлору оптичним ближнім полем нанонеоднорідностей кварцевої підкладинки. Поляризацію атомів хлору та молекул кварцу здійснено еванесцентною хвилею, яка генерується на поверхні підкладинки при її опроміненні зеленим лазерним випромінюванням з протилежного боку під кутом, не меншим ніж кут повного внутрішнього відбиття.

Ключові слова: фотодисоціація, субнанополірування, оптичне ближнє поле, еванесцентна хвиля, нанонеоднорідності поверхні, диполь-дипольна взаємодія.

Д. Василенко, асп.,
В. Григорук, д-р физ.-мат. наук,
В. Сидоренко, канд. физ.-мат. наук,
кафедра квантовой радиофизики,
факультет радиофизики, электроники и компьютерных систем,
Киевский национальный университет имени Тараса Шевченко, Киев

ОПТИЧЕСКОЕ БЛИЖНЕПОЛЬНОЕ СУБНАНОПОЛИРОВАНИЕ ПОВЕРХНОСТИ ДИЭЛЕКТРИКОВ С ИСПОЛЬЗОВАНИЕМ ФОТОХИМИЧЕСКОЙ РЕАКЦИИ

Рассмотрено способ полировки нанонеоднородностей поверхности кварцевой подложки с помощью оптического ближнепольного диполь-дипольного взаимодействия атомарного хлора с молекулами кварца. Атомарный хлор образовано путем фотодиссоциации молекулярного хлора оптическим ближним полем нанонеоднородностей кварцевой подложки. Поляризация атомов хлора и молекул кварца осуществлена эванесцентной волной, которая генерируется на поверхности подложки при ее облучении зеленым лазерным излучением с противоположной стороны под углом, не меньше чем угол полного внутреннего отражения.

Ключевые слова: фотодиссоциация, субнанополирование, оптическое ближнее поле, эванесцентная волна, нанонеоднородности поверхности, диполь-дипольное взаимодействие.

UDC 577.3

V. Gaidar, post grad. stud.,
O. Sudakov, Ph. D.,
S. Radchenko, Ph. D.,
Department of Medical radiophysics,
Faculty of Radiophysics, Electronics and Computer Systems,
National Taras Shevchenko University of Kyiv, Kyiv

DETECTING EPILEPTIC SEIZURES USING STATIONARY WAVELET TRANSFORM

Epilepsy is a common chronic neurological disorder caused by transient and unexpected electrical disturbance of the brain. This paper presents a mechanism by which seizures are detected using a single channel of on-scalp EEG. The proposed approach is based on Stationary Wavelet Transform (SWT) to decomposed the electrocorticography (ECoG) signal into its sub-bands to detect rhythmic discharges of specific frequencies. Afterwards, the modified post-processing procedure was applied for identification of epilepsy seizure.

Keywords: epilepsy, ECoG, wavelet transform, neural network, classification, seizure detection.

Introduction. Epilepsy is one of the world's most common neurological diseases, affecting more than 40 million people worldwide. Epilepsy's hallmark symptom, seizures, can have a broad spectrum of debilitating medical and social consequences [1].

The term epilepsy covers a large set of brain disorders whose main symptom is the occurrence of so-called epileptic seizures. There is no consensus among researchers regarding the definition of epilepsy and epileptic seizures. The most widespread and accepted definition of an epileptic seizure which is also used in textbooks [2] and within the clinical practice guidelines is as follows [3]: *epileptic seizures* are suddenly occurring and transient dysfunctions of the central nervous system due to abnormal neuronal activity in the cortex.

Understanding of this dynamic disease evolves; new possibilities for treatment are emerging. An area of great interest is the development of devices that incorporate algorithms capable of detecting early onset of seizures or even predicting those hours before they occur. This lead time will allow for new types of interventional treatment. In the near future a patient's seizure may be detected and aborted before physical manifestations begin.

Despite the fact that EEG is an important clinical tool for diagnosing, monitoring and managing neurological disorders, distinct difficulties associated with EEG analysis and interpretation, which hindered its wide-spread acceptance. Traditional method of analysis of the EEG is based on visually analyzing the EEG activity using strip charts. This is laborious and time consuming task which requires skilled interpreters, who by the nature of the task are prone to subjective judgment and error. Furthermore, manual analysis of the temporal EEG trace often fails to detect and uncover subtle features within the EEG which may contain significant information, Hence many researchers are working to develop an automated tool which easily analysis the EEG signal and revel important information present in the signal.

Electrocorticography or intracranial EEG is an EEG directly recorded from the exposed surface of the cerebral cortex during surgery. This recording technique has a higher spatial resolution on plain EEG and is used to localize epileptic foci prior to an epilepsy surgery. Amplitudes recorded with ECoG are manifold higher than in ordinary EEG recordings. Furthermore, ECoG is less prone to biological and technical artefacts.

The problem of automated seizure detection is the first step towards tackling many related problems, such as seizure prediction, prevention, and early seizure abortion [4]. Automated seizure detection and prediction have been extensively studied in the context of human epilepsy [5]. Yet some of the more challenging problems in particular seizure abortion and prevention using neurostimulation methods, are currently being studied in animal models of epilepsy (both in-vitro and in-vivo). Thus it is important to develop solid seizure detection techniques for these animal models also.

The work described below uses data from live *(in-vivo)* rats with chronic epileptiform activity. The ECoG recording was obtained at Bogomoletz Institute of Physiology of NAS of Ukraine.

Description of the Methods. *Data pre- processing.* For implementation of the seizure detection method, a general data pre- processing cycle has been implemented. This pre-processing cycle consists of three steps:

- noise cancellation
- power line interference cancellation (at 50 Hz)
- moving average with a Gaussian window

The first step provided by finding the coefficient of variation (CV) which is a relative measure of statistical dispersion. Given a discrete time series $x[n]$ the coefficient of variation

$$C_V(x[n]) = \frac{\sigma(x[n])}{\mu(x[n])} \quad (1)$$

where $\sigma(x[n])$ – the ration of standard deviation, $\mu(x[n])$ – the mean value. All ECoG recording which do have a small $C_V(x[n])$, i. e. $C_V(x[n])^2 < 0.05$ will be ignored. Those data are suspected to contain less information, because amplitudes can hardly be distinguished from the noise.

The next step is to center time series $x[n]$ by subtracting the mean $\mu(x[n])$ to create a zero mean time series:

$$x[n] = x[n] - \mu(x[n]) . \quad (2)$$

The EEG recordings are prone to power-line interference. Even on ECoG recordings power-line interference may have influence. That is why a 50 Hz notch filter is applied.

Both physiological and pathological EEG activity can be commonly observed in the range of 0.5–30 Hz [6]. ECoG themselves are often recorded with a considerably higher sampling rate, i/e/ greater than 200 Hz (in our study $f_s = 416$ Hz). This over sampling might complicate seizure detection using methods which analyze the morphology of the recording, i.e. searching for specific patterns. This issue can be solved by smoothing. In this work, a moving average with a Gaussian window with a default length of 50 ms . Finally, a convolution of the time series and the Gaussian windows is performed.

Stationary wavelet transform. In general, the he wavelet transform $w_x(b,a)$ can be calculated by equation [7]:

$$w_x(b,a) = \mid a \mid^{1/2} \int_{-\infty}^{\infty} x(t) \cdot \psi^*\left(\frac{t-b}{a}\right) dt \quad (3)$$

The function $\psi(t)$ is called a wavelet ("small wave") or wavelet function, eq. 3 is a *continuous wavelet* transform (CWT), and $w_x(b,a)$ is also called the *wavelet coefficient* of $x(t)$ at scale a and transitional value b . Having the wavelet coefficient and $\psi(t)$ the time series $x(t)$ can be recovered using the inverse CWT.

The discrete wavelet transform (DWT) is a decomposition of the time series $x(t)$ which can be understood as a successive band-pass filtering and downsampling. $x(t) = x_0(t)$ is decomposed into two parts: $y_1(t)$ representing the high-frequent parts of $x_0(t)$ and $x_1(t)$ representing the low-frequent parts.

The DWT is computationally fast and can be implemented by successive filter banks, and thus is an important tool in signal and image processing [7]. Unfortunately, the DWT is not shift-invariant when applied to discrete time series $x(t)$, i. e. if the input time series $x(t)$ is shifted, the resulting coefficients may differ severely. Therefore the stationary wavelet transform [8] was invented. Principally, the SWT is DWT, but the downsampling step is replaced by an upsampling. For the seizure detection we need to detect rhythmic discharges of frequency characteristics of specific frequencies. In context of EEG analysis, two wavelets are commonly used: the Daubechies 4 (Fig. 1) wavelet [9] and the *Symlet 5* wavelet [10]. In this work, the db4 wavelet has been used.

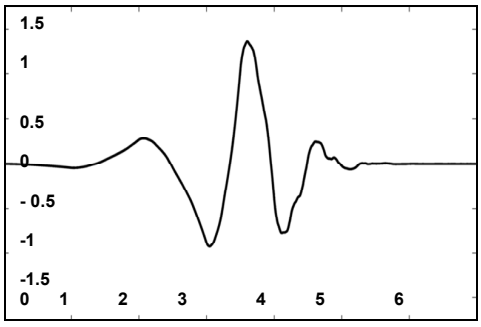

Fig. 1. The wavelet function ψ for a Deubechies 4 wavelet

After SWT for each scale a the calculated coefficients can be considered as a time series $\chi_a[n]$. Since the different scales cause a different scaling of the coefficients, the $\chi_a[n]$ need to be normalized (eq. 4) to be compared among each other.

$$\chi_a[n] = \frac{\chi_a[n]}{\max(\chi_a[n])}. \quad (4)$$

The mean of the $\chi_a[n]$ is calculated (eq. 5) resulting in a time series $\sum[n]$:

$$\sum[n] = \mu(\chi_a[n]). \quad (5)$$

A threshold ϑ_1 is calculated using standard deviation σ of the time series $\sum[n]$ and a variable parameter λ which has to be provided by the user (eq. 6):

$$\vartheta_1 = \lambda \cdot \sigma(\sum[n]) \quad (6)$$

This threshold is then applied to $\sum[n]$, such that all values greater that ϑ_1 are labeled 1, else 0. The result is a binary time series $\beta_1[n]$.

Data post- processing. In the previous section we reviewed the single seizure detection methods generate binary time series named $\beta_1[n]$ representing the indices where a specific feature indicate the presence of a seizure. These seizures need to be classified as epileptic or non-epileptic. Therefore, the indices have to be translated into possible seizure onsets and offsets. The post-processing procedure is given on Fig. 2 [11]

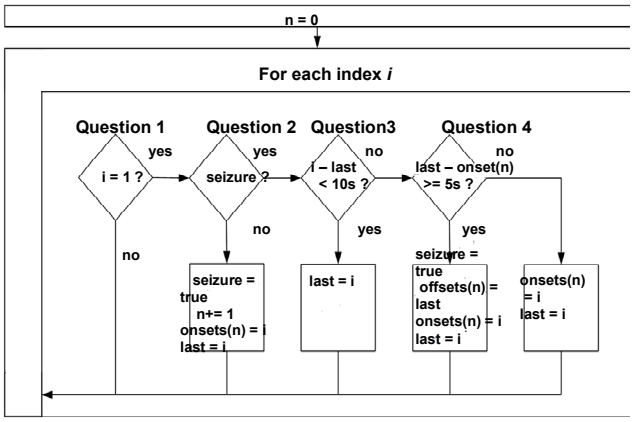

Fig. 2. Flowchart of the post-processing routine

The number of accepted seizures is given by the counter n, thus initialized with 0. For classification lets consider the general sequence of epileptic seizures [11] schematically shown in Fig. 3

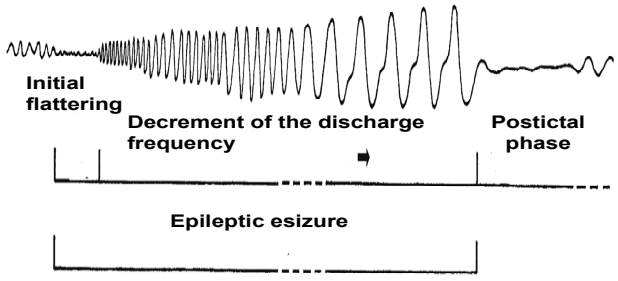

Fig. 3. Schematic representation of the temporal sequence of focal epileptic seizures

The initial flattening, an unspecific reaction similar to the flattening and desynchronisation of cortical activity caused by strong environmental stimuli, that indicates begin of a seizure. The discharges frequency decreases during the ictal period, whereas the amplitude increases. After the termination of the seizure, there is the postictal phase described by low activity. The first detectable discharges often occur with frequencies of 15 Hz. This discharge frequency decreases during the ictal period, whereas the amplitude increases. The decrement of the discharge frequency is crucial to identify these patterns as epileptic reactions.

The number of accepted seizures is given by the Counter n, thus initialized with 0. Each index $i = 1...$ data size is checked whether it is an epileptic seizure set or non-epileptic. A minimum ictal phase of $5s$ is assumed and the minimum interictal phase of $10\,s$.

Rezults. In our case we had a data from live (in-vivo) rats with chronic epileptiform activity collected from one channel intracranial EEG electrode. The ECoG recording was obtained at Bogomoletz Institute of Physiology of NAS of Ukraine.

The obtained data is recorded in $x[n]$. The sampling rate of EEG dataset is 416 Hz. After the preprocessing cycle we obtained the data shown in Fig. 4.

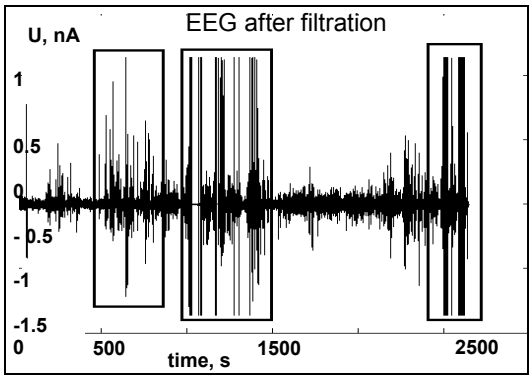

Fig. 4. The original ECoG dataset after pre-processing

The seizure detection method based on stationary wavelet transform was applied. In context of analysis we used the Daubechies 4 mother wavelet. After that, for each scale a, the calculated coefficients can be considered as a time series $\sum[n]$. All values of $\sum[n]$ greater than threshold value are labeled 1, else 0. The result is a binary time series. The results after seizers classification is shown at Fig. 5

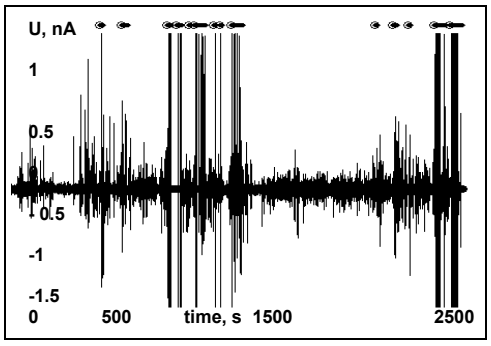

Fig.5. The binary time series indicating where an epileptic seizures was detected

In Fig. 5 as dots marked binary time series that classified as epileptic seizures, and as '*o*' seizures that are not considered as epileptic.

For determine the effectiveness of implemented methods of epileptic seizures detection we need to evaluate such parameters as *sensitivity* and *specificity*.

Therefore, the true positive rate (TPR) and the false positive rate (FPR) were calculated for all datasets of 1,5 hours (in average) ECoG recordings. Considering the obtained sensitivity ≥ 88 % and specificity ≥ 96 % for the SWT methods, this method seems to provide results with sufficient precision and could be implemented to create the expert system of ECoG datasets analysis.

Conclusions. Currently there is a great deal of interest in developing efficient methods to predict and prevent the onset of seizures in epileptic patients. Our results indicate that analogous to humans, a seizure event in a rat model can be detected with high accuracy using stationary wavelet analysis. Thus, in further it provides an opportunity to create expert systems for classification of ECoG signals and diagnosis the epilepsy seizures or even predicting those hours before they occur.

REFERENCES

1. *Tong S.* Engineering in Medicine & Biology Quantitative EEG Analysis Methods and Clinical Applications/ S. Tong and N. V. Thacor // Boston; London : Artech House, 2009.

2. *Hacke W.* Epilepsien Neurologie / W. Hacke // Springer, 2010. – P. 363–392.

3. *Elger C. E.* Erster epileptischer Anfall und Epilepsien im Erwachsenenalter / C. E. Elger // In Diener HC and Weimar C: Leitlinien für Diagnostik und Therapie in der Neurologie, 2012.

4. *Guillaume S.* Automatic Seizure Detection in an In-Vivo Model of Epilepsy: Computational Physiology / S. Guillaume, P. Joelle : papers from the AAAI 2011 Spring Symposium, 15.11.04 // School of Computer Sci., McGill University, Montreal, Quebec, Canada, 2011.

5. *Mormann F.* Seizure prediction: the long and winding road / F. Mormann, R. G. Andrzejak, C. E. Elger and K. Lehnertz // Brain: a journal of neurology, 2007. – Vol. 130. – P. 314–333.

6. *Engel J.* What should be modeled? Models of seizures and epilepsy / J. Engel, P. A. Schwartzkroin // In Pitkänen: Elsevier, 2006. – P. 1–14.

7. *Mertins A.* Die Wavelet-Transformation // Springer Vieweg : Signaltheorie, 2013. – 3-rd edition. – P. 301–354.

8. *Nason G.P.* The Stationary Wavelet Transform and some Statistical Applications/ G. P.Nason, B. Silverman // Wavelets and Statistics : Lecture Notes in Statistics, 2002. – Vol. 103. – P. 281–299.

9. *Performance* reassessment of a real-time seizure-detection algorithm on lo0ng ECoG series / I. Osorio, M. G. Frei, J. Giftakis et al. // Epilepsia, 2002. – Vol. 43(12). – P. 1522–1535.

10. *Statistical* mapping of scalp-recorded ictal EEG records using wavelet analysis / J. J. Battiston, T. M. Darcey, A. M. Siegel et al. // Epilepsia. – Vol. 44(5). – P. 664–672.

11. *Christian W.* Automatic Seizure Detection in Rats using ECoG: A Comparison of Methods / W. Christian. – Lübeck, den 11. September 2013.

Submitted on 08.06.16

В. Гайдар, студ.,
О. Судаков, канд. фіз.-мат. наук,
С. Радченко, канд. фіз.-мат. наук,
кафедра медичної фізики,
факультет радіофізики, електроніки та комп'ютерних систем
Київський національний університет імені Тараса Шевченка, Київ

ДЕТЕКТУВАННЯ ЕПІЛЕПТИЧНИХ НАПАДІВ З ВИКОРИСТАННЯМ СТАЦІОНАРНОГО ВЕЙВЛЕТ-ПЕРЕТВОРЕННЯ

Епілепсія є поширеним хронічним неврологічним розладом, викликаним тимчасовою і непередбачуваною електричною активністю головного мозку. Розглянуто механізм, за допомогою якого епілептичні напади фіксуються з використанням одноканальної електроенцефалограми (ЕЕГ), знятої з поверхні кори головного мозку. Запропоновано підхід, заснований на використанні стаціонарного вейвлет-перетворення (СВП), що розкладає сигнал електрокортікограми (ЕкГ) у його піддіапазони для виявлення ритмічних збурень. Дану модифіковану процедуру обробки даних застосовано для ідентифікації епілептичних нападів.

Ключові слова: епілепсія, ЕЕГ, вейвлет-перетворення, нейронна мережа, класифікація, детектування нападів.

В. Гайдар, студ.,
О. Судаков, канд. физ.-мат. наук,
С. Радченко, канд. физ.-мат. наук,
кафедра медицинской физики,
факультет радиофизики, электроники и компьютерных систем,
Киевский национальный университет имени Тараса Шевченко, Киев

ДЕТЕКТИРОВАНИЕ ЕПЕЛЕПТИЧЕСКИХ ПРИПАДКОВ С ИСПОЛЬЗАВАНИЕМ СТАЦИОНАРНООГО ВЕЙВЛЕТ-ПРЕОБРАЗОВАНИЯ

Эпилепсия является распространенным хроническим неврологическим расстройством, вызваннім временной и непредсказуемой электрической активностью головного мозга. Рассмотрен механизм, с помощью которого эпилептические припадки фиксируются с использованием одноканальной электроэнцефалограммы (ЭЭГ), снятой с поверхности коры головного мозга. Предложен подход, которій основан на использовании стационарного вейвлет-преобразования (СВП), что разбивает сигнал електрокортикограмы (ЭКГ) на его поддиапазоны для выявления ритмических возмущений. Данная модифицированная процедура обработки данных применена для идентификации эпилептических припадков.

Ключевые слова: эпилепсия, ЭЭГ, вейвлет-преобразования, нейронная сеть, классификация, детектирования приступов.

UDK 537.311.33

V. Gandzyuk, stud.,
V. Grygoruk, Dr. Sci.,
L. Ishchuk, Ph. D.,
Y. Onysko, Adv. Eng.,
S. Pavlyuk, Ph. D.,
O. Solomenko, Ph. D.,
Department Electrophysics,
Faculty of Radio Physics, Electronics and Computer Systems,
Taras Shevchenko National University of Kyiv, Kyiv

HEATING TEMPERATURE DETERMINATION OF THE "SILICON STRUCTURE WITH DIELECTRIC INSULATION"

This paper describes a method of determining the temperature, based on the calculation of the I-U curve of the silicon structure, prepared with technology "silicon with dielectric insulation" (SSDI) and comparing it with experimental I-U curve. The results of the SSDI heating temperature were compared with estimated from spectral measurements.

Keywords: method, temperature, silicon structure, dielectric insulation, spectral measurements.

There are various methods for the semiconductor temperature determining: using a thermocouple [6], using semiconductor conductivity dependence on the temperature [3, 5] etc. But all these methods can not be applied in this case because of the small size of structures [4].

The purpose of this study was to compare the proposed method of determining the temperature based on the calculated *I-U* curve of SSDI and its comparison with experimental *I-U* curve. The results of the SSDI heating temperature were compared with estimated from spectral measurements.

Determine the conditions necessary for the evaluation of temperature T. At the point x_m, where the temperature obtains the highest value T_m, the rate of change in concentration of electron-hole pairs $g = 0$. At this point it is defined only by generation (recombination) and diffusion, and at low concentrations also by bipolar drift. If the first process mostly affects the concentration of pairs and pair lifetime τ much smaller than the time of the temperature change, then at the point x_m implemented the thermodynamic equilibrium concentration of electrons n and holes p.

Thus, for values of temperature $T_m > T_i$ values of concentrations of electrons and holes are defined using equations $n = p = p_i(T_m)$, where $p_i = 7{,}54 \cdot 10^{15} T^{3/2} \exp(-6493/T)$ thermodynamic equilibrium concentration of electron-hole pairs in silicon with intrinsic conductivity (p_i was defined in [cm^{-3}], T – in [K]). The current flowing through the silicon film, quasistationary varies with temperature and can be defined as

$$I = wd_{Si} e p_i(T_m) \left\{ \nu_n \left[E(x_m), T_m \right] + \nu_p \left[E(x_m), T_m \right] \right\}. \quad (1)$$

Here ν_n and ν_p – drift velocity of electrons and holes, $E(x_m)$ – the electric field, w – characteristic size of the structure.

In equation (1) the value of the electric field $E(x_m)$ replaced with average value U/a (U – voltage across the sample, a – sample length). Using empirical expressions for the drift velocity [2]:

$$\nu_n = \frac{1{,}42 \cdot 10^9 T^{-2,42} E}{\left[1 + \left(E / 1{,}24 T^{1,68} \right)^{0,46 T^{0,17}} \right]^{1/2{,}57 \cdot 10^{-2} T^{0,66}}},$$

$$\nu_n = \frac{1{,}31 \cdot 10^8 T^{-2,2} E}{\left[1 + \left(E / 1{,}24 T^{1,68} \right)^{0,46 T^{0,17}} \right]^{1/0{,}46 \cdot T^{0,17}}}, \quad (2)$$

dependence $I(T_m, U)$ was calculated. Comparing with recent experimental *I-U* curves, obtained at $U > U_i$, the temperature T_m was defined. Said replacement does not lead to significant errors in determining T_m, because of the dependence $p_i(T_m)$ current (1) depends on $1/T_m$ approximately exponentially, while its dependence on $(\nu_n + \nu_p)$ and $E(x_m)$ is linear. Thus, the dependence T_m vs $E(x_m)$ is weak.

Let's estimate the error at determination of the temperature T_m. This error is due to the electric field value replacement to $E(x_m)$ by mean value U/a along the sample. Because of this change, drift velocity of electrons and holes (2) were determined with an error. This leads to that calculated using the formula (1) are referred to the temperature error. Estimation of error gives the maximum 5 % [1].

It should be noted that in the worst case considered in determining the error when it was taken to consider the greatest possible difference in values ν. So in fact it even less.

Some temperature values T_m and concentration $p_i(T_m)$ is shown on Fig. 1 at appropriate experimental points. When the current is increased, increasing the temperature from 1100K to 1320 K and carrier concentration from $1{,}8 \cdot 10^{16}$ cm^{-3} to $5{,}7 \cdot 10^{17}$ cm^{-3}. At voltage value U_i the temperature $T_m = T_i = 810$K, and the concentration p_i was $1{,}5 \cdot 10^{16}$ cm^{-3}, which is three times higher than the initial concentration of carriers in the silicon film.

The properties of the structure changed irreversibly, when at $U \approx 8\,\mathrm{V}$ temperature structure reached values 1800 K, and flowed through it direct current I_{st} .

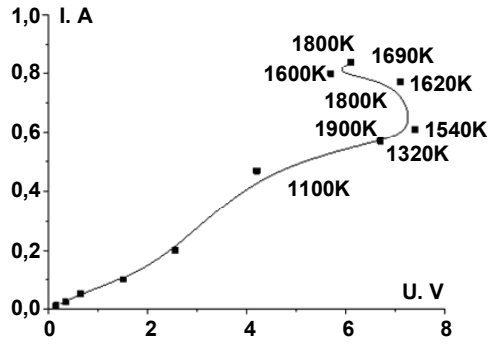

Fig. 1. I-U curve of SSDI. The numbers to the left of the curve near the experimental points marked spectral values, and the right – the calculated value by equation (1)

Study of system parameters was performed by emission spectrometry. The emission spectra registration procedure uses the system which consists of optical fiber, the spectral unit S-150-2-3648 USB, and the computer. Fiber is focusing on the light strip in the middle of the working sample. The spectrometer works in the wavelength range from 650 to 1100 nm. The computer is used in both control measurements process and data processing, received from the spectrometer.

Fig. 2 shows the emission spectrum of the system during work: current – 0.62 A, voltage – 6.9 V.

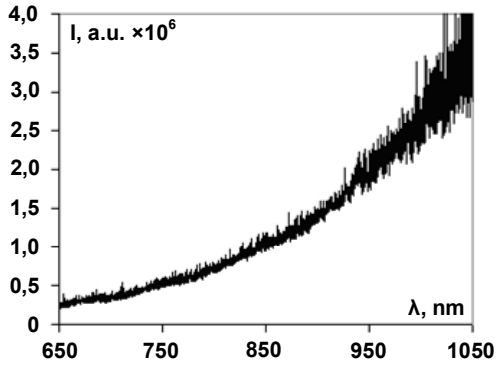

Fig. 2. Typical emission spectrum of the system

Based on the continuous nature of the emission spectra, we compared the experimental results with the calculated spectra of the blackbody radiation. Calculations have been performed by using Planck's formula:

$$I = \frac{hc^2}{\lambda^5}\left[\exp\left(\frac{hc}{kT\lambda}\right) - 1\right]^{-1}. \qquad (3)$$

Fig. 3 shows the comparison of the experimentally measured emission spectrum (current – 0.77 A, voltage – 7.1 V) with the calculated spectra of blackbody radiation computational grid with step of 300 K in the temperature range from 1500 K to 2100 K. All spectra are normalized to the intensity, which is located at a wavelength of 850 nm. Fig. 2 shows that the spectrum corresponds to a temperature of 1800 ± 300 K.

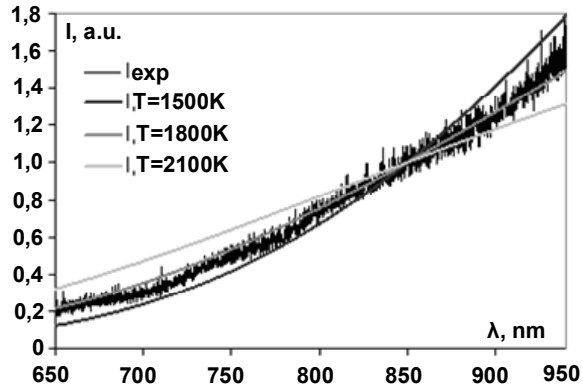

Fig. 3. Comparison of experimentally measured emission spectrum with the calculated spectra of black body radiation

Analyzing the results, we can conclude that theproposed methods for self-heating temperature measuring of the SSDI complement each other. Calculation method gives the most accurate results in a high field (current values 0.5–0.6 A), and the spectral method – in sufficient brightness (current values 0.6–0.9 A).

REFERENCE

1. Blakemore J. Statistics of electrons in semiconductors / J. Blakemore (in rus.). – M. : Mir, 1964.

2. Electron and Hole Drift Velocity Measurements in Silicon and Their Empirical Relation to Electric Field and Temperature/ C. Canali, G. Majni, R. Minder, G. Ottaviani // IEEE Trans. Electron Devices, 1975. – ED-22, № 11. – P. 1045–1047.

3. Dobrovolsky V. N. Thermal gradient-drift domain in the electron-hole plasma in germanium / V. N. Dobrovolsky, S P. Pavlyuk (in rus.) // FTP, 1981. – Vol. 15. – № 1. – P. 120–129.

4. Dobrovolsky V. N. Self-organization in SOI FET / V. N. Dobrovolsky, G. K. Ninidze, L. V. Ishchuk. // Microelectronic Engineering, 2004. – Vol. 72. – № 1–4. – P. 383–387.

5. Gordov A. N. Basics pyrometry / A. N. Gordov (in rus.). M. : Metallurgiya,1971.

6. Sosnovsky A. G. Temperature measurement / A. G. Sosnovsky, N. I. Stolyarova (in rus.). – M. :Izd. standartov, 1970.

Submitted on 30.12.16

В. Гандзюк, студ.,
В. Григорук, д-р фіз.-мат. наук,
Л. Іщук, канд. фіз.-мат. наук,
Ю. Онисько, пров. інж.,
С. Павлюк, канд. фіз.-мат. наук,
О. Соломенко, канд. фіз.-мат. наук,
кафедра електрофізики,
факультет радіофізики, електроніки та комп'ютерних систем,
Київський національний університет імені Тараса Шевченка, Київ

ВИЗНАЧЕННЯ ТЕМПЕРАТУРИ РОЗІГРІВУ КРЕМНІЄВОЇ СТРУКТУРИ З ДІЕЛЕКТРИЧНОЮ ІЗОЛЯЦІЄЮ

Описано метод визначення температури, який базується на розрахунку вольт-амперної характеристики (ВАХ) кремнієвої структури, виготовленої за технологією "кремній з діелектричною ізоляцією" (КСДІ) і порівнянні її з експериментальною ВАХ. Отримані результати визначення температури порівнюються з оцінками розігріву КСДІ-структури за допомогою спектральних досліджень.

Ключові слова: метод, температура, кремнієва структура, діелектрична ізоляція, спектральні дослідження.

В. Гандзюк, студ.,
В. Григорук, д-р физ.-мат. наук,
Л. Ищук, канд. физ.-мат. наук,
Ю. Онысько, вед. инж.,
С. Павлюк, канд. физ.-мат. наук,
Е. Соломенко, канд. физ.-мат. наук,
кафедра електрофизики,
факультет радиофизики, электроники и компьютерних систем,
Киевский национальный университет имени Тараса Шевченко, Киев

ОПРЕДЕЛЕНИЕ ТЕМПЕРАТУРЫ РАЗОГРЕВА КРЕМНИЕВОЙ СТРУКТУРЫ С ДИЭЛЕКТРИЧЕСКОЙ ИЗОЛЯЦИЕЙ

Описан метод определения температуры, основанный на расчете вольт-амперной характеристики (ВАХ) кремниевой структуры, изготовленной по технологии "кремний с диэлектрической изоляцией" (КСДИ) и сравнении его с экспериментальной ВАХ. Полученные результаты определения температуры сравниваются с оценками разогрева КСДИ-структуры с помощью спектральных исследований.

Ключевые слова: метод, температура, кремниевая структура, диэлектрическая изоляция, спектральные исследования.

UDC 621.385

I. Drozd, assist.,
A. Kuzmichev, Ph. D.
A. Pinkavsky, stud.
Department of Electron Devices,
Faculty of Electronics
National Technical University of Ukraine "KPI", Kyiv

HIGH-VOLTAGE FULL-CONTROLLED GAS DISCHARGE COLD-CATHODE TETRODE

The construction and operation of a high-voltage tetrode on the base of high-density magnetron glow discharge with cold cathode are considered. The tetrode operates in the thyratron mode as a closing switch, in the tacitron mode as a closing/opening switch and as a tacitron with automatic limitation of maximum anode current.

Key words: gas discharge tetrode, cold cathode, magnetron discharge, thyratron, tacitron, current limiter.

Introduction. Gas discharge switch devices such as thyratrons, spark gaps, and ignitrons have enjoyed great success in closing-switch pulse applications (in radar and laser technique, plasma technology, *etc.*) where high pulse currents must be switched from high-voltage energy storage on short time scales with low forward-voltage drop during conducting period (FVD) [1, 3]. At the same time, gas discharge devices are not usually considered as repetitive fast opening switches, although there are some devices, which are able to open the pulse circuits or interrupt high currents at high voltage [1, 6]. Such devices are desired for enhancing pulse rate and simplifying pulse circuit topology. A good example is tacitrons (low-pressure gas discharge triodes with very dense grid) [1]. It works as thyratrons during ignition and conduction periods, but as vacuum triodes during switch-off period; hence, the tacitrons may be considered as a high-voltage fully controlled switch. The tacitrons, due to high switched voltage but low FVD, occupy the niche between high-voltage vacuum tubes with high FVD and low-voltage high-power transistors [1]. Unfortunately, tacitrons contain hot thermionic cathode with well known demerits, therefore the development of tacitrons with a cold cathode is the vital problem. The cold cathode may provide long lifetime, fast readiness and other relevant excellent parameters. This work deals with development and investigation of the tacitron-type cold cathode tetrode with two control grids, which can not only interrupt the current but limit (restrict) this current, too. Besides, the tetrode will be study as a tandem switch device, in which the 2nd grid is used as an anode of the first cascade for amplification of the triggering signal and control of recovery of anode voltage hold-off.

Electrode structure and operation of experimental gas discharge tetrodes. The electrode structures of experimental tetrodes is built on the base of the inverted gas-magnetron [4] consisting from a hollow non-externally-heated (cold) cathode 1 and a coaxial auxiliary pre-ionizing electrode 2, which are surrounded by permanent magnet with axial field (Fig. 1). The cathode diameter is 40 mm. The 1st and 2nd grids, respectively 3 and 4 in Fig. 1, have disk-like shape and annular slots of 3 mm width. In experimental tetrode № 1, the annular grid slots are covered by dense molybdenum wire mesh. In tetrodes № 2, the 1st grids have no mesh covering. In both the tetrodes, gaps (d) between all grid disks and between the 2nd grid and the plat anode 5 equal 5 mm. The cathode is made from molybdenum (Mo shows itself as weakly sputtered cold cathode material in hydrogen discharges). The grids and the anode are made from X18H10T steel disks of 0.5 mm thick. The tetrode electrode structures have been mounted inside sealed glass envelopes of industrial thyratrons. The hydrogen filling is due to Ti-H generators disposed within the envelopes. The hydrogen pressure p = 10–40 Pa and is regulated by heating the Ti-H generators.

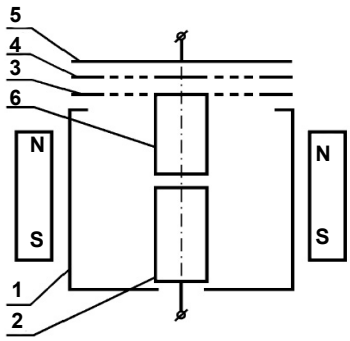

Fig. 1. Schematic structure of experimental tetrodes: 1 – hollow cold cathode, 2 – auxiliary pre-ionizing discharge electrode; 3–1st grid; 4–2nd grid; 5 – anode; 6 – supplemental element for facilitating the firing of the starting discharge to the 1st grid

Fig. 2 depicts the operational electrical scheme for investigation of the gas discharge tetrodes.

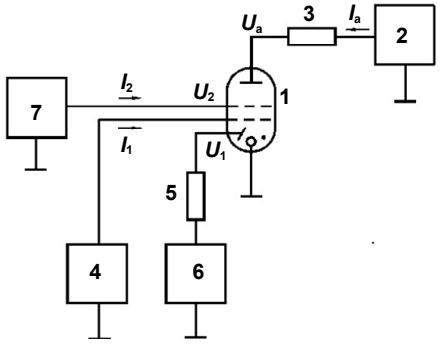

Fig. 2. The operational electric scheme: 1 – tetrode, 2 – high voltage supply (anode energy storage), 3 – load, 4 – starting (triggering) pulse generator for the 1st grid, 5 – ballast resistor, 6 – power source for the auxiliary pre-ionization electrode (for supplying the auxiliary pre-ionization discharge), 7 – control pulse generator for the 2nd grid

The DC power source 6 applies a positive voltage (~ 250 V) to the electrode 2 (Fig. 1) and maintains the auxiliary pre-ionization glow magnetron discharge with current of some tens of milliamperes in the cathode cavity. This discharge stabilizes firing a starting discharge between the cathode and the 1st grid after applying a positive pulse from generator 4 to this grid. If current of the starting discharge I_1 is higher of some critical value I_{cr}, and the anode current I_a also becomes higher than a critical one, the main discharge is established between the anode and the cathode though the openings (slots) in the grids. For triggering the tetrode, a positive pulse with peak voltage of 1–3 kV may be applied to the 2nd grid, too; but triggering is possible even with the grounded 2nd grid at

very high starting current (up to and higher 160–180 A) to the 1st grid. The high voltage supply 2 with capacitor energy storage provides anode voltages U_a up to 20 kV and pulse anode current of the main discharge I_a up to 600 A at pulse duration 1–4 μs.

Some words about the type of discharge supported by cold cathode. The average cathode current density reaches 0.1–10 A/cm^2. The average current density in the openings (slots) in the grids and on the anode reaches 2.5-250 A/cm^2. So, the high density glow magnetron discharge between the common cathode, on the one hand, and the grids and the anode, on the other hand, occurs in the tetrode. The crossed electric and magnetic fields (**E**×**H**) within the cathode cavity provides beautiful conditions for gas ionization by secondary cathode electrons, emitted due to bombardment of the cathode surface by plasma ions, and generation of dense discharge plasma [4]. The effect of enhancing gas ionization in **E**×**H** field is due to enlarging secondary electron trajectories at low pressures. The plasma surface in the openings of the 1st grid serves as an electron emitter for the anode part of the device. The current of emitted electrons is amplified by some gas ionization on the path to the anode and initiates the main discharge. From this moment, the closing/conductive phase of the switching process is established. Closing time, determined by anode voltage fall from U_a down to FVD (ΔU_a), is order of 0.1 μs.

The products of gas pressure p and gaps d between the grids and between the 2nd grid and the anode are very small (d = 5 mm); that is corresponding to pd values at the left of the left branch of Paschen curve. Hence, the self-maintained discharges between the grid disk and the anode are impossible (as in vacuum) and we have the combination of gas discharge part (in the cathode cavity) with vacuum conditions in the grid/anode part. However, said above ion generation by electrons emitted through the 1st grid and partial ion compensation of electron space charge in the anode part make the different case as compared with the real vacuum tetrode tube. The electron charge compensation by ions provides low FVD of gas tetrode relatively vacuum tubes.

Results of tetrode № 1 investigation. The experiments with tetrode № 1 showed there are three ranges of operation parameters and three associated with them operation modes. Consider them for U_a = 10 kV.

The first range relates to the usual thyratron mode. The conditions for this mode are: the 1st grid current $I_1 > I_{cr.1}$ at the 2nd grid voltages $0 < U_2 < 3.5$ kV ($I_{cr.1}$ ~ 160–180 A at $U_2 = 0$ and $I_{cr.1}$ ~ 10 A at U_2 = 3,5 kV). This mode provides only closing operation. The value of anode current is determined by the anode circuit. The dense plasma fills the space from the cathode to the anode with contraction of the plasma column in the grid openings. The tetrode structure with two dense grid ensures recovery of anode voltage hold-off for several microseconds (Table 1).

The second range relates to the tacitron mode with the possible anode current interruption, *i.e.* it ensures the full control. For this: $I_{cr.2} < I_1 < I_{cr.1}$, 1.5 kV < U_2 < 2.5 kV, $I_{cr.2} \le 60$ A. In this operation mode the value of anode current is determined by the anode circuit as in the thyratron mode. However, the decrease of U_2 down to negative values (~ –300 V at $I_a \le 75$ A) or even to zero (at $I_a \le 50$ A) interrupts the anode current for several tenths of microsecond (Table 1). Such effect occurs due to the relatively thick ion sheet (δ) surrounding the mesh wires covering the slot of the 2nd grid at negative or zero voltage (δ becomes larger half of distance between the wires) and, ultimately, blocking passage of electrons through the slot towards the anode. Blocking is possible due to negative potential of the 2nd grid relatively the local plasma potential and formation of the potential barrier for electrons within the grid openings.

Table 1

The parameters of the experimental tetrode № 1

Operation mode	Maximum pulse anode current, A	Maximum cathode current density, A/cm^2	Maximum anode current density, A/cm^2	Anode voltage hold-off recovery, μs
Thyratron	500	10	250	8
Tacitron*	75	1,5	35	0,7
Current limiter*	5–18	0.4	9	0,3

Peak pulse anode voltage U_a: 10 kV. Average anode current $I_{a.av}$: 150 mA; Anode pulse duration: 1–4 μs; Voltage drop in active mode ΔU_a: 300–650 V, Closing time, determined by anode voltage fall: ~ 0.1 μs.
* The opening time is determined by anode voltage hold-off recovery.
The current density through the grid openings and the anode current density are suggested to equal each other.

The third range relates to the current-limiting mode with saving possibility of the anode current interruption. For this I_1 = 10–25 A, U_2 = 0.7–1.5 kV. Such mode is very interesting for practical applications; therefore consider factors affecting the value of restricted anode current. Fig. 3 illustrates capability of the device to limit (restrict) anode current in the case of shorted load circuit. The case was modeled by shunting the anode load resistor with a thyratron. One can see, our device behaves in this case as a vacuum electron tube of beam tetrode type. Fig. 3 shows the maximum possible values of the anode current for the given I_1, U_2 and U_a. The less current values at the same U_a and U_2 are determined by the load resistance and I_1.

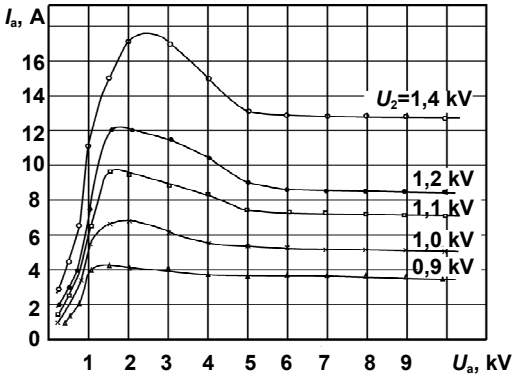

Fig. 3. Anode current I_a dependence on anode voltage U_a and control pulse voltage U_2 when load resistance equals zero. I_1 = 25 A

We can propose the following explanation of curve behavior in Fig. 3. Firstly, the main discharge to the anode is a non-self-maintained one supported by the discharge on the 1st grid, some plasma particles penetration into the gap 1st grid–2nd grid and then plasma electron penetration into the anode gap. Moreover, the latter forms a beam-like flow in the gap before the anode. The current in the anode gap is transferred by an electron beam emitted by low dense plasma cloud below the 2nd grid and passing through the grid slot. The existence of the beam-like flow is due to small *pd* in the anode gap and anode current density less than 10 A/cm^2 (at such conditions the anode plasma does not form [2]). The case is similar to electron processes in the vacuum beam tetrode and plasma cathode electron sources [5]. Secondly, the maximum on the curves at U_a ~ 2 kV may be caused by some gas ionization with the electron beam and electrons reflected from the anode. At higher values of U_a the cross section of electron ionization decreases and electron beam amplification is weak. Thirdly, the growth of the anode current at the beginning (U_a ~ 0.5–1 kV) with the growth of U_a may be caused by attracting plasma electrons by the anode field through the 2nd grid slot and due to less capture of electrons by the mesh wires of the 2nd grid.

Table 1 presents the main parameters of the experimental tetrode № 1. The values of current densities on the anode and through the grid openings were determined by the ration of I_a to the aria of the opening (slot) in the 1st or 2nd grid. The average anode current $I_{a.av}$ was limited by value of 150 mA by reason of using the glass envelope for the experimental tetrode and bad cooling of its electrodes.

Results of tetrode № 2 investigation. The experiments with tetrode № 2 showed its characteristics are similarly to ones of the tetrode № 1 and demonstrate the possibility to work in thyratron and tacitron modes. In the thyratron mode, the tetrode № 2 passes maximal currents, which equal to values shown in Table 1. However, the value $I_{cr.1}$ is much smaller: for instance, the value of $I_{cr.1}$ was about of 1 A at U_2 = 3,5 kV against 10 A for the tetrode № 1. Obviously, this is due to higher electrical transparence of the 1st grid in the tetrode № 2 than in the tetrode № 1 with the dense wire mesh on the 1st grid. At the same time the tetrode № 2 saves ability to interrupt the anode current up to 60 A at U_a 10 kV by applying a negative voltage to the 2nd grid in the range 0.1–1 kV. But the time of anode voltage recovery during current interruption is longer (~ 1 μs) against the tetrode № 2.

The current-limiting mode is not realized in the tetrode № 2 in the same measure as in the tetrode № 1. In the tetrode № 2, the cathode plasma species freely diffuse through the wide opening of the 1st grid with relatively small losses and the plasma emitter of electrons towards the anode forms in the close vicinity of the 2nd grid slot. It facilitates firing the self-maintained discharge with non-limited current to the anode. So, the experiments showed the current-limiting mode in the tetrode № 2 occurs only in the milliampere range and has no practical interest.

The standard method of tetrode triggering consists in applying two pulses to the grids; moreover, the triggering of the 2nd grid needs high voltage and high power pulses in order to generate dense plasma in the close vicinity of the 2nd grid slot but far from the cathode. It was suggested to convert the two-grid tetrode into the tandem two-cascade switch device controlled by one pulse of low voltage and low power applied only to the 1st grid. In this case the 2nd grid will be serve as an anode of the first cascade; the power supply of the 2nd grid may be of DC type.

The electrical scheme depicted in Fig. 4 has been use for carrying out the experiments with the tetrode № 2 as the tandem switch. Its difference relatively the scheme in Fig. 1 consists in modification of the 2nd grid circuit. This circuit contains two capacitive energy storages 8 and 10, which are discharged after ignition of the starting discharge on the 1st grid. The discharge of capacitors 8 and 10 may be interpreted as the second starting discharge for initiation of discharge to the anode and triggering the tetrode as the whole. Thus, both the grids together with the cold cathode present a first stage (cascade) of the tetrode where the 2nd grid serves as a temporary anode. Respectively, the anode part of the tetrode may be considered as a second stage (cascade) of the tandem switching device.

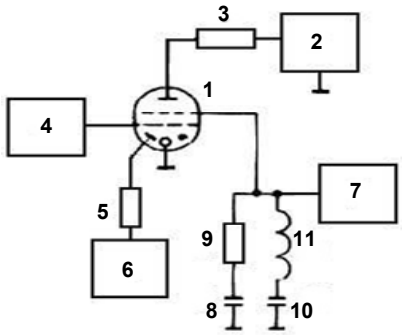

Fig. 4. The operational scheme for tandem switching: 1 – tetrode, 2 – high voltage supply (anode energy storage), 3 – load, 4 – starting pulse generator for the 1st grid, 5 – ballast resistor, 6 – DC power source for supplying the auxiliary pre-ionization discharge, 7 – DC power source of positive voltage for charging capacitors 8 and 10, 9 – ballast resistor, 11 – coil for recharging capacitor 10

The capacitor 8 provides fast growth of the 2nd grid current and fast filling of the gap below this grid with plasma. The capacitor 10 together with coil 11 provides the desired duration τ of positive pulse of 2nd grid current as well as recharging the capacitor 10 from positive to negative voltage. The value of τ is to correspond to the duration of anode current pulse. Thus, the negative potential of the 2nd grid must act in the post-discharge period during recovering the electrical (anode voltage) hold-off of the tetrode. Fig. 5 demonstrates behavior of the 2nd grid voltage U_2 during the whole pulse process.

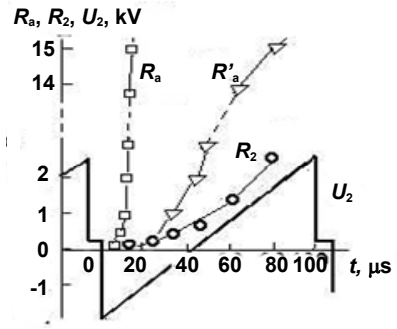

Fig. 5. Recovery of anode (R_a) and 2nd grid (R_2) voltage hold-off and time diagram of U_2 for operation with pulse rate of 10 kHz. I_a = 500 A, τ = 4 μs, the voltage of the charged capacitors 8 and 10 equals 2.5 kV

Testing of the tandem switching devices has been fulfilled in the thyratron mode in order to determine the possibility of realization of the tandem mode. The experiments confirm reality of such operation.

The next part of experiments with the tetrode № 2 dealt with post-discharge processes and characteristics. In particular, we study recovery of electrical hold-off of the tetrode. This parameter determines the maximum voltage applied to an electrode but not causing electrical breakdown or self-firing of a discharge to the electrode. For measurement of recovery characteristics we used the special scheme, in which the first pulse generator passed a pulsed current through the tetrode and then, with some regulated delay, the second pulse generator applied a pulsed high voltage to the

tetrode. The recovery characteristic depicts values of the minimum breakdown voltage at different delays after the finish of tetrode current pulse.

The 2nd grid circuit provides not only firing the second starting discharge for initiation of discharge in the anode gap but also creating conditions for fast recovery of electrical hold-off of the anode gap in the post-discharge period. The former takes place due to the positive voltage of the capacitors 8 and 10 in the pre-discharge period; the latter occurs due to the automatic recharge of the capacitor 10 from positive to negative voltage during the conductive period. Fig. 5 (the R_a curve) shows small delay (~ 5 μs) of the recovery beginning and how quickly grows the electrical hold-off of the anode gap. For the comparison: R'_a curve demonstrates much slower recovery and larger delay (~ 22 μs) of the recovery beginning when the negative voltage is not applied to the 2nd grid in the post-discharge period and the recovery is based only on the deionization process within the grid and anode gaps.

The role of negative bias of the 2nd grid consists in creation of ion sheets around the mesh wires in the grid slot and removal of plasma surface, serving as an electron emitter for the anode gap, below the grid. It leads to shut down of plasma electron emission towards the anode and allows application of voltage to the anode without discharge firing.

The DC power source 7 (Fig. 4) provides the secondary recharging of the capacitors 8 and 10 to positive voltage in order to create conditions for the next pulse switching process as it is shown in Fig. 5 (the U_2 curve). The management of the secondary recharging must take into account the dynamics of electrical hold-off of the 2nd grid. Fig. 5 (the R_2 curve) depicts recovery characteristic of this grid. One can see the hold-off recovery of the 2nd grid is much slower than the hold-off recovery of the anode. This may be explained by the high electrical transparence of the 1st grid for the 2nd grid field respectively the electrical transparence of the 2nd grid for the anode field.

In our case, the secondary recharge of the capacitors 8 and 10 needs at least 100 μs (see Fig. 5, the U_2 curve), and maximal pulse rate will be 10 kHz. The high pulse rate is also possible, e. g. 40 kHz, but the control method similar to one employed for control of the tetrode № 1 should be used: at the first 25 μs of the post discharge period, the negative voltage is to apply to the 2nd grid; then positive pulses are applied to both the grids for triggering the tetrode.

Conclusion. The experiments with cold cathode tetrodes based on the dense magnetron glow discharge showed there are three ranges of operation parameters and three associated with them operation modes: the thyratron mode as a closing switch, the tacitron mode as a closing/opening switch and as a tacitron with automatic limitation of maximum anode current. The tetrode may be used as the tandem switch device with the 2nd grid as a temporaty anode of the first cascade. Such approach allows to use only one starting pulse applled to the 1st grid for triggering the tetrode. The choice of higher electrical tranparence of the 1st grid allows realizing the internal amplification of starting pulses in the tandem mode and decreasing the power of the control generator.

REFERENCES

1. *Bochkov V. D.* Impulsnye gazorozryadnye kommutiruyushie pribory / V. D. Bochkov, Yu. D. Korolev // Encyclopedia nizkotemperaturnoy plazmy. Vvodnyy tom. Kniga IV. – M. : Nauka, 2000. – S. 446–459.

2. *Boldasov V. S.* A low-pressure, non-self-maintained high-voltage discharge / V. S. Boldasov, A. I. Kuz'michev and D. S. Fillipychev // Radiophysics and Quantum Electronics, 1984. – Vol. 27. – № 7. – P. 656–663.

3. *Gas* Discharge Closing Switches / ed. by G. Schaefer, M. Kristiansen. and A. Guenther. – N. Y. : Plenum Press, 1990.

4. *Kuzmichev A.* Magnetronnye raspylitelnye sistemy / A. Kuzmichev. – Kiev : Avers, 2008.

5. *Oks E.* Plasma Cathode Electron Sources: Physics, Technology, Applications / E. Oks. – Weinheim : Wiley-VCH Verlag, 2006.

6. *Schumacher R. W.* Low-pressure plasma opening switches / R. W. Schumacher, R. J. Harvey // Opening switches ; ed. by A. Guenther, M. Kristiansen and T. Martin. – N. Y. : Plenum Press, 1987. – P. 93–129.

Submitted on 16.10.16

І. Дрозд, асист.
А. Кузьмичов, канд. техн. наук,
О. Пинькавський, студ.,
кафедра електронних приладів та пристроїв,
факультет електроніки,
Національний технічний університет України "КПІ", Київ

ВИСОКОВОЛЬТНИЙ ПОВНОКЕРОВАНИЙ ГАЗОРОЗРЯДНИЙ ТЕТРОД ІЗ ХОЛОДНИМ КАТОДОМ

Розглянуто конструкцію і роботу високовольтного тетрода на основі щільного магнетронного тліючого розряду з холодним катодом. Тетрод працює в тиратронному режимі як вмикаючий прилад, у тасітронному режимі – як вмикаючий/вимикаючий прилад, а як тасітрон – з автоматичним обмеженням максимального анодного струму.

Ключові слова: газорозрядний тетрод, холодний катод, магнетронний розряд, тиратрон, тасітрон, обмежувач струму.

И. Дрозд, ассист.,
А. Кузьмичёв, канд. техн. наук,
А. Пинькавский, студ.,
кафедра электронных приборов и устройств
факультет электроники
Национальный технический университет Украины "КПИ", Киев

ВЫСОКОВОЛЬТНЫЙ ГАЗОРАЗРЯДНЫЙ ТЕТРОД С ПОЛНЫМ УПРАВЛЕНИЕМ И ХОЛОДНЫМ КАТОДОМ

Рассмотрены конструкция и работа высоковольтного тетрода на основе плотного магнетронного тлеющего разряда с холодным катодом. Тетрод работает в тиратронном режиме как включающий прибор, в таситронному режиме – как включающий/выключающий прибор и как таситрон – с автоматическим ограничением максимального анодного тока.

Ключевые слова: газоразрядный тетрод, холодный катод, магнетронный разряд, тиратрон, таситрон, ограничитель тока.

UDC 537.525:621.325

I. Melnyk, Dr. of Tech. Sci.,
I. Chernyatynshkiy, stud.,
N. Piasetska, stud.,
Electronic Devices Department, Electronic Faculty,
National Technical University of Ukraine "Igor Sikorskiy Kiev Polytechnic Institute", Kyiv

ITERATIVELY METHODIC OF SIMULATION OF TROIDE HIGH VOLTAGE GLOW DISCHARGE ELECTRODES SYSTEMS WITH TAKING INTO ACCOUNT THE TEMPERATURE AND MOBILITY OF SLOW ELECTRONS IN ANODE PLASMA

Iteratively methodic of accuracy simulation of energy distribution and the time of discharge current rising in the high voltage glow discharge electrodes systems with taking into account the temperature and mobility of electrons in the anode plasma is considered in this article. The designation feature of proposed methodic is relatively high accuracy of calculations and absence the necessity of references to do not verified approximated discharge plasma parameters from the literature. The calculations provided iteratively and interrupted, when the positions of anode plasma boundary, calculated from the sides of the cathode-fall region and of anode plasma was equal with specified required accuracy. Obtained simulation results are in good agreement both with the results, published early, and with obtained experimental data.

Keywords: high voltage glow discharge, triode electrodes system, electrical control of discharge current, anode plasma, electrons' temperature in plasma, electrons' mobility in plasma, iteration algorithm.

Introduction. High Voltage Glow Discharge (HVGD) electron sources are widely used in industry for electron beam welding of thin-wall items in the medium of soft vacuum, for deposition of chemically-complex ceramic coatings in the medium of active gases, for annealing of different materials and parts of mechanisms, as well as for refining of refractory materials [2, 7, 8]. It caused by the advantages of this type of electron sources, which are follows:

– possibility of providing the technological operations in the soft vacuum in the medium of different gases, including noble and active ones;

– relative cheapness of the sources and of electron-beam technological equipment, including evacuation system;

– relative simplicity of realizing control of beam current by continuous changing the pressure in technological chamber;

– providing of very high quality of produced items and low percent of its defects [2, 7, 8].

But for providing advanced electron-beam technologies, based on the HVGD electron sources, in the modern electronic, instrument making industry, mechanical engineering and metallurgy, fast and precision control of the power of formed electron beam is usually necessary. It is caused by necessity of producing the identically items with required electrical, mechanical and thermodynamic parameters without unsuitable deflections and defects [2, 7, 8]. Therefore using of gas-dynamic control systems with the time regulation constant range of few second [5] is not very suitable to such applying of these sources. By that reason using of triode HVGD electron sources with changing the anode plasma (AP) parameters by lighting of additional low voltage discharges is very perspective for further development of those technologies [3, 11]. Its allows also applying the impulse regime of operation of this types of electron source, which lead to possibilities of obtaining new crystal and film materials with unique properties [2, 7, 8].

The main technical problem for further realization of electron-beam technologies, based on triode HVGD electron sources in the different branches of industry, is absence of accuracy model of such electrodes systems with defining and taking into account thermodynamic anode plasma parameters. Proposed early model is mainly correct and adequate, however it is not closed parametrically, because the approximated thermodynamic parameters of anode plasma not calculated, but taking from the scientific literature [3, 11]. Therefore today the forming of correct and adequate model of triode HVGD gap on the base of pervious investigations with taking into account AP parameters, such as electrons' temperature and mobility, is very actual scientific task. This article is devoted to the describing the general method of solving this complex problem.

Main physical and geometrical parameters of simulated triode electrodes' system. The structure scheme of triode high voltage glow discharge electrodes' system with ring-like additional electrode for lighting of non self-sustained arc discharge is presented on the Fig. 1. It must be pointed out, that another form of additional electrode, for example cylindrical or plain, is also possible, but in any case the physical conditions of discharge maintaining must be corresponded to hollow cathode regime [4].

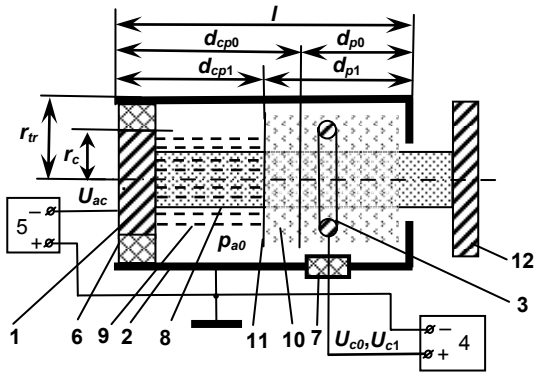

Fig. 1. Scheme of HVGD triode electrodes system and its supplying. 1 – cathode; 2 – HVGD anode; 3 – ring-like electrode for lighting of additional discharge; 4 – low-voltage power source for lighting of additional discharge; 5 – high-voltage power source; 6 – high-voltage insulator, 7 – low-voltage insulator, 8 – electron beam, 9 – ions' flow; 10 – anode plasma, 11 – plasma boundary, 12 – treated item

It is clear from the Fig. 1, that main geometrical parameters of triode HVGD electrodes' system are follows.

1. Longitude size of discharge gap l.

2. Transversal size of discharge gap d_{tr}.

3. Distance from the cathode surface to the AP boundary d_{cp}.

The main electrical parameters of the considered system are follows.

1. Acceleration voltage U_{ac}, applied between the cathode 1 and HVGD anode 2 of electron source.

2. Voltage of additional discharge U_c, applied between the HVGD anode 2 and additional electrode 3. It mast be pointed out, that for additional discharge, corresponding to the circuit scheme, presented at Fig. 1, HVGD anode 2 is considered as the cathode.

It is also important, that for the impulse regime of operation of triode HVGD electron source must be considered two different values of voltage of additional discharge U_c, namely: voltage in impulses U_{c1} and voltage in pauses between impulses U_{c0}. [8]. Position of plasma boundary, as was pointed out in the papers [3, 9–11], is depended from the control voltage U_c, therefore in impulse regime of operation two values of cathode-plasma distance d_{cp} are considered. Value d_{cp1} corresponded to the voltage on additional electrode in impulse U_{c1}, and value d_{cp0} – to the voltage U_{c0}. In HVGD electrodes systems increasing of particles concentrations in AP corresponded to its greater volume and to smallest value of d_{cp}, therefore for impulse regime of HVHD lighting relation

$$d_{cp0} > d_{cp1}, \qquad (1)$$

is always satisfied [3, 9, 11]. Corresponded geometry model of HVGD electrodes' system is also presented at the Fig. 1. In some formulas except cathode-plasma distance d_{cp} using of plasma longitude size d_p is more suitable, therefore corresponded geometry values, which are connected and defined as

$$d_p = l - d_{cp}, \qquad (2)$$

are also considered at Fig. 1.

In the papers [3, 9–11] also have been pointed out, that important internal parameter of HVGD is the residual pressure in the chamber of electron source p_{a0}. It is clear, that this parameter also take the significantly influence to the concentration of charged particles in AP, to its volume, and, as a result, to the current of formed electron beam.

Other internal parameters of considered model of triode HVGD electrodes' system are defined both by the conditions of interaction of charged particles flows and by the level of gas ionization in AP, and these parameters are follows [1, 3, 9–13].

1. T_e – temperature of slow electrons in anode plasma.

2. μ_{e0} – mobility of electrons' in anode plasma.

3. γ_a – secondary ion-electron emission coefficient from anode surface

4. η_i and η_U – coefficients of electrons reflection from the anode by the current and by the voltage correspondently.

5. f – transparent coefficient for electrons in anode plasma.

6. $\overline{Q_{i0}}$ – average cross-section of accelerated ions scattering at the residual gas atoms.

7. k_e – coefficient of longitude of electrons' trajectories.

8. U_i – potential of gas ionization.

9. A_i, a_i, α_i – empirical constants for defined operation gas and electrodes material, which are usually defined experimentally.

Value of all these internal model parameters are strongly depended form acceleration voltage U_{ac}, voltage of additional discharge U_c, residual pressure p_{a0} and geometry sizes of electrodes' system. Most of those coefficients are taking from the scientific literature or defined experimentally for real conditions of discharge lighting [1, 10, 12, 13], but thermodynamic parameters of anode plasma can be calculated by using iterative method, which will be described beyond.

Defining of anode plasma boundary position relatively to the cathode surface and energetic efficiency of electron source by considering the interaction of fluxes of charged particles in cathode-fall region.

Corresponding with proposed algorithm on the first step of calculation position of plasma boundary defined with taking into account the physical conditions in cathode-fall region. For the conditions of HVGD lighting AP volume defined through gas ionization by the fast beam and slow plasma electrons, through the interaction of accelerated ions with the atoms of residual gas and through the emission processes on the cathode surface. Taking into account all this processes, written and analytically solved the equation of discharge self-consistent [3, 9–12]. Corresponded analytical solution can be written as follows [3, 9–12]:

$$R_1 = A_i U_{ac}^{-a_i}\left(A_i U_{ac}^{-a_i} + 1\right)\sqrt{\frac{kT_e + eU_d}{2\pi m_e}}, \; R_2 = f\eta_i\eta_U^{-a_i}k_e,$$

$$R_3 = 3\left(kT_e + eU_d\right)N_0\alpha_i\sqrt{\frac{kT_e + eU_d}{2\pi m_e}}\,\mathrm{e}^{-\frac{U_i}{\frac{kT_e}{e}+U_d}},$$

$$R_4 = \mu_{e0}\left(kT_e + eU_d\right)\left(\frac{\pi}{p_{a0}}\right)^2\left(1+\frac{\gamma d_{tr}}{\lambda_e}\right), \qquad (3)$$

$$R_5 = R_1R_2p_{a0}Q_{ep0}, \quad C_{eq} = -\frac{R_1 + R_3 + R_1R_2}{R_5},$$

$$D_{eq} = \frac{R_4}{R_5}, \quad p = -\frac{C_{eq}^2}{3}, \quad q = \frac{2C_{eq}^3}{27} + D_{eq},$$

$$D = \left(\frac{p}{3}\right)^3 + \left(\frac{q}{2}\right)^2,$$

$$u = \sqrt[3]{-\frac{q}{2} + \sqrt{D}}, \; v = \sqrt[3]{-\frac{q}{2} - \sqrt{D}}, \quad y = u + v,$$

$$\lambda_e = \frac{2.25kT_e\left(eU_d + kT_e\right)^2}{\pi e^4 p_{a0}\ln\left(1.5 - \sqrt{\frac{kT_e\left(eU_d + kT_e\right)^3}{\pi p_{a0}}}\right)}, \; d_p = y - \frac{C_y}{3},$$

where λ_e – free path of electrons in anode plasma, R_1, R_2, R_3, R_4, R_5, p, q, u, v and y – additional variables, C_{eq} and D_{eq} – coefficient of solved cubic equation, D – discriminate of this equation. With known volume of AP and, as a result, concentration of ions in it, currents of the main discharge I_{md} and of additional discharge I_{ad} are defined from equations [3, 9–11]:

$$C_1 = A_i U_{ac}^{-a_i}\left(1 + A_i U_{ac}^{-a_i}\left(1 + \eta_i\eta_u^{-a_i}\left(1 - f\left(1 - d_p p_{a0}Q_{ep0}\right)\right)\right)\right),$$

$$C_4 = 3N_0\alpha_i\sqrt{\frac{e\left(kT_e + eU_d\right)}{2\pi m_e}},$$

$$C_2 = \frac{\pi^2\mu_{i0}}{\left(d_p p_{a0}\right)^2}\left(1+\frac{\gamma d_{tr}}{\lambda_e}\right) - C_4,$$

$$C_3 = C_2\left(kT_e + eU_d\right)\mathrm{e}^{-\frac{U_i}{\frac{kT_e}{e}+U_d}}, \qquad n_i = \frac{C_1}{C_3},$$

$$I_{md} = r_c^2 n_i\left(1 + A_i U_{ac}^{-a_i}\right)\sqrt{\frac{\pi e d_p\left(kT_e + eU_d\right)}{2m_e}}; \qquad (4)$$

$$I_{ad} = en_i\pi r_{tr}\left(1+\gamma\right)\left(r_{tr} + 2d_p\right)\sqrt{\frac{2eU_d}{m_i}}.$$

As a result, with known voltages and currents, energetic efficiency of triode HVGD electrodes' system η_t can be calculated by simple formulas [3, 11]:

$$\eta_d = 1 - \frac{2 + k_e\left(1 + 2k_e\gamma\mu_{e0}\right)}{2k_e\left(1+\gamma k_e\right)}, \qquad k_e = lp_{a0}\overline{Q_0}, \qquad (5)$$

$$\eta_t = \frac{\eta_d}{1 + \frac{\eta_d U_d I_d}{U_{ac} I_e}},$$

where η_d – energetic efficiency of diode electrodes' system, which have the same current of main discharge.

Defining of temperature of electrons and its mobility in anode plasma. In the early investigations problem of using equations (3 – 5) for estimation of energetic efficiency of HGGD electrodes' systems was in defining thermodynamic parameters of AP, such as temperature of slow electrons T_e and its' mobility μ_{e0} [3, 9–11], because these parameters takes from the literature [1, 12, 13] without verification. Another way of providing such calculations is defining these parameters by solving the thermodynamic equation for discharge plasma [14, 16]:

$$\frac{e^2 n_e E^2}{m_e\left(\nu_{ea} + \nu_{ei}\right)} = \frac{3kn_e}{2}\left(\left(T_e - T_a\right)\delta_{ea}\nu_{ea} + \left(T_e - T_i\right)\delta_{ei}\nu_{ei}\right), \qquad (6)$$

where ν_{ea} – frequency of collision of electrons with the gas atoms, ν_{ei} – frequency of collision of electrons with the ions, δ_{ea} – part of energy, which transfer from the atoms to electrons, δ_{ei} – part of energy, which transfer from the ions to electrons, T_a – temperature of atoms, T_i – temperature of ions.

For the weekly ionized HVGD plasma, where the condition

$$\frac{n_e - n_i}{n_e} << 1$$

is fulfilled, analytical solving of equation (6) for the temperature of electrons T_e is [14, 16]:

$$T_e = \frac{eU_c}{2k}\left(1 + \sqrt{1 + \frac{\pi e^2 m_i}{6m_e}\left(\frac{U_{ac} d_{cp}}{p_{a0}\overline{Q_{ea}}}\right)^2}\right). \qquad (7)$$

From equation (7) the relation to the cathode plasma distance can be rewritten as:

$$d_{cp} = \frac{p_{a0}\overline{Q_{ea}}}{U_{ac}}\sqrt{\frac{6m_e}{\pi e^2 m_i}\left(\left(\frac{2kT_e}{eU_c} - 1\right)^2 - 1\right)}. \qquad (8)$$

Mobility of electrons in the AP μ_{e0} is depended from its temperature T_e and from the frequency of collision electrons with atoms ν_{ea}, which defined as [14, 16]:

$$\nu_{ea} = \frac{U_{ac} d_{cp}}{\sqrt{\frac{3U_{ac} m_e^2}{e m_i}\left(\frac{1}{2}\left(1 + \sqrt{1 + \frac{\pi e^2 m_i}{6m_e}\left(\frac{U_{ac} d_{cp}}{p_{a0}\overline{Q_{ea}}}\right)^2}\right) - 1\right)}}. \qquad (9)$$

The equation for mobility of electrons μ_{e0} with known its temperature and frequency of collision electrons with atoms ν_{ea} from equations (7, 9), and with making assumption, that distribution of electrons' velocity in AP conform to the Maxwell law, can be written as [14, 16]:

$$\mu_{e0} = = \frac{eK_p}{3\nu_{ea} m_e}, \qquad K_p = \frac{\int_0^\infty v_{ea}^4 \exp\left(-\frac{m_e v_{ea}^2}{2kT_e}\right) dv_{ea}}{\int_0^\infty v_{ea}^2 \exp\left(-\frac{m_e v_{ea}^2}{2kT_e}\right) dv_{ea}}. \qquad (10)$$

Since numerical integration of equation (10) is very complicated and lead to irrational using of computer resources, usually simplified approximations for the value μ_{e0} are used. For example, for the nitrogen and air such approximation is usually suitable [16]:

$$\mu_{e0} = \frac{a p_{a0} d_{cp}}{U_{ac}} + b, \qquad (11)$$

where *a* and *b* are empirical constant.

Iterative method of calculation of energetic efficiency of triode HVGD electron sources with using equations (3–5, 7, 8, 11) will be considered in the next section of the article.

Iterative algorithm of calculation of energetic efficiency of triode high voltage glow discharge electron sources. In the general case position of AP boundary in HVGD electrodes' systems defined from the equation of equilibrium of force of strength of electric field from the side of cathode-fall region and pressure of electronic gas from the side of AP. For the physical conditions of HVGD lighting, for considering low ions' temperature and Boltzmann statistic for electronic gas in AP, this condition is formalized by the following equation [6]:

$$\frac{\varepsilon_0 E_e^2}{2} = n_e k T_e, \qquad (12)$$

where ε_0 – dielectric constant, E_e – strength of electric field. Taking into account relation (12), the values of d_{cp}, calculated from equations (3) and (8), must be approximately equal. Assume, that value of d_{cp}, obtained from the equation (3) with using the data from literature for T_e and μ_{e0}, is d'_{cp}, and the value, obtained from the equation (8), is d''_{cp}. Therefore, with using method of gold section [16], averages values of d_{cp}, $d_{cp}^{r_1}$ and $d_{cp}^{r_2}$, iteratively calculated as follows:

$$\frac{d'_{cp} - d''_{cp}}{d'_{cp} - d_{cp}^{r_1}} = \frac{d'_{cp} - d''_{cp}}{d_{cp}^{r_2} - d''_{cp}} = \frac{1+\sqrt{5}}{2}. \qquad (13)$$

After that, for obtained values $d_{cp}^{r_1}$ and $d_{cp}^{r_2}$, from equation (7) calculated the temperature of electrons T_e. Further the values d'_{cp} and d''_{cp} recalculated by the following way:

$$\begin{cases} T_e\left(d''_{cp}\right) - T_e\left(d_{cp}^{r_2}\right) > T_e\left(d'_{cp}\right) - T_e\left(d_{cp}^{r_1}\right), & d'_{cp} = d_{cp}^{r_1}; \\ T_e\left(d''_{cp}\right) - T_e\left(d_{cp}^{r_2}\right) \le T_e\left(d'_{cp}\right) - T_e\left(d_{cp}^{r_1}\right), & d''_{cp} = d_{cp}^{r_2}. \end{cases} \qquad (14)$$

After that the calculations with using equations (3, 7, 8, 11, 13, 14) are repeated, till the condition

$$\left|d'_{cp} - d''_{cp}\right| > \varepsilon \qquad (15)$$

where ε – accuracy of calculations, is satisfied.

Block-scheme of described calculation algorithm is presented at Fig. 2.

Obtained simulation results and its discussion. Tests of proposed iterative calculation algorithm was provided for such parameters of HVGD electrodes' system [3, 9–11, 14, 16]: $l = 7$ sm, $d_{tr} = 7$ sm, $r_c = 5$ sm, $U_i = 18$ V, $a_i = 0.343$, $\gamma_a = 4.6$, $\overline{Q_{ea}} = 5{,}3 \cdot 10^{-19}$ m^{-2}, $\alpha_i = 1.452$, $\eta_i = 0.7$, $\eta_U = 0.95$, $f = 0.99$, $A_i = 3.8 \cdot 10^{-6}$, $a = 2.5 \cdot 10^4 \frac{\text{m}}{\text{s}}$, $b = 25.4 \frac{\text{m}^2}{\text{V} \cdot s}$, acceleration voltage U_{ac} = 10 – 30 kV, voltage of additional discharge U_c = 30 –100 V, residual pressure in the chamber of electron source p_{a0} = 0.2–1 Pa, operation gas – mixing of nitrogen with 5 % of oxygen, cathode material – aluminum, anode material – cooper. Obtained simulation results and corresponded experimental data are shown at Fig. 3.

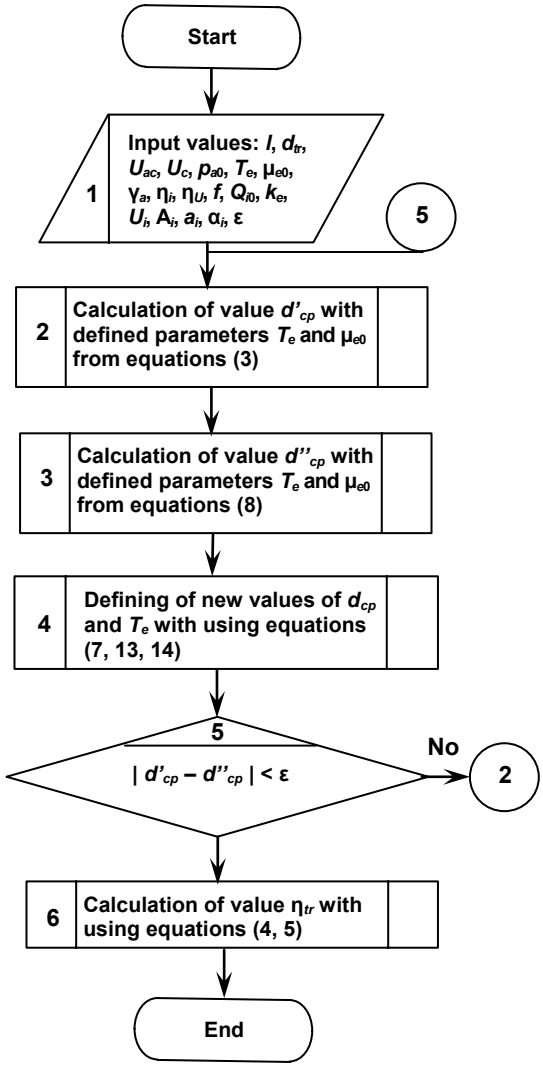

Fig. 2. Block-scheme of considered iterative algorithm of calculation of energetic efficiency of triode HVGD electron sources

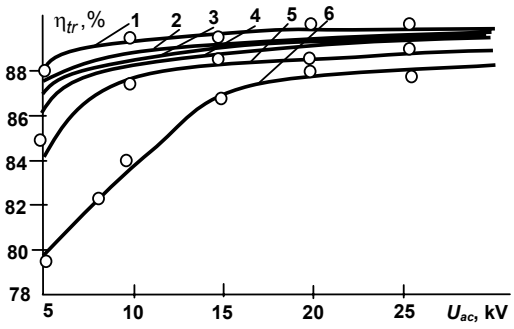

Fig. 3. Calculated and experimental dependences of energetic efficiency of HVGD electron sources from the acceleration voltage for different residual pressure in the volume of discharge gap.
U_c = 50 V. 1 – p_{a0} = 0.2 Pa; 2 – p_{a0} = 0.4 Pa; 3 – p_{a0} = 0.5 Pa; 4 – p_{a0} = 0.6 Pa; 5 – p_{a0} = 0.8 Pa; 6 – p_{a0} = 1 Pa. Experimental results for pressure, corresponded to curves 1, 2 and 6 are marked by the circles

In the paper [10] was proposed the method of calculation of the time of increasing of HVGD current for impulse regime of its' operation. Corresponded equations are:

$$G = \exp\left(-\frac{U_i}{\frac{kT_e}{e} + U_{c1}} \right) \left[\gamma_a \left[\exp\left(\beta_i U_{ac} \right) - 1 \right] - 1 \right], \quad (16)$$

$$t_{fa} = \frac{9kT_e\left(d_{p1} - d_{p0}\right)}{8(\pi e)^3 \mu_{io} \gamma_a G \ln\left(1.5 - \sqrt{\frac{kT_e\left(e\left(U_{c1} - U_{c0}\right)\right)^3}{\pi p_{a0}}} \right)},$$

where β_i – coefficient of gas ionization, t_{fa} – average time of rising of HVGD current. At Fig. 4 presented theoretical and experimental dependences for the time of current increasing from control voltage in impulse U_{c1} and residual pressure p_{a0}. The calculated data, obtained with using described here calculation algorithm, compare in this plot with the pervious results, obtained in paper [10], and with experimental results.

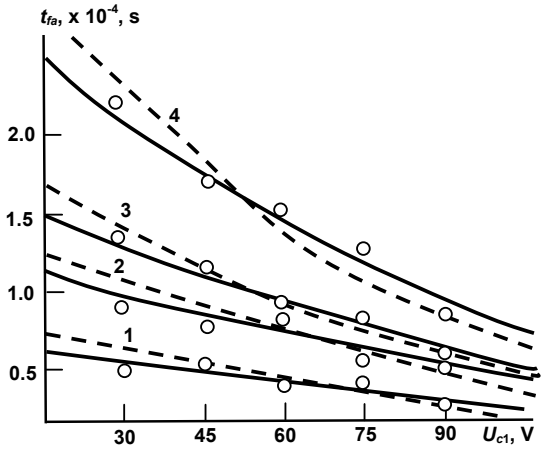

Fig. 4. Calculated and experimental dependences of rising time of HVGD current from the voltage of additional discharge in impulse and from residual pressure. Solid lines – results, obtained with using iterative algorithm, presented in this article, dashed lines – results, obtained in paper [10].
1 – p_{a0} = 0.7 Pa, 2 – p_{a0} = 0.4 Pa, 3 – p_{a0} = 0.3 Pa, 4 – p_{a0} = 0.2 Pa; U_{c0} = 10 V.

Difference between the data, obtained with using proposed iteration algorithm and the results, have been obtained early in papers [3, 9–11], is not grater, then 10–15 %. The graters difference is observed for the small and big values of voltage of additional discharge and residual pressure, because in papers [3, 9–11] was used the values of electrons temperature and mobility in AP for average values of these parameters from literature [1, 12, 13]. In any case, iteration method is more precision, then proposed early, especially for extremely regimes of operation of electron sources, which are mostly interesting to its practical application. Another advantage of proposed iteration method is absence of unnecessary references to data bases with the approximated values of electrons temperature and mobility in AP for different HVGD regimes.

Conclusion. Proposed in this paper iteration algorithm of calculation of energetic parameters of HVGD electron sources and the time of increasing of HVGD current in impulse regime of its operation based on complex analyze of physical processes, taking place in AP, and on defining of thermodynamic plasma parameters without unnecessary references to approximation data from literature and without forming of complex relative databases. Obtained algorithm and the program complex, based on it, can be used in industry for elaboration of new generation of electron-beam equipment with applying of HVGD electron sources.

REFERENCE

1. *Granovskiy V. L.* Elektricheskiy tok v gazah. T. 1. Obschie voprosy elektrodinamiki gazov [Electric current in gases. Vol. 1. General problems of gases' electrodynamics] / V. L. Granovskiy. – M. ; L. : Gosizdat. Fiz.-Mat. Lit-ry, 1952 (in rus.).

2. *Modern* electron beam technologies and equipment for melting and physical vapor deposition of different materials. / M. I. Grechanyuk, A. G. Melnyk, I. M. Grechanyuk et al. // Elektrotechnica and Electronica (E+E). 2014. – Vol. 49, N 5-6. – P. 115–121.

3. *Denbnovetskiy S. V.* Analytical Relations for Calculation the Energetic Efficiency of Triode Glow Discharge Electron Guns / S. V. Denbnovetskiy, I. V. Melnyk, S. B. Tugay // Visn. kyiv. nat. univ. imeni Tarasa Shevchenka. Radiofizika i elektronika", 2014. – N 1/2 (21/22). – P. 37–42.

4. *Investigation* of forming of electron beam in glow discharge electron guns with additional electrode / S. V. Denbnovetsky, V. I. Melnik, I. V. Melnik, B. A. Tugay. – XVIII-th Internat. Symposium on Discharges and Electrical Insulation in Vacuum., Aug. 17–21, 1998, Eindhoven, The Netherlands. Proc. – Vol. 2. – P. 637–640.

5. *Denbnovetsky S. V.* Model of control of glow discharge electron gun current for microelectronics production applications / S. V. Denbnovetsky, V. I. Melnyk, I. V. Melnyk, B. A. Tugay. – Proc. of SPIE. 6th Internat. Conf. on "Material Science and Material Properties for Infrared Optoelectronics", 2003. – Vol. 5065. – P. 64–76.

6. *Iliin V. P.* Chislennye metody resheniya zadach elektrofiziki. [Numerical methods for solving of electrophysics problems] / V. P. Iliin. – M. : Nauka, 1985 (in rus.).

7. *Elektronno-luchevaya* plavka v liteynom proizvodstve [Electron-beam melting in foundry] / S. V. Ladokhin, N. I. Levitskiy, V. B. Chernyavsky at al. – K. : Stal, 2007 (in rus.).

8. *Gas* discharge electron sources – proven and novel tools for thin-film technologies. / G. Mattausch, B. Zimmermann, F. Fietzke et al. // Elektrotechnica and Electronica (E+E), 2014. – Vol. 49, N 5-6. – P. 183–195.

9. *Melnyk I. V.* Analytical calculation of plasma boundary position in high voltage glow discharge under the lighting of additional discharge. / I. V. Melnyk, S. B. Tuhai // Radioelectronic and communication systems, 2012. – Vol. 55, N 11. – P. 50–59.

10. *Melnyk I. V.* Estimation of time of increasing of high voltage glow discharge electron current in the triode electrode system under supply of control impulse / I. V. Melnyk // Radioelectronic and communication systems, 2012. – Vol. 56, N 12. – P. 50–59.

11. *Melnyk I. V.* Issledovanie zavisimosti energeticheskoy effektivnosti triodnyh istochnikov elektronov vysokovoltnogo tleyuschego razryada ot ego parametrov i ot geometricheskih razmerov elektrodnoy sistemy / I. V. Melnyk // Elektronnoe Modelirovanie, 2013. – Vol. 35, N 5. – P. 71–81 (in rus.).

12. *Novikov A. A.* Istochniki elektronov vysokovoltnogo tleyuschego razryada s anodnoy plasmoy [High voltage glow discharge electron sources with anode plasma] / A. A. Novikov. – M. : Energoatomizdat, 1983 (in rus.).

13. *Raizer Yu. P.* Fizika gazovogo razryada [Physic of gas discharge] / Yu. P. Raizer. – M. : Nauka, 1987. (in rus.).

14. *Sinkevich O. A.* Fizika plasmy. Statsionarnye processy v chastichno ionizirovanom gase. Uchebnoe posobie. [Physics of plasma. Stationary processes in the partially-ionised gas. Tutorial] / O. A. Sinkevich, I. P. Stakhanov. – M. : Vysschaya Shkola, 1991 (in rus.).

15. *Vasiliev V. P.* Chislennye metody resheniya ekstremalnyh zadach : ucheb. posobie dlya vuzov. [Numerical methods for solving of extremely problems. Tutorial for institutes of higher education] / V. P. Vasiliev. – M. : Nauka, 1988 (in rus.).

16. *Velikhov E. P.* Fizicheskie yavleniya v gasorazryadnoy plasma. [Physical phenomena in the gas-discharge plasma] / E. P. Velikhov, V. S. Kovalyov, A. T. Rahimov. – M. : Nauka, 1987 (in rus.).

Submitted on 16.10.16

І. Мельник, д-р техн. наук,
І. Чернятинський, студ.,
Н. П'ясецька, студ.,
кафедра електронних приладів та пристроїв,
факультет електроніки,
Національній технічний університет України "КПІ імені Ігоря Сікорського", Київ

ІТЕРАЦІЙНА МЕТОДИКА МОДЕЛЮВАННЯ ТРІОДНИХ ЕЛЕКТРОДНИХ СИСТЕМ ВИСОКОВОЛЬТНОГО ТЛІЮЧОГО РОЗРЯДУ З УРАХУВАННЯМ ТЕМПЕРАТУРИ ТА РУХОМОСТІ ЕЛЕКТРОНІВ В АНОДНІЙ ПЛАЗМІ

Описано ітеранційну методику моделювання розподілу енергії та часу зростання струму розряду в тріодних електродних ситемах високовольтного тліючого розряду з урахуванням температури та мобільності іонів в анодній плазмі. Відмінною рисою методики, яка пропонується, є відносно висока точність розрахунків і відсутність посилань на неперевірені апроксимовані дані з літературних джерел. Розрахунки здійснено ітераційно і припинено, коли положення межі анодної плазми з боку області катодного спадання потенціалу та з боку анодної плазми стає однаковим із наперед заданим ступенем точності. Отримані результати моделювання добре погоджуються як із експериментальними даними, так і з отриманими раніше розрахунковими результатами.

Ключові слова: високовольтний тліючий розряд, тріодна електродна система, електричне керування струмом газового розряду, анодна плазма, температура електронів у плазмі, рухомість електронів у плазмі, ітераційний алгоритм.

И. Мельник, д-р техн. наук,
И. Чернятинский, студ.,
Н. Пясецкая, студ.,
кафедра электронных приборов и устройств,
факультет электроники,
Национальный технический университет Украины "КПИ имени Игоря Сикорского", Киев

ИТЕРАЦИННАЯ МЕТОДИКА МОДЕЛИРОВАНИЯ ТРИОДНЫХ ЭЛЕКТРОДНЫХ СИСТЕМ ВЫСОКОВОЛЬТНОГО ТЛЕЮЩЕГО РАЗРЯДА С УЧЕТОМ ТЕМПЕРАТУРЫ И ПОДВИЖНОСТИ ЭЛЕКТРОНОВ В АНОДНОЙ ПЛАЗМЕ

Описано итерационную методику моделирования распределения энергии и времени увеличения тока разряда в триодных электродных системах высоковольтного тлеющего разряда с учетом температуры и подвижности электронов в анодной плазме. Отличительной чертой предлагаемой методики является относительно высокая точность расчетов и отсутствие ссылок на непроверенные аппроксимированные данные из литературных источников. Расчеты проведено итерационно и прекращено, когда положение границы анодной плазмы со стороны области катодного падения потенциала и со стороны области анодной плазмы становится одинаковым с заранее заданной степенью точности. Полученные результаты моделирования хорошо согласуются как с экспериментальными данными, так и с полученными ранее расчетными результатами.

Ключевые слова: высоковольтный тлеющий разряд, триодная электродная система, электрическое управление током газового разряда, анодная плазма, температура электронов в плазме, подвижность электронов в плазме, итерационный алгоритм.

UDC 539.196.6

S. Radchenko, Ph. D.,
S. Mamilov*, Ph. D.,
I. Hliebova, stud.,
Department of Medical Radiophysics,
Faculty of Radiophysics, Electronics and Computer Systems,
National Taras Shevchenko University of Kyiv
*Institute of Applied Problems of Physics and Biophysics, Kyiv

SIMULATION OF EFFECTS OF OPTICAL RADIATION ON THE OXYHEMOGLOBIN REDUCTION IN BLOOD

A Monte-Carlo simulation of light propagation in tissue was applied for the purpose of better understanding of the results of absorption in different layers in multi-layered tissues. Values of optical parameters used in the model were taken from literature. Simulation results of absorption of different lasers radiation source for each layer of 23 layers tissues are presented. The comparative analysis of experimental research in vivo saturation changes under the influence of radiation and results of simulations light absorption by oxyhemoglobin in blood are presented.

Keywords: Monte-Carlo modeling, tissue optics, photon transport, photodissociation.

Introduction. Optical technologies are put into practice in various areas of modern medicine. For example, the effects of biostimulation and therapeutic effect of low-intensity radiation are currently put to use.

It is known that photodissociation of oxyhemoglobin under the influence of laser radiation from outside through the skin leads to increase of the concentration of the free molecular oxygen in the tissues [3], which can be used to treat burns, bedsores, ulcers and anaerobic infections, as well as other pathologies where compensation of oxygen deficiency in tissues is critical.

It is important to mention that the results of studies of photolysis of hemoglobin that were received in buffer solutions may differ from the effects that take place in the whole blood under the conditions *in vivo*. It is established that with qualitative similarity of photochemical reactions of hemoglobin in natural and modeled conditions (buffer solutions) the effectiveness of phototransformation of protein varies, which authors associate with the antioxidant properties of blood [8]. Numerous experiments show that photodissociation efficiency depends on the wavelength of the incident light [5].

Fig. 1 shows the change in saturation of oxyhaemoglobin in blood caused by the radiation sources with different wavelength.

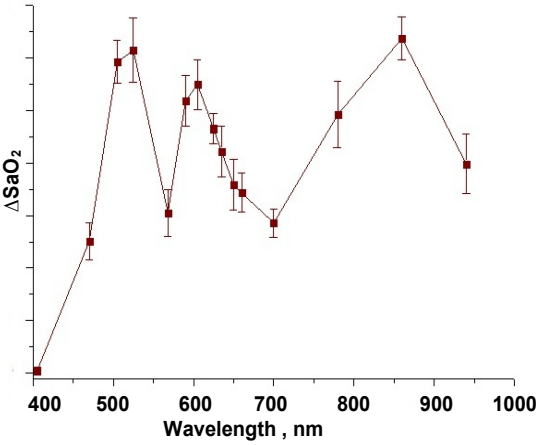

Fig. 1 The change in saturation of oxyhemoglobin in blood caused by the different sources of irradiation

But the theoretical background and explanation of this effect does not exist for today. So at the same time conducting experiments *in vivo* is actual simulating of radiation in biological tissues.

Materials and methods. To simulate the absorption of optical radiation fractions of hemoglobin must be used a method that takes into account several layers of biological tissue with different optical properties and reflection on the boundaries of section layers. It is not important to consider details of energy radiation within a single cell. Therefore numerical Monte – Carlo method is selected, which makes it possible to investigate the light distribution inside biological tissue with a complex multilayered structure.

The advantage of the Monte-Carlo method is that it is a reasonably simple model that can handle arbitrary geometries and that it can provide a direct solution without approximations to the radiative transport equation (RTE).

The downside is the simulation time required which makes it less suitable for inverse problems. The Monte-Carlo method is also limited by noise and the fact that the exact geometry is rarely known. Despite the disadvantages the Monte-Carlo method is considered as "gold standard" in modeling of light propagation within the field of Biomedical optics.

Light transport process is simulated as random walks in which photons histories are recorded as they are scattered and absorbed. The intensity distribution in biological tissues was calculated as a function of the absorption μ_a and scattering μ_s coefficients, anisotropy of scattering g, reflective index n.

For modeling algorithm of Monte-Carlo method was used [4]. The whole area is divided into cells, when the photon is initialed, it is placed to the origin, and initial weight is assigned to it. Then calculate the direction of motion of the photon. The stepsize of the photon is calculated based on the sampling of the probability for the photon's free path S. Each step between photon positions is variable and equals

$$S = \frac{-\ln(1-\mathrm{rnd})}{(\mu_a + \mu_s)}, \qquad (1)$$

where rnd is a random number which is uniformly distributed over the interval [0-1].

When a photon crosses the boundary between two media with different refractive indices it is assigned a new weight. After each move, except the case when the photon goes beyond the medium, the part of photon weight recorded into the cell array, which determines the distribution of energy which was absorbed. The new value of the scattering angle and the free path of photon is generated and the procedure is repeated. If the weight is above a minimum, then the rest of the photon packet is scattered into a new direction and the process is repeated. When a photon weight decreases to a specified small value then roulette is played to either extinguish or continue propagating the photon. If the photon does not survive the roulette, a new photon packet is started. Fig. 2 indicates the basic flowchart for the photon tracing part of the Monte-Carlo calculation [9].

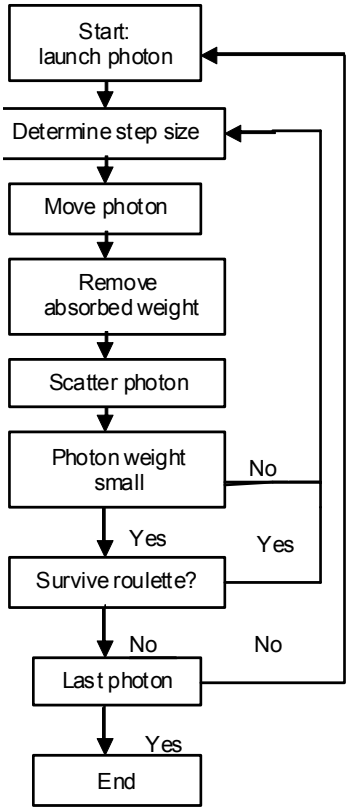

Fig.2 Flowchart for Monte-Carlo simulation of multi-layered tissue

The simulation was performed for the biological object that was used during the experiment which was finger. Phantom for simulation consist of 23 layers and include epidermis, dermis, arterial and venous blood, subcutaneous and muscle tissue, bone. The layers are housed mirror considering anatomical properties. The order number denotes sequence order of layers along ray tracing during the radiation propagation.

1. Epidermis – 0,1mm
2. Dermis – 0,2 mm
3. Arterial blood – 0,45 mm
4. Dermis – 0,9 mm
5. Venous blood – 0,45 mm
6. Subcutaneous tissue – 0,5 mm
7. Muscle – 3 mm
8. Bone – 5,5 mm
9. Muscle – 0,15 mm
10. Subcutaneous tissue – 0,5 mm
11. Venous blood – 0,45 mm
12. Dermis – 0,9 mm
13. Arterial blood – 0,45 mm
14. Dermis – 0,2 mm
15. Epidermis – 0,1mm

Arterial and venous blood were divided into three components in the presence of different forms of hemoglobin: deoxyhemoglobin (Hb), oxyhemoglobin (HbO_2) and carboxyhemoglobin (HbCO). The percentage concentration of each component in the arterial and venous blood is shown in Table 1.

Table 1

Presence of different forms of hemoglobin *concentration* in arterial and venous blood

Form of hemoglobin	*Concentration* in arterial blood, %	Concentration in venous blood, %
Hb	3	25
HbO_2	92	70
HbCO	5	5

Thickness was determined according to the percentage concentration. Simulation was conducted for three wavelengths 605 nm, 700 nm and 850 nm. For each layer according to the sources which was used in simulation the following optical properties were selected: absorption coefficients μ_a scattering μ_s coefficients, anisotropy of scattering g, reflective index n [1, 2, 4, 5, 7].

Simulation of optical radiation passing through 23 layer biotissue was conducted for 10 million photons. The example of Monte-Carlo simulations results of absorption of optical radiation in different layers are shown in Table 2.

Table 2

The proportion of absorbed radiation for each of the layers at 605 nm, 700 nm and 850 nm wavelengths

Layer	The proportion of absorbed radiation for each of the layers		
	605nm	700nm	850nm
epidermis	$1{,}48\cdot10^{-2}$	$1{,}16\cdot10^{-2}$	$7{,}87\cdot10^{-3}$
dermis	$1{,}31\cdot10^{-2}$	$1{,}05\cdot10^{-2}$	$5{,}29\cdot10^{-2}$
HO_2	$4{,}92\cdot10^{-1}$	$2{,}06\cdot10^{-2}$	$3{,}91\cdot*10^{-1}$
Hb	$2{,}99\cdot10^{-2}$	$3{,}27\cdot10^{-2}$	$5{,}07\cdot10^{-3}$
HCO	$1{,}09\cdot10^{-2}$	$2{,}71\cdot10^{-3}$	$8{,}70\cdot10^{-4}$
dermis	$4{,}75\cdot10^{-3}$	$1{,}69\cdot10^{-2}$	$4{,}61\cdot10^{-2}$
HO_2	$1{,}69\cdot10^{-2}$	$3{,}14\cdot10^{-3}$	$3{,}79\cdot10^{-2}$
Hb	$5{,}70\cdot*10^{-3}$	$7{,}23\cdot10^{-2}$	$6{,}34\cdot10^{-3}$
HCO	$1{,}49\cdot10^{-4}$	$1{,}07\cdot10^{-3}$	$1{,}72*10^{-4}$
Subcutaneous tissue	$1{,}02\cdot10^{-4}$	$7{,}74\cdot10^{-3}$	$3{,}42\cdot10^{-3}$
muscle	$2{,}54\cdot10^{-4}$	$2{,}48\cdot10^{-2}$	$3{,}86\cdot10^{-3}$
bone	$2{,}50\cdot10^{-5}$	$8{,}01\cdot10^{-3}$	$3{,}67\cdot10^{-3}$
muscle	$2{,}88\cdot10^{-6}$	$5{,}29\cdot10^{-4}$	$9{,}22\cdot10^{-5}$
Subcutaneous tissue	$3{,}76\cdot10^{-7}$	$1{,}19\cdot10^{-4}$	$5{,}30\cdot*10^{-5}$
HCO	$1{,}16\cdot10^{-7}$	$6{,}03\cdot10^{-6}$	$6{,}05\cdot10^{-7}$
HO_2	$5{,}58\cdot10^{-7}$	$1{,}78\cdot10^{-5}$	$8{,}28\cdot10^{-5}$
Hb	$1{,}94\cdot10^{-7}$	$2{,}56\cdot10^{-4}$	$1{,}40\cdot10^{-5}$
dermis	$3{,}78\cdot10^{-9}$	$1{,}57\cdot10^{-5}$	$1{,}25\cdot10^{-5}$
HCO	$1{,}58\cdot10^{-9}$	$1{,}31\cdot10^{-6}$	$9{,}35\cdot10^{-8}$
HO_2	$7{,}84\cdot10^{-9}$	$4{,}03\cdot10^{-6}$	$1{,}11\cdot10^{-5}$
Hb	$7{,}33\cdot10^{-10}$	$9{,}69\cdot10^{-6}$	$1{,}44\cdot10^{-7}$
dermis	$1{,}60\cdot10^{-11}$	$1{,}46\cdot10^{-6}$	$4{,}19\cdot10^{-7}$
epidermis	$1{,}64\cdot10^{-11}$	$1{,}09\cdot10^{-6}$	$3{,}77\cdot10^{-8}$

Since the absorption of the second half of layers in biological model are insignificant, it is enough to take into account the following tissues: the skin, blood vessels, subcutaneous tissue, soft muscles and bone should be considered because it is characterized by a significant scattering of optical radiation.

Considering the fact that various forms of hemoglobin in the blood are mixed, the simulation was performed for different location sequences oxy-, carboxy-, deoxyhemoglobin. The result was calculated as the arithmetic mean of each of the sequences. The average values for oxyhemoglobin absorbed radiation with different forms of hemoglobin sequence shown in Fig. 3

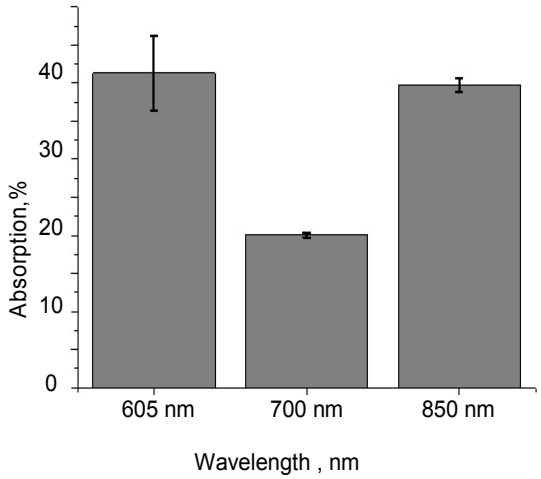

Fig. 2 The proportion of oxyhemoglobin absorbed radiation to sources with different wavelengths

The oxyhemoglobin absorption of optical radiation in biological multilayer structure at wavelengths of 605 nm and 805 two larger than for 700 nm. To compare the results of modeling and experimental *in vivo* [6], the ratio of oxy hemoglobin absorption during the Monte-Carlo simulation and ratio of falls saturation during experiment in vivo was calculated.

Table 3

Comparison of simulation results the absorption of optical radiation and the measured experimental values saturation changes under the influence of various sources of radiation

Pairs of wavelengths	The ratio of the absorption of radiation of different wavelengths during simulation	The ratio of saturation decline in experiments *in vivo* for the different sources of radiation
605/700 nm	2,07 ± 0,06	1,9 ± 0,2
850/700 nm	1,99 ± 0,01	2,1 ± 0,5
605/850 nm	1,04 ± 0,02	0,9 ± 0,3

Experimental and simulation results convergence shows that oxyhemoglobin photodissociation caused by absorption of photons of the exciting radiation, and the contribution of recombination is insignificantly for oxyhemoglobin concentration. Simulation of optical radiation absorption, together with the experiment in vivo provides an opportunity to investigate the effect of photodissociation in whole blood.

REFERENCES

1. *Bashkatov A. N.* Optical properties of skin, subcutaneous, and muscle tissues: a review / A. N. Bashkatov, E. A. Genina, V. V. Tuchin // J. of Innovative Optical Health Sciences, 2011 – Vol. 4 – № 1 – P. 9–38.

2. *Oxygen* Saturation-Dependent Absorption and Scattering of Blood / D. J. Faber, C. G. Maurice, E. G. Mik et al. // Phys. rev. lett., 2004 – Vol. 93. – P. 1–4.

3. *Gibson Q. H.* Photosensitivity of haem compounds. Nature / Q. H. Gibson, S. Ainsworth // Nature, 1957. – № 180. – P. 1416–1417.

4. *Jacques S. L.* Origins of tissue optical properties in UVA, visible and NIR regions // OSA TOPS on advances in optical imaging and photon migration, 1996. – Vol. 2. – P. 364–371.

5. *Kienle A.* In vivo determination of the optical properties of muscle with time-resolved reflectance using a layered model / A. Kienle, T. Glanzmann // Phys. Med. Biol., 1999. – Vol. 44. – P. 2689–2702.

6. *Mamilov S. A.* Photodissociation oxyhemoglobin and carboxyhemoglobin in arterial blood / S. A. Mamilov, S. S. Esman I. V. Hliebova // J. of Lviv University. Biology Series, 2014. – № 68. – P. 325–327.

7. *Rossi V. M.* Characterizing the optical properties of bone using a multi-fiber array and diffuse reflectance spectroscopy / V. M. Rossi, S. B. Gustafson, S. L. Jacques // Optics in bone biology and diagnostics, 2009.

8. *Tarasyev M. Yu.* Peculiarities of photochemical properties of hemoglobin in native conditions / M. Yu. Tarasyev, V. V. Ryl'kov, 1991. – Vol. 56, № 7. –P. 1296–1303.

9. *Wang L.* Monte-Carlo Modeling of Light Transport in Tissues / L. Wang, S. L. Jacques, L. Zheng // Computer methods and programs in biomedicine, 1995. – № 47. – P. 131–146.

Submitted on 16.10.16

С. Радченко, канд. фіз.-мат. наук,
С. Мамілов, канд. фіз.-мат. наук,*
І. Глєбова, студ.,
кафедра медичної радіофізики,
факультет радіофізики, електроніки та комп'ютерних систем,
Київський національний університет імені Тараса Шевченка, Київ,
***Інститут прикладних проблем фізики і біофізики НАН України, Київ**

МОДЕЛЮВАННЯ ВПЛИВУ ОПТИЧНОГО ВИПРОМІНЮВАННЯ НА ЗМЕНШЕННЯ ОКСИГЕМОГЛОБІНУ В КРОВІ

Із метою кращого розуміння результатів поглинання оптичного випромінювання в різних шарах багатошарових тканин було промодельовано поширення випромінювання методом Монте-Карло Значення оптичних параметрів, що використовувались для моделювання, були взяті з літератури. Представлено результати моделювання поглинання випромінювання різних джерел для кожного шару 23-шарової тканини. Проведено порівняльний аналіз експериментальних досліджень in vivo зміни насичення оксигемоглобіном крові під дією випромінювання і результатів моделювання поглинання світла оксигемоглобіном в крові

Ключові слова: метод Монте-Карло, оптика тканин, транспорт фотонів, фотодисоціація.

С. Радченко, канд. физ.-мат. наук,
С. Мамилов[1], канд. физ.-мат. наук,
И. Глебова, студ.,
кафедра медицинской радиофизи,
факультет радиофизики, электроники и компьютерных систем,
Киевский национальный университет имени Тараса Шевченко, Киев,
[1] Институт прикладных проблем физики и биофизики НАН Украины, Киев

МОДЕЛИРОВАНИЕ ВЛИЯНИЯ ОПТИЧЕСКОГО ИЗЛУЧЕНИЯ НА УМЕНЬШЕНИЕ ОКСИГЕМОГЛОБИНА В КРОВИ

Моделирование методом Монте-Карло распространения света в биоткани было применено с целью лучшего понимания результатов поглощения в различных слоях многослойных тканей. Значения оптических параметров, используемых в модели, были взяты из литературы. Представлены результаты моделирования поглощения излучения различных источников для каждого слоя 23-слойной ткани. Проведен сравнительный анализ экспериментальных исследований in vivo изменения насыщения оксигемоглобином крови под действием излучения и результатов моделирования поглощения света оксигемоглобином в крови

Ключевые слова: метод Монте-Карло, оптика тканей, транспорт фотонов, фотодиссоциация.

UDC 621.3.088.7

S. Reschikoff, post grad. stud.,
Radio engineering faculty,
Ulyanovsk State Technical University

TWO SIMPLE ALGORITHMS FOR AUTOMATION OF LF NOISE MEASUREMENTS

Flicker noise measurements are used for reliability evaluation of semiconductor devices. To evaluate trustworthiness of received information investigators must estimate the accuracy of noise measurement. Automation is necessary because of the laboriousness of the calculations and measurements. In this paper we will consider the some details of calculations to be automated. Some expressions for calculation are given.

Keywords: low-frequency noise, flicker noise, white noise, noise measurements, power spectral density, spectral exponent, corner frequency, measurement error, automation.

Introduction. Low-frequency (LF) noise (1/f noise, flicker noise, excess noise) of semiconductor devices is a subject of many modern scientific papers. It is founded in all types of semiconductor devices.

In the semiconductor electronics LF noise is used for reliability estimation of devices [24]. The level of the LF noise is one of the most important characteristics of devices used in microwave and optical systems [12]. It upconverts into phase noise that limits performance of oscillators and mixers [12].

Processes with such power-law spectrum are widespread in physics (traffic noise [15]), electronics (semiconductor devices, microelectromechanical systems, ceramic pressure sensors, photovoltaic cells etc), biology (neurons dynamics [4], mammograms), geophysics (atmospheric CO_2 records, geomagnetic storm), music, economics etc.

Generalized structure diagram of measurement setup for all these processes is shown on Fig. 1. Object under investigation (OUI) is exposed to impact of Generator. Generator may produce constant voltage, stable current or special noise. In particular case, it may be absent.

The OUI may be understood as semiconductor device, part of human body, acoustic field etc. In last cases it is necessary to have a Transducer before amplifier. When OUI is semiconductor device Transducer may be absent or represents a transimpedance amplifier. Amplifier (A) of course must be low-noise. Because spectral parameters of noise are most important Spectrum analyzer is necessary part of any noise measurement setup. There are different ways for building of this unit. It may be commercial FFT spectrum analyzer, selective nanovoltmeter, PC with ADC-board or other. PDU is processing and displaying unit.

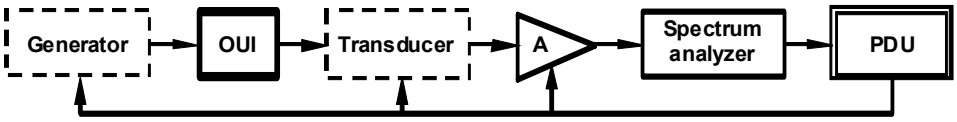

Fig.1. Generalized structure diagram of LF noise measurement system

Review of commercial measurement systems. Now there are 4 main commercial LF noise measurement systems. The first one is "E4727A Advanced Low-Frequency Noise Analyzer" (Keysight Technologies, Inc.). It is "High-performance noise analyzer designed to make fast, accurate and repeatable low-frequency noise measurements" [4]. Others are "9812D 1/f Noise Characterization System" (ProPlus Design Solutions, Inc.) [26], "3001B Flicker Noise Measurement System" (AdMOS GmbH) [28] and "1/f noise characterization solution – NC300A" (Platform Design Automation, Inc.) [14].

9812D System improves upon 9812B. 9812B was preceded by BTA9812A [13] (BTA Technology, Inc.). BTA Technology introduced BTA9812A system in 1999 [21].
There was also (till 2010) "EDGE Flicker Noise Measurement System" (Cascade Microtech, Inc.) [3]. Now (2016) "Cascade Microtech releases 1/f measurement solution with Keysight Technologies" [1]. There is also "Silvaco 1/f Noise Measurements Solution" (Silvaco, Inc.). It consists of S3245A noise amplifier and UTMOST III software [27].

But all these systems are very expensive and not always optimal for concrete problem. Therefore, scientists continue to design their own measurement systems. For example, such as in [9]. In [11] noise measurement setup contain modulation bridge that moving the input noise into higher frequencies, where LF noise level of preamplifiers is negligible. Besides this, setup includes 89410A spectrum analyzer (Agilent) and SR830 amplifiers (Stanford Research Systems). The system described in [25] consists of: HP4140B voltage source, SR570 Stanford Research amplifier, HP35665A signal analyser, PC.

It is necessary to underline that all these systems are based on discrete Fourier transform (DFT). But we will consider another case too.

Automation of analog filtration based measurement system. The following expressions may be used for spectral analysis by analog filtration such as in [10, 22–23]. A researcher has to deal with a mixture of white noise and LF noise with power spectral density (PSD):

$$G_{\text{nm}}(f) = \frac{A}{f^{\gamma}} + G_0, \qquad (1)$$

where A is some constant, f is the frequency, γ is the spectral exponent, G_0 is white noise level.

There is method of exponent evaluation by three points of spectrum [16]. For calculate exponent we must measure PSD on some frequencies [16, 19]:

$$\gamma_m = \log_k \frac{G_1 - G_{add}}{G_{add} - G_2}, \qquad (2)$$

where G_1, G_2 and G_{add} are PSDs of LF noise on first, second and additional points respectively; $k = \sqrt{f_2/f_1}$.

From these values of PSD can be estimated not only the γ value, but also the white noise level [20]:

$$G_{WNmsr} = \frac{G_{add}^2 - G_1 \cdot G_2}{2 \cdot G_{add} - G_1 - G_2}, \qquad (3)$$

where G_1, G_{add}, G_2 are corresponding PSDs.

White noise level is required for us to find the real PSD of LF noise on some frequency (for example on f_{add}). The full algorithm will be as on Fig. 2.

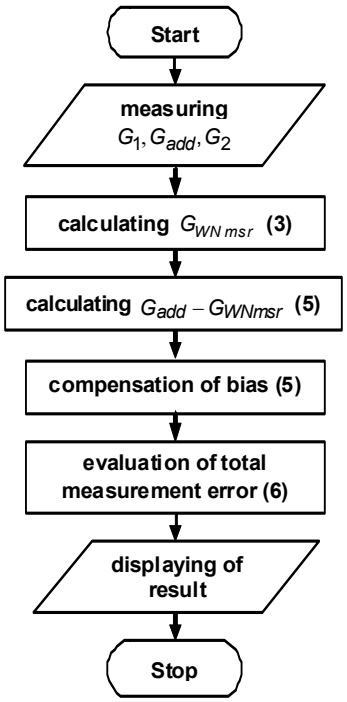

Fig. 2. Block diagram of measurement algorithm.

Expression for evaluated by (3) white noise level inaccuracy estimation is

$$\delta_{G\,WN} = \sqrt{\frac{a^2 + b^2 + c^2}{(G_1 + G_2 - 2\cdot G_{add})^2 \cdot (G_{add}{}^2 - G_1 \cdot G_2)^2}}, \quad (4)$$

$$a = (G_2 - G_{add})^2 \cdot G_1 \cdot \delta_{G1};$$

$$b = (G_1 - G_{add})^2 \cdot G_2 \cdot \delta_{G2};$$

$$c = 2\cdot (G_1 - G_{add})(G_2 - G_{add}) \cdot G_{add} \cdot \delta_{Gadd},$$

where δ_{G1}, δ_{Gadd}, δ_{G2} are corresponding relative mean squared random errors of G_1, G_{add}, G_2.

The real value of LF noise PSD (after systematic errors compensation) on some frequency will be

$$G_{LF\,Cps} = \frac{G_{NM} - G_{WNmsr}}{1 + \delta_{\text{bias}}}, \quad (5)$$

where δ_{bias} is a bias error, G_{NM} is a PSD of noise mixture, G_{WNmsr} is a measured PSD of white noise (3).

The square of total error of calculated LF noise PSD on some frequency real value will be

$$\delta_{G\,LF\,Cps}{}^2 = \left(\frac{\delta_{\text{bias}} \cdot \delta_{\delta\text{bias}}}{1 + \delta_{\text{bias}}}\right)^2 + \frac{(G_{NM} \cdot \delta_{G\,NM})^2 + (G_{WNmsr} \cdot \delta_{G\,WN})^2}{(G_{NM} - G_{WNmsr})^2}, \quad (6)$$

where δ_{bias} is a bias error, $\delta_{\delta\text{bias}}$ is a random mean squared error of δ_{bias} evaluation, G_{NM} is a PSD of noise mixture (G_{add}, for example), $\delta_{G\,NM}$ is a corresponding error, G_{WNmsr} is a measured PSD of white noise (3), $\delta_{G\,WN}$ is a corresponding error (4).

Expression for finding δ_γ, required for calculation of $\delta_{\delta\text{bias}}$, from experimental data is given in [16]:

$$\delta_\gamma = \frac{\sqrt{\left(\frac{G_1 \cdot \delta_{G1}}{G_1 - G_{add}}\right)^2 + d^2 + \left(\frac{G_2 \cdot \delta_{G2}}{G_2 - G_{add}}\right)^2}}{\ln\left(\frac{G_1 - G_{add}}{G_{add} - G_2}\right)}, \quad (7)$$

$$d = \left(\frac{G_{add} \cdot \delta_{Gadd}}{G_1 - G_\partial} \cdot \frac{G_2 - G_1}{G_2 - G_{add}}\right),$$

where δ_{G1}, δ_{Gadd}, δ_{G2} are corresponding relative mean squared random errors of G_1, G_{add}, G_2.

Expression for estimation of δ_γ in modeling purposes is given in [17, 19]. On Fig. 3 two graphics of $\delta_{G\,LF\,Cps}$ (6) are shown (with $\gamma = 3$, LF noise corner frequency – 1 kHz, duration of averaging is 1 s).

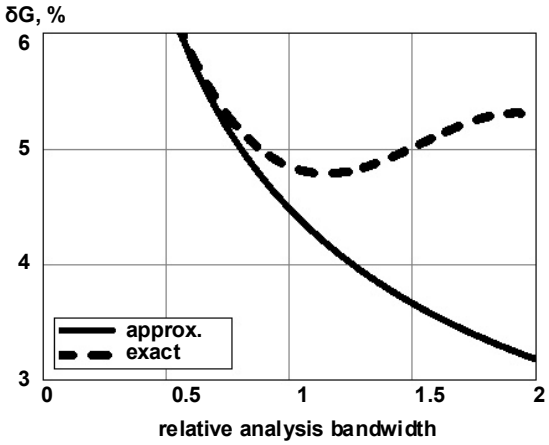

Fig. 3. Dependence of total relative error on bandwidth

For graphic "approximated" formula of bias error (δ_{bias}) obtained by expanding in a Taylor series [18] is used. For graphic "exact" more accurate calculation of δ_{bias} is used. But for graphic "exact" only a bandwidth of G_{NM} is variable (others bandwidths equal to 0.5). So, the total error with the expansion of bandwidth only is reducing. The optimum bandwidth is not observed. Automation in this case is necessary at least for convenient systematic errors compensation.

Automation of DFT-based measurement system. The most of noise measurement systems are DFT-based [2, 6-8]. In this case after DFT of noise time series we obtain a number of PSD values with random error [23]:

$$\delta_G \approx 1/\sqrt{T \cdot \Delta f_{eff}} \approx 1 \quad (8)$$

Strictly speaking, expression (8) in case $\Delta f_{eff} \approx T$ is not applicable. LF noise power spectral density diagram without any averaging in non-logarithmic scale is shown on Fig. 4.

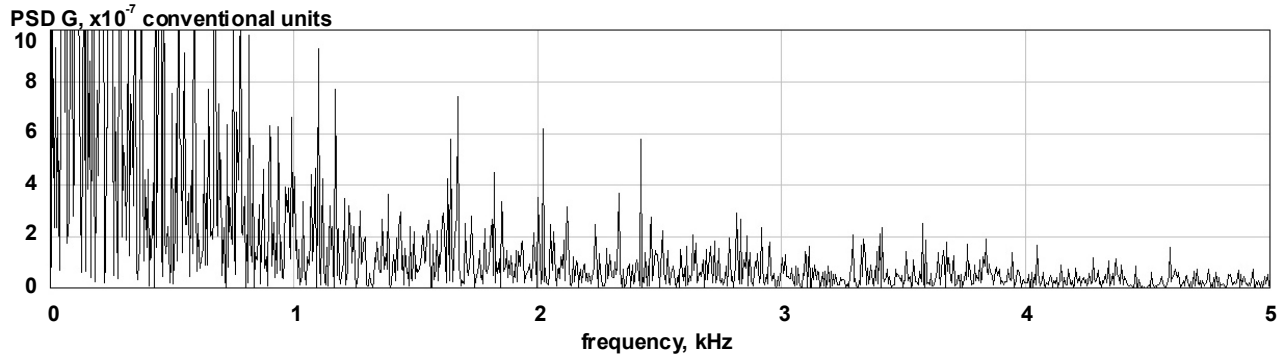

Fig. 4. LF noise PSD without any averaging

It is obviously that an averaging is necessary. The general structure of proposed averaging algorithm is shown on Fig. 5.

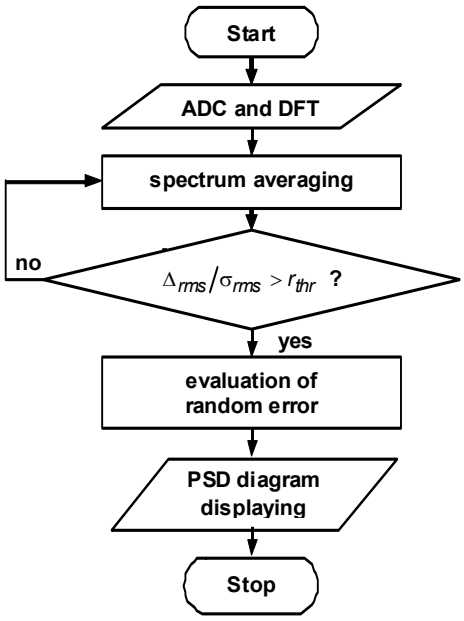

Fig.5. Block diagram of PSD averaging algorithm.

On Fig. 5 Δ_{rms} is the experimental random mean squared (RMS) relative difference between neighboring spectral components (9), a σ_{rms} is the theoretical RMS relative random error for calculating difference between neighboring spectral components (10) and r_{thr} is the threshold coefficient that is set by researcher.

The expression for Δ_{rms} is

$$\Delta_{rms} = \sqrt{\frac{1}{N}\sum_{m=1}^{N-1}\left(\frac{2\cdot|G_m - G_{m+1}|}{G_m + G_{m+1}}\right)^2}\ , \qquad (9)$$

where N is a number of components in spectrum, G_m is the m-th value of noise PSD.

The expression for σ_{rms} is

$$\sigma_{rms} = \sqrt{\delta_m^2 + \delta_{m+1}^2}\ , \quad 0 < m < N\ ,$$

where m is an integer, δ_m is a RMS relative random error of m-th spectral component value.

If $\delta_m = \delta_{m+1}$ then

$$\sigma_{rms} = \sqrt{2/n_{avr}}\ , \qquad (10)$$

where n_{avr} is a number of combined basic spectral components.

If a value of spectral step is indifferent then value of n_{avr} can be increased by one per algorithm step. If one want to see 10^n-like frequency graduations then

$$n_{avr} = 10^s\ ,$$

where s is the number of averaging step.

LF noise PSD diagram for blue light-emission diode (LED) is shown on Fig. 6 in log-log scale. LED forward current was 10 mA. LF noise PSD after averaging by proposed algorithm is shown by white curve (random error – 4 %). LF noise PSD after minimal averaging (random error – 41 %) is shown as background by black curve.

Conclusion. The first algorithm described in this paper allows to compensate systematic errors of PSD value estimate. But it is applicable only if model (1) is adequate to measured noise PSD. In more complex cases DFT spectral analyze is needed. The result of DFT requires an averaging. The second algorithm allows to determine the optimal level of averaging.

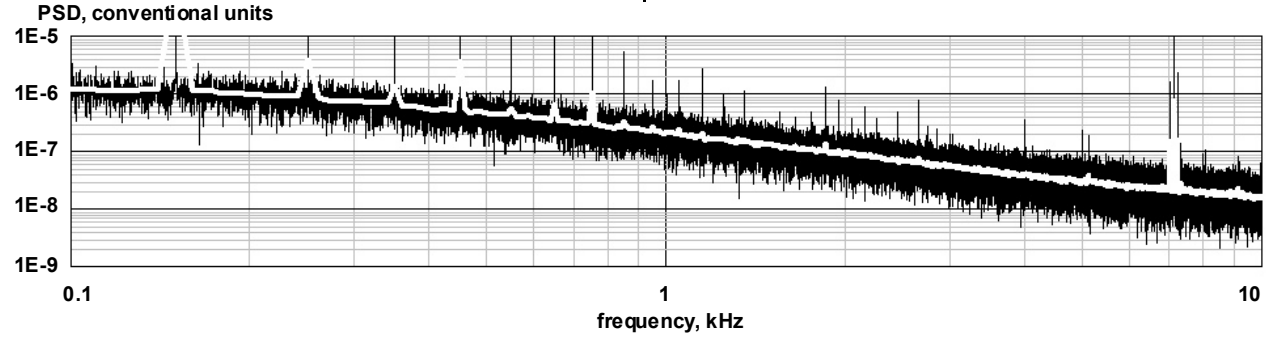

Fig. 6. LF noise PSD with averaging

REFERENCES

1. *Cascade* Microtech Releases 1/f Measurement Solution With Keysight Technologies : [electronic resource]. – URL: https://www.cascademicrotech.com/news/cascade-microtech-releases-1/f-measurement-solution-with-keysight-technologies].

2. *Dedicated* instrumentation for high sensitive, low frequency noise measurement systems / C. Ciofi, G. Giusi, G. Scandurra, B. Neri // Fluctuation and Noise Lett., 2004. – Vol. 4, № 2. – P. 385–402.

3. EDGE Flicker Noise Measurement System States : [electronic resource]. – URL: http://www.mbelectronique.fr/Edge_Brochure.pdf.

4. E4727A Advanced Low-Frequency Noise Analyzer States : [electronic resource]. – URL: http://www.keysight.com/ru/pd-2389560-pn-E4727A /advanced-low-frequency-noise-analyzer.

5. *Fractal* analysis reveals subclasses of neurons and suggests an explanation of their spontaneous activity / Luis H. Favela, Charles A. Coey, Edwin R. Griff, Michael J. Richardson // Neuroscience Lett., 2016. – Vol. 626, № 4. – P. 54–58.

6. *Applications* of integrated solar cells in low noise instrumentation / G. Scandurra, G. Cannata, G. Giusi, C. Ciofi // Noise and Fluctuations (ICNF), 2013, 22nd Internat. Conf. – P. 1–4.

7. *Automatic* measurement system for the DC and low-f noise characterization of FETs at wafer level / G. Giusi, O. Giordano, G. Scandurra et alю // IEEE Internat. Instrumentation and Measurement Technology Conf. (I2MTC) 2015, 11–14 May 2015. – P. 2095–2100.

8. *Giusi G.* Estimation errors in $1/f^{\gamma}$ noise spectra when employing DFT spectrum analyzers / G. Giusi, G. Scandurra, C. Ciofi // Fluctuation and Noise Lett.., 2013. – Vol. 12, № 1.

9. *High* sensitivity measurement system for the direct-current, capacitance-voltage, and gate-drain low frequency noise characterization of field effect transistors / G. Giusi, O. Giordano, G. Scandurra et al. // Rev. Sci. Instrum., 2016. – Vol. 87, № 4. – 044702. – P. 1–6.

10. *Gorlov M. I.* Measurement of the noise parameters of semiconductor devices / M.I. Gorlov, D.Yu. Smirnov, D.L. Anufriev // Measurement Techniques. – 2006. – V.49, № 12. – P. 1241-1245.

11. *Julin J.* Fabrication, electrical characterization and 1/f noise study of submicron-sized superconducting tunnel junctions : Acad. Dissertation … Ph. D./ J. Julinю – Finland, 2016.

12. *Levinshtein M.* Tunneling effects and low frequency noise of GaN/GaAlN HFETs / M. Levinshtein S. Rumyantsev and M. S. Shur // Advanced Experimental Methods for Noise Research in Nanoscale Electronic Devices, 2004. – P. 161–168.

13. *Mercha A.* Inversion Layer Quantization Impact on the Interpretation of 1/f Noise in Deep Submicron CMOS Transistors / A. Mercha, E. Simoen, G. Richardson, C. Claeys // Proc. of the 32nd European Solid-State Device Research Conf., 24–26 Sept., 2002. – P. 79 82.

14. Noise Solution – NC300 : [electronic resource]. – URL: http://www.platform-da.com/a/en/NC300.

15. *Traffic* Noise: 1/f Characteristics / K. B. Patange, A. R. Khan, S. H. Behere and Y. H. Shaikh // Internat. J. of Artificial Life Res., 2011. – Vol. 2, № 4. – P. 1–11.

16. *Reschikoff S. E.* Otsenka pogreshnosti opredeleniya pokazatelya spektra NCh-shuma / S. E. Reschikoff // 19-i Mezhdunarodnyi molodezhnyi forum "Radioelektronika i molodezh' v XXI veke", Kharkiv, 20–22 April, 2015. – Vol. 2. – P. 164–165 (in rus.).

17. *Reschikoff S. E.* Some practical aspects of construction of adaptive system for low-frequency noise measurement of semiconductor devices / S. E. Reschikoff // XV Internat. Young Sci. Conf. on App. Phys., June 10–13, 2015. – Kyiv, Ukraine. – P. 92–93.

18. *Reschikoff S.* On reliability of optimum analysis bandwidth formula for flicker noise / S. Reschikoff // 1st Internat. School and Conf. on Optoelectronics, Photonics, Engineering and Nanostructures, St. Petersburg, Russia, March 25–27, 2014. – P. 105–106.

19. *Reschikoff S.* Basic relations for construction of adaptive system for low-frequency noise measurement of semiconductor devices / S. Reschikoff // Bulletin of Nat. Taras Shevchenko Univ. of Kyiv. Series: Radio Physics and Electronics, 2015. – Vol. 1, № 23. – P. 71–73.

20. *Reschikoff S. E.* About algorithms for automated measurement of LF noise in semiconductor devices : abstracts / S. E. Reschikoff // XVI Internat. Young Sci. Conf. on App. Phys., 2016, June 15–18. – Kyiv, Ukraine . – P. 109–110.

21. *RF* and M-S Simulation Get a Boost with New Noise Characterization System from BTA Technology States : [electronic resource]. – URL: http://www.eetimes.com/document.asp?doc_id=1213720.

22. *Sergeev V. A.* The Systematic Error of Measurement of the Exponent of the Frequency Dependence of the Spectrum of Low-Frequency Noise / V. A. Sergeev, S. E. Rezchikov // Measurement Techniques, 2016. – Vol. 58, № 10. – P. 1160–1166.

23. *Sergeev V. A.* The systematic errors of the measurement of the parameters of low-frequency noise with a $1/f^{\gamma}$ spectrum / V. A. Sergeev, O. A. Dulov // Measurement Techniques, 2008. – Vol. 51, № 10. – P. 1122–1127.

24. *Vandamme L. K. J.* Noise as a diagnostic tool for quality and reliability of electronic devices / L. K. J. Vandamme // IEEE Trans. Electron Devices, 1994. – Vol. 41, № 11. – P. 2176–2187.

25. *Westerhout R. J.* A Study of Passivation, Dark Current and 1/f Noise in Mid-wave Infrared HgCdTe Photovoltaic Detectors : Thesis … Ph. D. / R. J. Westerhout. – Australia, 2013.

26. *1/f* Noise Characterization System – 9812D States : [electronic resource]. – URL: http://www.proplussolutions.com/9812d-en.php.

27. *1/f* Noise Measurements and SPICE Model Extraction For MOS Transistors States : [electronic resource]. – URL: http://www.silvaco.com/products/analog/vyper/noiseamp/noiseamp_mos /MOS_noisebox_03.pdf.

28. *3001B* Flicker Noise Measurement System States : [electronic resource]. – URL: http://www.admos.de/en/services/product-overview /flicker-noise-system.

Submitted on 23.11.16

С. Резчиков, асп.,
радіотехнічний факультет,
Ульяновський державний технічний університет, Ульяновськ

ДВА ПРОСТИХ АЛГОРИТМИ АВТОМАТИЗАЦІЇ ВИМІРЮВАНЬ НЧ-ШУМУ

Вимірювання флікер-шуму застосовні для оцінки надійності напівпровідникових приладів. Для оцінки достовірності отриманої інформації дослідники повинні оцінити точність вимірювання шуму. Автоматизація необхідна через трудомісткість розрахунків і вимірювань. Розглянуто деякі деталі обчислень, придатних для автоматизації. Надано деякі вирази для розрахунку.

Ключові слова: низькочастотний шум, флікер-шум, білий шум, шумові вимірювання, спектральна щільність потужності, показник спектра, частота перегину, похибка вимірювання, автоматизація.

С. Резчиков, асп.,
радиотехнический факультет,
Ульяновский государственный технический университет, Ульяновск

ДВА ПРОСТЫХ АЛГОРИТМА АВТОМАТИЗАЦИИ ИЗМЕРЕНИЙ НЧ-ШУМА

Измерения фликкер-шума применимы для оценки надежности полупроводниковых приборов. Для оценки достоверности полученной информации исследователи должны оценить точность измерения шума. Автоматизация необходима из-за трудоемкости расчетов и измерений. Рассмотрены некоторые детали вычислений, подходящих для автоматизации. Даны некоторые выражения для расчета.

Ключевые слова: низкочастотный шум, фликкер-шум, белый шум, шумовые измерения, спектральная плотность мощности, показатель спектра, частота перегиба, погрешность измерения, автоматизация.

UDC 535.341.08, 535.342, 53.096A

A. Sizhuk, Ph. D.
Department of Electrophysics,
Faculty of Radiophysics, Electronics and Computer Systems,
Taras Shevchenko National University of Kyiv, Kyiv

ABSORPTION PROPERTIES OF ATOMS WITH THE QUANTUM OPTICAL INTERACTION

The theory of two-laser beam technique for the investigation of stimulated emission and absorption near resonance is present. The method for the calculation of the probe field absorption coefficient is described. Using the analytical expressions for the macroscopic absorption coefficient, previously derived in the kinetic limit for the system interacting with a coherent pump and weak counter-propagating probe fields tuned near sodium D_2 line, the behavior of maximum probe absorption is predicted for the range of temperatures of sodium vapor from 600 to about 800 K.

Keywords: absorption coefficient, kinetic equation, optics, atomic vapour, quantum optical, interatomic interaction.

Introduction. The application of the theory, developed in paper [12], is demonstrated for sodium vapor with densities from 0 to about 7000 atoms per cubic resonant D_2 wavelength (or from 0 to 35×10^{21} atoms per cubic meter corresponding to the maximum vapor temperature about 800 K and pressure 1650 Pa) in the optical region. The description of the system is formulated in the terms of long-range interatomic interaction induced by the quantum optical mechanism of exchange by photons between atoms. The quantum optical basis of the theory is established in the model Hamiltonian derived in [13].

The line shape of transmitted through the sample probe beam was first experimentally obtained in the work [4]. In the experiment the sample of sodium was heated to about 600 K (see the scheme of the experimental setup in figure 1). The frequencies of the driving and counter propagating probe laser beams are tuned near the atomic resonance corresponding to sodium D_2 line. The nonlinear increase in the intensity of the probe beam was observed at the so-called threshold density around 130 atoms per cubic wavelength.

In this work we predict the nonlinear decrease in the intensity of probe beam for the saturation region from 6600 to 6700 atoms in cubic wavelength. The feature is induced by collective long-range coupling between the population inversion and polarization of the medium.

The examples of researches devoted for the dynamical description of two and more particles, taking into account quantization of electromagnetic field, can be found, for example, in such works as [2, 3] and [6, 7]. Many quantum optical effects, for example, such as superradiance [9], subradiance [8], and photon entanglement [10] etc. are known today. In fact, the mentioned quantum field effects require well defined localization of atoms, otherwise the necessary coherence between atomic and field states does not form. The coherence in atomic states determines the certain collective effects in the system of atoms and field (see [1]). Hence, any averaging over statistical ensemble is expected to ruin possible quantum field effects. Even in the case of one-atomic approximation in the explanation of the recoil induced resonances or collective atomic recoil mechanism (see analysis in [1]), a definite coherence is required. For example, the coupled by the conservation law translational momentum of an atom and the absorbed or re-emitted momentum of a photon make different contribution to the scattering process, depending on a local atomic density and velocity. However, in a certain sense, the collective coherence is possible not only between atomic states but also between the atomic and quantum field states in forming the polarization and population gratings even at relatively high temperatures and atomic densities. In comparison with the mentioned theories (see [1]), the long-range interaction, due to quantization of electromagnetic field, is emphasized in our calculations as a main contributor to the certain non-linear effects. The observed experimental time scale in [4] for the build-up of the probe field amplification was of the order of the spontaneous emission time. In the case of quite high sample temperatures, the thermal atomic motion during the time scale can be comparable with the movement on the wavelength distance. These allow to neglect multiple spontaneous recoils and quantum recoil effects (see more theoretical details in [5]) in the present calculation. Furthermore, at the atomic densities, corresponding to the temperature domain of sodium vapor from 600 K to 800 K, the "hard core" collision rate for a sodium atom is of the order of 10^6 collisions per second. The complicated interatomic collision mechanism is therefore interpolated by the decay rate of an atomic exited state.

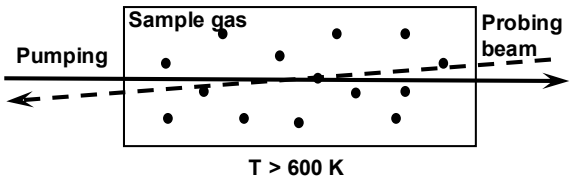

Fig. 1. Illustration of the two-laser beam propagation through the "hot" atomic vapor used in the setup [4]

Theory. Let the driven system of interacting two-level atoms is modeled by the Schrödinger equation (see [13]):

$$\frac{\partial}{\partial t}\left|\Psi\right\rangle = -\frac{i}{\hbar}\left(\hat{\mathrm{H}} + \hat{\Gamma}\right)\left|\Psi\right\rangle, \tag{1}$$

$$\begin{aligned}\hat{\mathrm{H}} &= \hbar\omega_a \sum_{i=1}^{N} \sigma_i^{+}\sigma_i + \hbar\omega_b \sum_{i=1}^{N} \sigma_i \sigma_i^{+} \\ &- \sum_{i=1}^{N} \hat{\vec{d}}_i \cdot \vec{\mathrm{E}}\left(t, \vec{r}_i\right) + \frac{1}{2}\frac{1}{4\pi\varepsilon_0} \sum_{i,j;i\neq j}^{N,N} Q_{ij},\end{aligned} \tag{2}$$

$$Q_{ij} = \frac{1}{\left|\vec{r}_i - \vec{r}_j\right|^3}\left\{\hat{\vec{d}}_i \cdot \hat{\vec{d}}_j - 3\left(\hat{r}_{ij} \cdot \hat{\vec{d}}_i\right)\left(\hat{r}_{ij} \cdot \hat{\vec{d}}_j\right)\right\} \tag{3}$$

with the dipole operator is defined as $\hat{\vec{d}}_i = \vec{\mu}_{ab}^{\,i}\sigma_i^{\dagger} + \vec{\mu}_{ba}^{\,i}\sigma_i$, where σ_i, σ_i^{+} are the excited state creation and nnihilation operators for the i-th atom, accordingly (I = 1,..., N). N is the total number of atoms; a denotes the excited state and b the ground state of an atom; r_i is the position of the i-th atom; $\hat{r}_{ij}$ is the unit vector pointing from atom j to atom i. The off-diagonal dipole matrix elements are defined by terms $\vec{\mu}_{ab}^{\,i}$.

Operator $\hat{\Gamma}$ describes the decay (relaxation rate) of the excited state of a single atom.

The corresponding macroscopic evolutional equations, derived in [12] assuming the vanishing space correlations between atoms with time, have the following form:

$$\frac{\partial}{\partial t}\Delta\left(t,\vec{r}\right)=\gamma\left(\bar{n}\frac{n\left(\vec{r}\right)}{N}-\Delta\left(t,\vec{r}\right)\right)+i\left(\rho_{ba}\left(t,\vec{r}\right)\Omega\left(t,\vec{r}\right)-c.c.\right), \quad (4)$$

$$\frac{\partial}{\partial t}\rho_{ba}\left(t,\vec{r}\right)=\left(-\gamma_{ba}+i\bar{\omega}_0\right)\rho_{ba}\left(t,\vec{r}\right)+i\Delta\Omega^{*}\left(t,\vec{r}\right), \quad (5)$$

where Δ is the atomic population inversion, while ρ_{ba} is the coherence between the *a* and *b* states; $\bar{n}$ is the initial non-averaged inversion when an external electric field is not applied; $n\left(\vec{r}\right)$ is the number of atoms per unit volume; $\bar{\omega}_0$ is the averaged frequency of the resonant transition. And,

$$\Omega\left(t,\vec{r}\right)=\Omega^{AF}\left(t,\vec{r}\right)+\Omega^{Int}\left(t,\vec{r}\right) \quad (6)$$

with

$$\Omega^{AF}\left(t,\vec{r}\right)=\frac{\mu\hat{\mu}\cdot\vec{E}\left(t,\vec{r}\right)}{\hbar}, \quad (7)$$

$$\Omega^{Int}\left(t,\vec{r}\right)=-\frac{2}{\hbar}\chi\int d\vec{r}'\left\{\mathrm{Re}\left(\rho_{ba}\left(t,\vec{r}'\right)\right)Q\left(\vec{r},\vec{r}'\right)\right\}, \quad (8)$$

where the integral kernel is corresponding to the quantum optics of long-range dipole-dipole coupling (originating from the results in [13]), such as

$$Q\left(\vec{r},\vec{r}'\right)=\frac{\hat{\mu}\cdot\hat{\mu}'}{\left|\vec{r}-\vec{r}'\right|^3}-3\frac{\left(\hat{\mu}\cdot\left(\vec{r}-\vec{r}'\right)\right)\left(\hat{\mu}'\cdot\left(\vec{r}-\vec{r}'\right)\right)}{\left|\vec{r}-\vec{r}'\right|^5} \quad (9)$$

$$\text{with}\ \chi\cong\frac{1}{4\pi\varepsilon_0}N\mu^2.$$

The electromagnetic field satisfies the Maxwell equation

$$\nabla\times\nabla\times\vec{E}\left(t,\vec{r}\right)+\frac{1}{c^2}\frac{\partial^2}{\partial t^2}\vec{E}\left(t,\vec{r}\right)=-\mu_0\frac{\partial^2}{\partial t^2}\vec{P}\left(t,\vec{r}\right), \quad (10)$$

where the polarization $\vec{P}\left(t,\vec{r}\right)$ of the system per unit volume is given by

$$\vec{P}\left(t,\vec{r}\right)=N\mu\hat{\mu}\left(\rho_{ba}\left(t,\vec{r}\right)+\rho_{ab}\left(t,\vec{r}\right)\right). \quad (11)$$

For the strongly pumped medium we assumed a linear polarization of pumping field and therefore set the off-diagonal dipole matrix elements for all atoms being under the action of pump field to be equal in magnitude $\vec{\mu}_{ab}^{\,i}=\left(\vec{\mu}_{ab}^{\,i}\right)^{*}=\mu\cdot\hat{\mu}$ with i = 1, …, N, where $\hat{\mu}$ is the unit vector (parallel to the polarization of the external pumping field). Let

$$\vec{E}=\vec{E}_0e^{-i\left(\omega t-\vec{k}\cdot\vec{r}\right)}+\vec{E}_0'e^{-i\left(vt-\vec{k}'\cdot\vec{r}\right)}. \quad (12)$$

The applied weakness of the probe field and interatomic coupling in comparison with the driving field, that can be expressed as

$$\frac{\left|\Omega'\right|}{\left|\Omega^{AF}\right|}<<1\ \text{and}\ \frac{\left|\Omega^{Int}\right|}{\left|\Omega^{AF}\right|}<<1\ \text{with}\ \Omega'=\frac{\mu\hat{\mu}\cdot\vec{E}_0'}{\hbar}, \quad (13)$$

allows to represent the solution of the kinetic equations (4) and (5) through the following terms:

$$\Delta\left(t,\vec{r}\right)=\Delta^{(0)}+\delta\Delta^{(2)}\left(t,\vec{r}\right)+\delta\breve{\Delta}\left(t,\vec{r}\right)+\delta\tilde{\Delta}\left(t,\vec{r}\right)+\delta\Delta\left(t,\vec{r}\right), \quad (14)$$

and

$$\rho_{ba}\left(t,\vec{r}\right)=\rho_{ba}^{(0)}+\delta\rho_{ba}^{(2)}\left(t,\vec{r}\right)+\delta\breve{\rho}_{ba}\left(t,\vec{r}\right)+\delta\tilde{\rho}_{ba}\left(t,\vec{r}\right)+\delta\rho_{ba}\left(t,\vec{r}\right) \quad (15)$$

where, $\Delta^{(0)}$ and $\rho_{ba}^{(0)}$ form the "equilibrium" solution for the system of pumped non-interacting atoms. $\delta\Delta\left(t,\vec{r}\right)$ and $\delta\rho_{ba}\left(t,\vec{r}\right)$ are the perturbation to $\Delta^{(0)}$ and $\rho_{ba}^{(0)}$, respectively, in the case of non-zero interaction item $\Omega^{Int}\left(t,\vec{r}\right)\neq0$ and unapplied external probe field $\Omega'=0$. The corrections $\delta\tilde{\Delta}\left(t,\vec{r}\right)$ and $\delta\tilde{\rho}_{ba}\left(t,\vec{r}\right)$ are induced when both, the strong and weak fields, are applied with disregarded interatomic interaction $\Omega^{Int}\left(t,\vec{r}\right)=0$. $\delta\breve{\Delta}\left(t,\vec{r}\right)$ and $\delta\breve{\rho}_{ba}\left(t,\vec{r}\right)$ take into account the corrections to the absorption/reemission rates induced by the perturbed population inversion and polarization $\delta\Delta\left(t,\vec{r}\right)$ and $\delta\rho_{ba}\left(t,\vec{r}\right)$, therefore here $\Omega^{Int}\left(t,\vec{r}\right)\neq0$ and $\Omega'\neq0$. $\delta\Delta^{(2)}\left(t,\vec{r}\right)$ and $\delta\rho_{ba}^{(2)}\left(t,\vec{r}\right)$ represent the strongly non-linear perturbation of the interaction item $\Omega^{Int}\left(t,\vec{r}\right)$, thus induced by the dipole-dipole coupling of the perturbed population and polarization of the medium.

The corresponding definitions of the introduced perturbation items with the help of differential equations are provided in [12]. When the steady state approximation is applied for the pumping field ($\Delta^{(0)}$ and $\rho_{ba}^{(0)}$ are assumed to be essentially larger in their absolute values in comparison with the other items in (14) and (15)), the appearing in the introduced kinetic equations (4) and (5) integral Rabi frequency $\Omega^{Int}\left(t,\vec{r}\right)$ can be factorized to time and space functions. Namely,

$$\Omega^{Int}\left(t,\vec{r}\right)\propto I\left(\vec{k},\vec{r}\right), \quad (16)$$

where

$$I\left(\vec{k},\vec{r}\right)=\int_{\bar{V}}d\vec{r}'e^{i\vec{k}\cdot\left(\vec{r}-\vec{r}'\right)}Q\left(\vec{r},\vec{r}'\right). \quad (17)$$

Here the integration is defined over the space volume $\bar{V}$ outside the spherical shell with the radius equal to the average distance between nearest atoms $\bar{l}_0=\frac{1}{n^{1/3}}$.

The absorption coefficient is proportional to the sum of the absorption rates defined by the solution (14) and (15). In building the transmittance curve defined by (14) and (15), the time dependence of the amplitude of probe field in the case of the near stationary system state is neglect. This approximation (see more detailed description for the approximation, for example, in [11]) allows us to use the exponential dependence of the probe transmission on the distance passed by the probe beam (along the *Z*-axis). Because the experimental saturation gain (transmission) of about 2–2,5 is valid for quite long paths, a relatively weak dependence of the total probe absorption coefficient on the probe and pump amplitudes can be used for further simplification. Therefore, the following exponential dependence of the probe intensity on the beam path length is in use

$$\frac{I_{out}'}{I_{in}'}=\exp\left(-\alpha_{tot}'z\right), \quad (18)$$

where the total probe absorption coefficient α'_{tot} is defined as the superposition of the coefficients "induced" by the perturbations, introduced in (14) and (15),

$$\alpha'_{tot} = \delta\alpha' + \delta\bar{\alpha}' + \delta\alpha'^{(2)}. \qquad (19)$$

The following parameters are used in obtaining the numerical results here and in the following example. The fraction of atoms having their absorption frequencies (due to the Doppler effect), equal to frequencies $\bar{\omega}_0 \pm 25\times10^6$ Hz, is estimated to be 0,0124 at 617 K. Atomic mass is m_{Na} = 0,3817668548x10^{25} kg; $\bar{\omega}_0 = \pi\times0{,}1017979636\times10^{16}$ Hz. The volume of the sample cell is $\pi\times8{,}3\times10^{-8}$ m^3. Also, $\mu = 1{,}725\times10^{29}$ Cm for D_2 linearly polarized laser beam. Pump Rabi frequency $\left|\Omega^{AF}\right|$ is set 2,5 GHz. The initial intensities of pump and probe laser beams are set equal to I_{in} = 8x10^6 W/m^2 and I'_{in} = 15x10^4 W/m^2, respectively; $\gamma = 2\gamma_{ba} = 61.543\times10^6$ Hz.

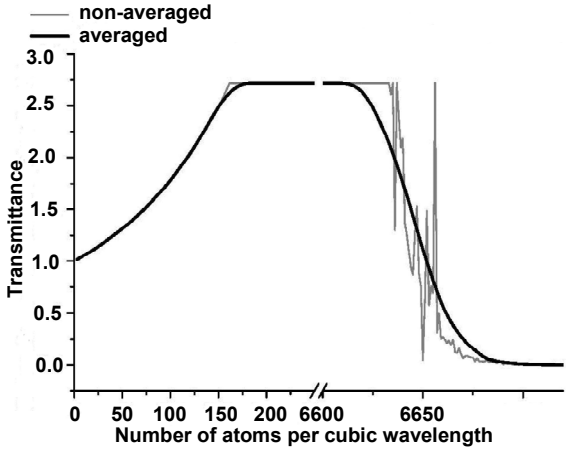

Fig. 2. The "maximum" probe amplification as a function of atomic number per cubic wavelength at non-resonant pump frequency. The thin line follows the density dependence of transmittance with resolution 1 atom per wavelength; the bold solid line shows the transmittance as the averaged thin curve with resolution about 23 atoms per wavelength. Pump is shifted on 700M Hz relative to the averaged resonant frequency. Effective beam path-length is 1/300 meters.

The graph in picture Fig. 2 shows the transmittance of probe beam in the vicinity of the maximum gain depending on the number of atoms per cubic wavelength, *n*, for non-resonant pumping. Note, the relative pump detuning, determining a maximum gain, is fixed at the same value as for the vapor density defined by temperature 617 K. In the figure the pump frequency is displaced on 700 MHz relative to $\bar{\omega}_0$. As it can be seen, for the region of atomic densities from 180 to 6625 atoms per cubic wavelength, the system peak gain is in the saturation domain. Then, the curve starts falling down after reaching the threshold value of the atomic density at 6625 (or roughly saying, at 6630) atoms per cubic wavelength.

For higher atomic densities than 6675 atoms per cubic wavelength with detuned probe beam at the peak gain in the saturation region, the system becomes non-transparent for a probe signal. This can be explained by the shift of the maximum gain points closer to the resonant frequency, as it can be deduced from the analysis of the solutions (14) and (15). Note, the same point of the relative probe frequency, as for the maximum gain defined by the specific detuning for the region of relatively low atomic densities, is chosen in the region of the relatively high densities. The nature of the behavior can be explained in the context of the dependence of the corresponding absorption rate, that is defined by the expression for the rate $W^{(2)}$ in [12], on the interaction integral, *I,* in (17).

Conclusions. Thus, the application of the previously developed theory for testing the fundamental concept of quantization for electromagnetic field through the research of collective absorption/reemission effects in a strongly pumped vapor of interacting atoms is provided. The near resonant optical spectral line shape of pumped sodium vapor at relatively high temperatures is analyzed in the terms of collective effects, induced by the atom-field and long-range interatomic interaction, using the additivity of the corresponding absorption/reemission rates. The numerical result in the form of graph, built by adding the constituents of the total absorption coefficient, corresponds to the contributions from different effects (perturbations). This allows to describe the spectral line shape in the related terms of induced by interatomic interaction population inversion and polarization of the medium.

REFERENCES

1. *Berman P. R.* Comparison of recoil-induced resonances and the collective atomic recoil laser / P. R. Berman // Phys. Rev. A, 1999. – Vol. 59. – P. 585.

2. *Dicke R. H.* Coherence in spontaneous radiation processes / R. H. Dicke // Phys. Rev., 1954. – Vol. 93. – P. 99.

3. *Grinberg H. J.* Nonclassical Effects of a Two-Level Spin System Interacting with a Two-Mode Cavity Field via Two-Photon Transition / H. J. Grinberg // Phys. Chem. B, 2008. – Vol. 112(50). – P. 16140.

4. *Self-Organization*, Broken Symmetry, and Lasing in an Atomic Vapor: The Interdependence of Gratings and Gain / P. R. Hemmer, N. P. Bigelow, D. P. Katz et al. // Phys. Rev. Lett., 1996. – Vol. 77. – P. 1468.

5. *Quantum* recoil effects in finite-time disentanglement of two distinguishable atoms / F. Lastra, S. Wallentowitz, M. Orszag and M. Hernandez // J. of Phys. B: Atomic, Molecular and Optical Phys., 2009. – Vol. 42. – P. 065504.

6. *Lehmberg R. H.* Radiation from an *N*-Atom System. I. General Formalism / R. H. Lehmberg // Phys. Rev. A, 1970. – Vol. 2. – P. 883.

7. *Stephen M. J.* First‐Order Dispersion Forces / M. J. Stephen // J. Chem. Phys., 1964. – Vol. 40. – P. 669.

8. *Experimental* Evidence for Subradiance / D. Pavolini, A. Crubellier, P. Pillet et al. // Phys. Rev. Lett., 1985. – Vol. 54. – P. 1917.

9. *Rehler N. E.* Superradiance / N. E. Rehler and J. H. Eberly // Phys. Rev. A, 1971. – Vol. 3. – P. 1735.

10. *Directed* Spontaneous Emission from an Extended Ensemble of N Atoms: Timing Is Everything / M. O. Scully, E. S. Fry, C. H. R. Ooi and K. Wodkievic // Phys. Rev. Lett., 2006. – Vol. 96. – P. 010501.

11. *Scully M. O.* Quantum Optics / M. O. Scully and S. Zubairy. – Cambridge, England : Cambridge University Press. B., 1997. – P. 166–168.

12. *Sizhuk A. S.* Kinetics and Optical Properties of the Strongly Driven Gas Medium of Interacting Atoms / A. S. Sizhuk and P. R. Hemmer // J. of Stat. Phys., 2012. – Vol. 147. – P. 132.

13. *Sizhuk A. S.* Derivation Of The Model Hamiltonian In "Short Time Scale" Limit / A. S. Sizhuk, S. M. Yezhov // Ukr. J. of Phys., 2012. – Vol. 57. – P. 670–677.

Submitted on 31.03.16

А. Сіжук, канд. фіз.-мат. наук,
кафедра електрофізики,
факультет радіофізики, електроніки та комп'ютерних систем,
Київський національний університет імені Тараса Шевченка, Київ

ПОГЛИНАЛЬНІ ВЛАСТИВОСТІ ГАЗІВ ІЗ КВАНТОВО-ОПТИЧНИМ МЕХАНІЗМОМ ВЗАЄМОДІЇ

Представлено елементи теорії двопроменевої техніки "накачка–зондування" дослідження стимульованого випромінювання та поглинання біля резонансу. Описано метод обчислення коефіцієнта поглинання. Побудовано криву поглинання для області температур парів натрію від 600 до 800 К з використанням аналітичних виразів для макроскопічного коефіцієнта поглинання, попередньо отриманого в кінетичному наближенні для системи, яка взаємодіє з когерентним накачувальним і слабким протилежно напрямленим пробним електромагнітними полями з частотою, що близька до лінії D_2 парів натрію.

Ключові слова: коефіцієнт поглинання, кінетичне рівняння, оптика, атомарний газ, квантова оптика, взаємодія атомів.

А. Сижук, канд. физ.-мат. наук,
кафедра электрофизики,
факультет радиофизики, электроники и компьютерных систем,
Киевский национальный университет имени Тараса Шевченко, Киев

ПОГЛОЩАТЕЛЬНЫЕ СВОЙСТВА ГАЗОВ С КВАНТОВО-ОПТИЧЕСКИМ МЕХАНИЗМОМ ВЗАИМОДЕЙСТВИЯ

Представлены элементы теории двухлучевой техники "накачка–зондирование" исследования стимулированного излучения и поглощения в области резонанса. Описан метод вычисления коэффициента поглощения. Используя аналитические выражения для макроскопического коэффициента поглощения, предварительно полученные в кинетическом приближении для системы, взаимодействующей с когерентным накачивающим и слабым противоположно направленным пробным электромагнитными полями с частотой, близкой к линии D_2 паров натрия, построена кривая поглощения для области температур паров натрия от 600 до 800 К.

Ключевые слова: коэффициент поглощения, кинетическое уравнение, оптика, атомарный газ, квантовая оптика, взаимодействие атомов.

UDC 537.6/.8, 537.86/.87

O. Sulymenko, Ph. D. stud.,
O. Prokopenko, D. Sci., Asc. Prof.,
Department of Nanophysics and Nanoelectronics,
Faculty of Radiophysics, Electronics and Computer Systems,
National Taras Shevchenko University of Kyiv, Kyiv

NUMERICAL STUDY OF THE PHASE SYNCHRONIZATION OF TWO SPIN-TORQUE NANO-OSCILLATORS WITH RANDOM EIGEN FREQUENCIES AND INITIAL PHASES

Numerical analysis of the mutual synchronization of two spin-torque nano-oscillators (STNOs) with random eigen parameters (frequencies and initial phases of oscillations) has been carried out. A numerical procedure for the determination of the system's state (synchronization is present or absent) based on the analysis of the complex order parameter variations over time is proposed. Estimation for the minimum number of simulations required for the robust analysis of the system's state has been made.

Key words: spin-torque nano-oscillator, synchronization, phase model, complex order parameter, numerical analysis procedure.

Introduction. The spin-torque nano-oscillators (STNOs) [2–11, 17–23, 26, 28] based on the spin-transfer torque (STT) [1, 13, 18, 24, 25, 26, 28] effect are now considering as promising base elements for the future electronics. However, if these devices are to be used for practical applications, their microwave characteristics (output power, linewidth and signal-to-noise ratio etc.) must be improved [5, 9, 17, 18, 20, 26, 28]. For instance, this can be done by using the mutual phase-locking of several STNOs [2, 4, 9–11, 14–17, 19, 21–23]. Synchronization of STNOs could also reduce an influence of existing imperfections of STNO's manufacture technology on the oscillators microwave characteristics [2, 5, 9, 17].

In this work we propose a numerical analysis procedure for the mutual synchronization of two STNOs with random eigen parameters. We analyze the stability of the proposed numerical procedure and estimate its efficiency for the case of STNOs having normal distribution of eigen frequencies and uniform distribution of initial phases. We consider the general case of two coupled nano-contact STNOs [13, 18, 21–23, 28] without account of the exact type of coupling. Thus, our results are universal and valid for different types of coupling.

Theoretical model. The microwave magnetization dynamics in two weakly-coupled STNOs is described by the system of coupled nonlinear equations for the complex amplitudes $c_j(t)$ of spin wave modes, excited in *j*-th nano-contact, $j,k=\{1,2\}$ [14–16, 21–23]. In the scope of the generalized phase model [14–16] these equations are transformed to the equations for the generalized phases of the oscillations $\varphi_1(t)$ and $\varphi_2(t)$ for the first and second STNOs, respectively [14–16, 21]:

$$\begin{aligned}\frac{d\varphi_1}{dt}-2\pi f_1&=2\pi\Lambda_{1,2}\sin\left(\varphi_2-\varphi_1+\beta_{1,2}\right),\\ \frac{d\varphi_2}{dt}-2\pi f_2&=2\pi\Lambda_{2,1}\sin\left(\varphi_1-\varphi_2+\beta_{2,1}\right).\end{aligned}\qquad(1)$$

Here f_j is the natural (free-running) frequency of *j*-th oscillator, $\Lambda_{j,k}$ is the amplitude of the coupling between *j*-th and *k*-th oscillators, and $\beta_{j,k}$ is the coupling phase. Both amplitude $\Lambda_{j,k}$ and phase $\beta_{j,k}$ of the coupling are renormalized by the nonlinearity of the oscillators [14–16, 21].

In the experiment, STNO's eigen frequencies f_j may substantially vary from one oscillator to another due to the technological uncertainties during the STNO manufacturing procedure, presence of defects and impurities, etc. Thus, the frequencies f_j should be considered as random quantities having certain probability distribution $P(f_j)$. For simplicity we assume that this probability distribution is the same for each oscillator as well as the mean μ and variance Δf^2 of the distribution. Without loss of generality, we assume that the average frequency $\langle f_j\rangle=\mu$ of the oscillators is about dozen of GHz (otherwise, we can perform transformation $\varphi_j(t)\to\tilde{\varphi}_j(t)=\varphi_j(t)-2\pi\mu t$, that does not change form of Eqs. (1)). Below we consider only the case, where the frequency distribution $P(f_j)$ is the Gaussian distribution:

$$P_G(f_j)=\frac{1}{\Delta f\sqrt{2\pi}}\exp\left[-\frac{1}{2}\left(\frac{f_j-\mu}{\Delta f}\right)^2\right].\qquad(2)$$

The coupling amplitudes $\Lambda_{j,k}$ and phases $\beta_{j,k}$ depend on the coupling mechanism between oscillators and on their properties (nonlinearity). Here we analyze the simplest case of practical interest – the case of global coupling [12, 15], when

$$\Lambda_{j,k}=\Lambda=\text{const},\quad \beta_{j,k}=\beta=\text{const}.\qquad(3)$$

Below we will numerically study the globally-coupled STNOs using model (1) with coupling (3), when the eigen frequencies of the oscillators are distributed by the Gaussian distribution (2). The main subject of study is an influence of the amplitude Λ and phase β of the coupling on the system's state (the synchronization is possible or impossible).

To characterize the state of two weakly-interacting STNO we use the time-dependent complex order parameter [12]:

$$r\equiv r(t)=R(t)e^{i\Psi(t)}=\frac{1}{2}\left(e^{i\varphi_1(t)}+e^{i\varphi_2(t)}\right).\qquad(4)$$

The amplitude $R\equiv R(t)$ of the complex order parameter characterizes the efficiency of phase-locked oscillations, while the rate of the phase change $d\Psi(t)/dt$ gives the frequency of phase-locked oscillations.

As one can see from (4), when the STNO's magnetization oscillations are not synchronized the difference between the phases $\varphi_1(t)$, $\varphi_2(t)$ is not constant and the amplitude R of the order parameter varies over time. Thus the variance of R, ΔR, along with R characterize the existence and stability of the synchronized state. Synchronization of the STNO's magnetization oscillations is possible when the variations ΔR are quite small over some time Δt only

(synchronization is present during this period of time Δt), while the absolute value of R at some time $t = t_0$ characterizes the difference between the phases $\varphi_1(t_0)$, $\varphi_2(t_0)$ only.

Numerical model. Our numerical model is based on the numerical solution of Eqs. (1) for some particular values of $\Lambda_{1,2} = \Lambda_{2,1} = \Lambda$, $\beta_{1,2} = \beta_{2,1} = \beta$, f_1, f_2 and known initial conditions $\varphi_1(0) = 0$, $\varphi_2(0)$. During the numerical calculations we assume that the average value of STNOs' frequencies is $\langle f_1 \rangle = \langle f_2 \rangle = \mu$ and $\Delta t = \mu\zeta$, where ζ is the dimensionless parameter that characterizes imperfection of the system. The initial phase of the second STNO $\varphi_2(0)$ is calculated as random value having rectangular distribution over range $[0; 2\pi]$.

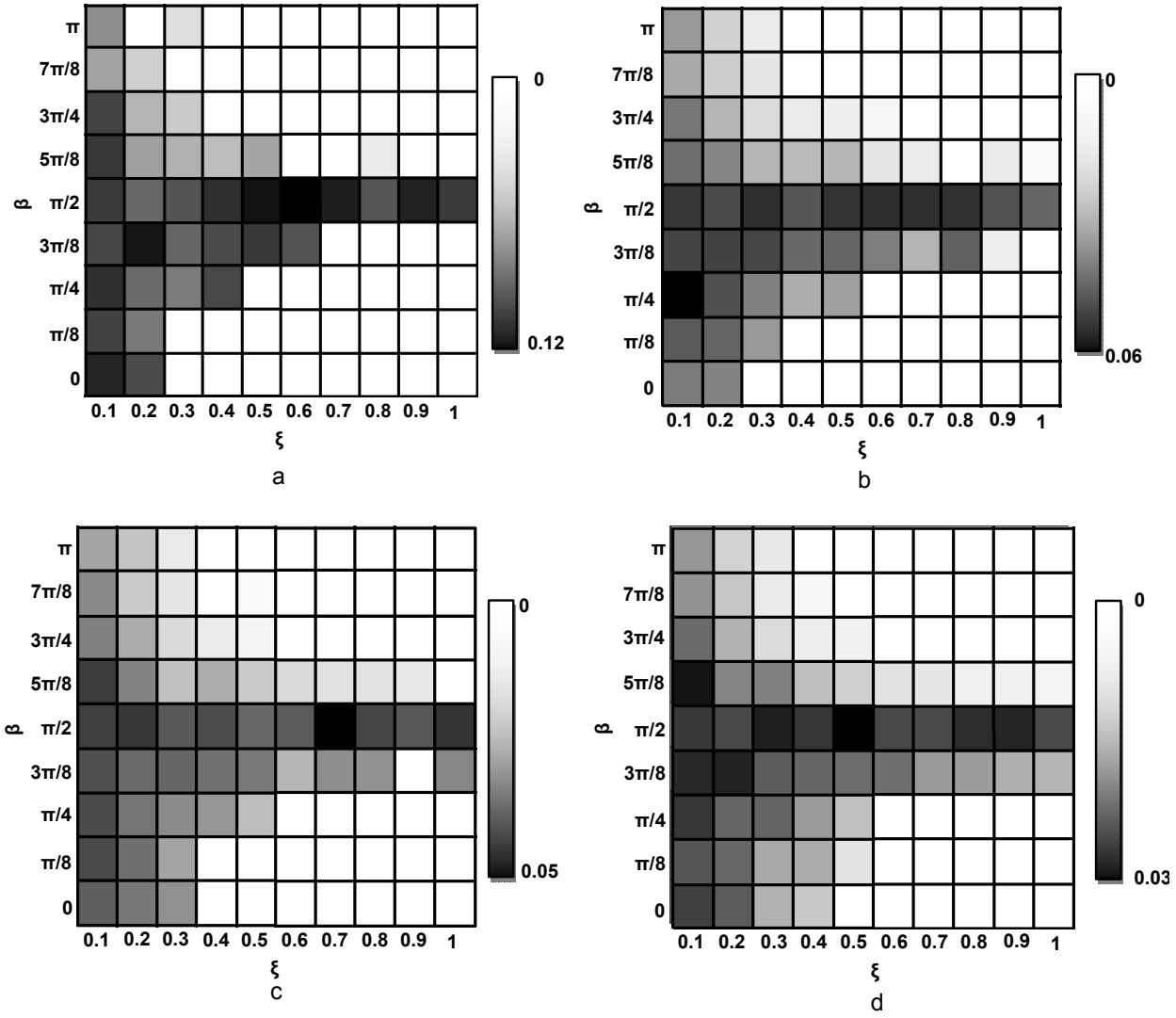

Fig. 1. Dependence of the variance parameter $\langle \Delta R \rangle_{N,\tau}$ [see Eq. (6)] on the phase β and normalized amplitude $\Lambda / 2\pi\mu$ of the coupling for the different number of simulations: (a) *N*=10; (b) *N*=50; (c) *N*=100; (d) *N*=200; μ=12 GHz

The dynamics of general phases $\varphi_1(t)$, $\varphi_2(t)$ depends on random values f_1, f_2, and $\varphi_2(0)$ and, therefore, shows random behavior. To determine the system's state for given μ, ζ we use the following procedure:

1) We choose some particular values of the amplitude ($\Lambda = 2\pi \cdot \xi \cdot \mu$) and phase ($\beta$) of the coupling.

2) For known values of μ and ζ we calculate random frequency values f_1 and f_2 using (2) and $\varphi_2(0) \in [0; 2\pi]$ from the rectangular distribution $P_R(\varphi_2(0)) = 1/2\pi, 0 \le \varphi_2(0) \le 2\pi$ (note, that for simplicity we can let $\varphi_1(0) = 0$).

3) Using previously determined random values $\varphi_1(0) = 0$, $\varphi_2(0)$, f_1, f_2, we numerically solve the equations (1) and get its solution, the phase vector $\vec{\varphi}(t) = \{\varphi_1(t), \varphi_2(t)\}$. Then we calculate the modulus of the complex order parameter as a function of time, $R(t)$, from (4).

4) We repeat steps (2) – (3) N times and for each i-th simulation cycle calculate the modulus of the complex order parameter as a function of time $R_i(t)$ for given random quantities $\varphi_{2,i}(0)$, $f_{1,i}$, $f_{2,i}$, $i = \overline{1,N}$. Then we calculate average value of $\langle R \rangle_N(t)$ as:

$$\langle R \rangle_N(t) = \frac{1}{N} \sum_{i=1}^{N} R_i(t). \qquad (5)$$

5) We choose a period time $[T-\tau;T]$, where the system's state should be analyzed. Here T is the total simulation time, τ τ is the duration of the time period where synchronized state of the system should be checked. To describe the STNOs' state we introduce the average variance parameter

$$\langle \Delta R \rangle_{N,\tau} = \frac{1}{N}\sum_{i=1}^{N}\sqrt{\frac{1}{n}\sum_{j=1}^{n}\left[R_i(t_j)-\langle R\rangle_N(t_j)\right]^2}, \qquad (6)$$

where n is the number of time points t_j in time interval $[T-\tau;T]$, $j=\overline{1,n}$.

6) Then we choose a value of the acceptable relative deviation ρ of the modulus of the system's complex order parameter. If the following inequality

$$\langle \Delta R \rangle_{N,\tau} \le \rho \langle R \rangle_N \qquad (7)$$

is true, then we assume that the STNOs are synchronized, otherwise – the synchronization is absent. In our simulations we use the value of $\rho = 0.01$.

Results and discussion. Using the above described numerical procedure we calculate the dependence of the variance parameter $\langle \Delta R \rangle_{N,\tau}$ [see Eq. (6)] on the phase β and normalized amplitude $\Lambda/2\pi\mu$ of the coupling for the different number of simulations N (Fig. 1). As one can see, the average variance parameter $\langle \Delta R \rangle_{N,\tau}$ substantially depends on the number of simulations N. For small values of N $\langle \Delta R \rangle_{N,\tau}$ could be not statistically stable and might vary in a wide range (see Fig. 1(a)). On the other hand, if the number of simulations N is quite large, the deviations of $\langle \Delta R \rangle_{N,\tau}$ are small (see Fig. 1(d)), but this could also cause an increase of the calculation time and/or accumulation of the computational error. Therefore, there should be an optimal number of simulations N_{opt}, when both the total computation time and computation errors are quite small.

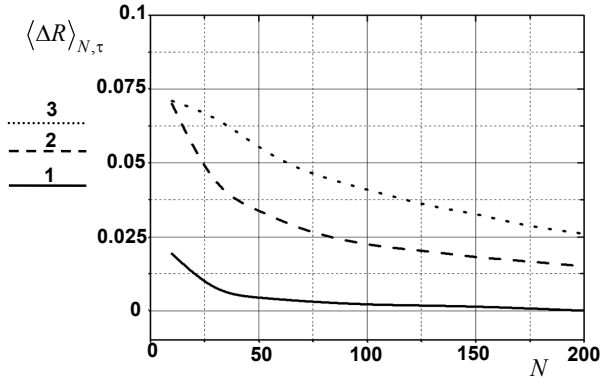

Fig. 2. Dependence of the average variance parameter (6) on the number of simulations: (1) β=0.2π,ξ =0.1; (2) β=0.2 π, ξ=0.5; (3) β=0.5 π, ξ =0.5

Using our numerical data presented in Figs. 1, 2 we can estimate the optimal number of simulations as $N_{\text{opt}} \sim 100$. As one can see from Fig. 2 the characteristic deviations of $\langle \Delta R \rangle_{N,\tau}$ practically do not change or change slowly for $N > 100$. However, the behavior of $\langle \Delta R \rangle_{N,\tau}$ depends on the phase of coupling β and the dimensionless amplitude of coupling parameter ζ. The system's dynamics is the most unstable for $\beta = \pi/2 + 2\pi k$, $k \in Z$ (see curve 3 in Fig. 2). The instability of $\langle \Delta R \rangle_{N,\tau}$ also increases with the increase of ζ.

Conclusion. We developed the numerical analysis procedure to study the dynamics of two weakly-coupled STNOs with random eigen parameters and have demonstrated that the system's dynamics were conveniently described by the average variance of the system's complex order parameter. We have shown that the proposed procedure had quite low computation time, high accuracy and stability when the number of simulations were about $N_{\text{opt}} \sim 100$. We have also shown that the exact optimal number of simulations depend on the phase and amplitude of the coupling between the oscillators.

Publication is partially based on the research provided by the grant support of the State Fund For Fundamental Research of Ukraine (project F64/008).

REFERENCES

1. *Berger L.* Emission of spin waves by a magnetic multilayer traversed by a current / L. Berger // Phys. Rev. B, 1996. – Vol. 54. – P. 9353

2. *Numerical* simulations of the synchronization of an assembly of Spin Transfer Oscillators by the stimulated microwave currents : Influence of delay and linewidth / B. Georges, J. Grollier, V. Cros et al. // Abstracts of the 52th MMM Conf. –2007. – Tampa, FL, USA, Nov. 2007. – CE-10.

3. *Spin-torque* oscillator using a perpendicular polarizer and a planar free layer / D. Houssameddine, U. Ebels, B. Delaët et al. // Nat. Mat., 2007. – Vol. 6. – P. 447–453.

4. *Mutual* phase-locking of microwave spin torque nano-oscillators/ S. Kaka, M. R. Pufall, W. H. Rippard et al. // Nat., 2005. – Vol. 437. – P. 389–392.

5. *Katine J. A.* Device implications of spin-transfer torques / J. A. Katine, E. E. Fullerton // J. Magn. Magn. Mat., 2008. – Vol. 320. – P. 1217–1226.

6. *Microwave* oscillations of a nanomagnet driven by a spin polarized current / S. I. Kiselev, J. C. Sankey, I. N. Krivorotov et al. // Nat., 2003. – Vol. 425.

7. *Time-domain* measurements of nanomagnet dynamics driven by spin-transfer torques/ *I. N. Krivorotov, N. C. Emley, J. C. Sankey et al.* // Sci., – 2005. – Vol. 307. – P. 228–231.

8. *Lee K. J.* Excitations of incoherent spin waves due to spin-transfer torque/ *K. J. Lee, A. Deac, O. Redon et al.* // Nat. Mat., 2004. – Vol. 3. – P. 877.

9. *Locatelli N.* Spin-torque building blocks / N. Locatelli, V. Cros, J. Grollier // Nat. Mat., 2014. – Vol. 13. – P. 11–12.

10. *Phase-locking* in double-point-contact spin-transfer devices / *F. B. Mancoff, N. D. Rizzo, B. N. Engel et al.* // Nat., 2005. – Vol. 437. – P. 393–395.

11. *Persson J.* Phase-locked spin torque oscillators: Impact of device variability and time delay / J. Persson, Y. Zhou, J. Akerman // J. of App. Phys., 2007. – Vol. 101. – P. 09A503.

12. *Pikovsky A.* Synchronization: a universal concept in nonlinear sciences / A. Pikovsky, M. Rosenblum, J. Kurths. – Cambridge, 2007.

13. *Pogorily A. M.* Spintronics. Basic Phenomenoa. Trends of development/ A. M. Pogorily, S. M. Ryabchenko, A. I. Tovstolytkin // Ukr. J. Phys. Rev., 2010. – Vol. 6, № 1. – P. 37–97.

14. *Prokopenko O. V.* Mutual phase-locking of two nano-size magnetic structures considering an influence of signal delay / O. V. Prokopenko // Radio Electronics, Computer Sci., Control, 2010. – Vol. 2. – P. 11–15.

15. *Prokopenko O. V.* Dynamics of generalized phases in a system of two weakly-coupled spin-torque nano-oscillators with random eigen frequencies: the case of global coupling / O. V. Prokopenko, B. I. Karpiak, O. R. Sulymenko // Bulletin of National Taras Shevchenko University of Kyiv. Radiophysics and Electronics, 2013. – № 19. – P. 47–51.

16. *Prokopenko O. V.* Mutual phase-locking of two spin-torque oscillators: Influence of time delay of a coupling signal / *O. Prokopenko, V. Tyberkevych, A. Slavin* // Proc. of the Europe Internat. Magnetics Conf. May 4–8, 2008. – Madrid (Spain). – DP-06.

17. *Prokopenko O.* Spin-Torque Nano-Oscillator as a Microwave Signal Source / O. Prokopenko, E. Bankowski, T. Meitzler et al. // IEEE Magnetics Lett., 2011. – Vol. 2. – P. 3000104–3000104.

18. *Ralph D. C.* Spin Transfer Torques / *D. C. Ralph, M. D. Stiles* // J. Magn. Magn. Mat., 2008. – Vol. 320. – P. 1190–2008.

19. *Phase-locking* of magnetic vortices mediated by antivortices / A. Ruotolo, V. Cros, B. Georges et al. // Nat. Nanotechnology, 2009. – Vol. 4. – P. 528–532.

20. *Silva T. J.* Developments in nano-oscillators based upon spin-transfer point-contact devices / T. J. Silva, W. H. Rippard // J. Magn. Magn. Mat., 2008. – Vol. 320. – P. 393–395.

21. *Slavin A. N.* Nonlinear auto-oscillator theory of microwave generation by spin-polarized current / A. N. Slavin, V. S. Tiberkevich // IEEE Transaction on Magnetics, 2009. – Vol. 47. – P. 1875–1918.

22. *Slavin A. N.* Nonlinear self-phase-locking effect in an array of current-driven magnetic nanocontacts / A. N. Slavin, V. S. Tiberkevich // Phys. Rev. B, 2005. – Vol. 72. – P. 092407.

23. *Slavin A. N.* Theory of mutual phase-locking of spin torque nano-oscillators / A. N. Slavin, V. S. Tiberkevich // Phys. Rev. B, 2006. – Vol. 74. – P. 104401.

24. *Slonczewski J. C.* Current-driven excitation of magnetic multilayers / J. C. Slonczewski // J. Magn. Magn. Mat., 1996. – Vol. 159. – P. L1–L7.

25. *Slonczewski J. C.* Excitation of spin waves by an electric current / J. C. Slonczewski // J. Magn. Magn. Mat., 1999. – Vol. 195. – P. L261–L268.

26. *Extremely* Coherent Microwave Emission from Spin Torque Oscillator Stabilized by Phase Locked Loop / S. Tamaru, H. Kubota, K. Yakushiji et al. // Sci. Reports, 2015. – Vol. 5.

27. *Physical* principles of spintronics / A. I. Tovstolytkin, N. A. Borovoy, V. V. Kuryliuk, Yu. A. Kunickiy. – Vinnitsia, 2014.

28. *Žutić I.* Spintronics: Fundamentals and applications / I. Žutić, J. Fabian, S. D. Sarma // Rev. of Modern Phys., 2004. – Vol. 76. – P. 323.

Submitted on 01.06.16

О. Сулименко, асп.,
О. Прокопенко, д-р фіз.-мат. наук, доц.,
кафедра нанофізики та наноелектроніки,
факультет радіофізики, електроніки та комп'ютерних систем,
Київський національний університет імені Тараса Шевченка, Київ

ЧИСЛОВЕ ДОСЛІДЖЕННЯ ФАЗОВОЇ СИНХРОНІЗАЦІЇ ДВОХ СПІНТРОННИХ МАГНІТНИХ НАНООСЦИЛЯТОРІВ ІЗ ВИПАДКОВИМИ ВЛАСНИМИ ЧАСТОТАМИ ТА ПОЧАТКОВИМИ ФАЗАМИ

Проведено числовий аналіз взаємної фазової синхронізації двох спінтронних магнітних наноосциляторів (СМНО) з випадковими власними параметрами (частотами та початковими фазами коливань). Запропоновано числовий алгоритм для визначення стану системи (є синхронізація, чи немає її), який базується на аналізі часової залежності змін комплексного параметра порядку протягом певного періоду часу. Зроблено оцінку мінімальної кількості моделювань, необхідних для отримання статистично обґрунтованих результатів щодо синхронізації двох СМНО.

Ключові слова: спінтронний магнітний наноосцилятор, синхронізація, фазова модель, комплексний параметр порядку, алгоритм числового аналізу.

О. Сулименко, асп.,
О. Прокопенко, д-р физ.-мат. наук, доц.,
кафедра нанофизики и наноэлектроники,
факультет радиофизики, электроники и компьютерных систем,
Киевский национальный университет имени Тараса Шевченко, Киев

ЧИСЛЕННОЕ ИССЛЕДОВАНИЕ ФАЗОВОЙ СИНХРОНИЗАЦИ ДВУХ СПИНТРОННЫХ МАГНИТНЫХ НАНООСЦИЛЛЯТОРОВ СО СЛУЧАЙНЫМИ СОБСТВЕННЫМИ ЧАСТОТАМИ И НАЧАЛЬНЫМИ ФАЗАМИ

Проведён числовой анализ взаимной фазовой синхронизации двух спинтронных магнитных наноосцилляторов (СМНО) со случайными собственными параметрами (частотами и начальными фазами колебаний). Предложено числовой алгоритм для определения состояния системы (есть синхронизация, или она отсутствует), который основан на анализе временной зависимости изменений комплексного параметра порядка на протяжении определенного временного интервала. Проведена оценка минимального количества моделирований, необходимых для получения статистически обоснованных результатов синхронизации двух СМНО.

Ключевые слова: спинтронный магнитный наноосциллятор, синхронизация, фазовая модель, комплексный параметр порядку, алгоритм численного анализа.

UDC 616-71

D. Titov stud.,
Y. Kyiashko stud.,
T. Afanasieva Ph.D.,
Faculty of Radiophysics, Electronics and Computer Systems,
Taras Shevchenko National University of Kyiv
S. Mamilov Ph. D.,
Institute of Applied Problems of Physics and Biophysics
of National Academy of Sciences of Ukraine, Kyiv

NON-INVASIVE OPTOELECTRONIC DEVICE FOR DETERMINING THE TOXICITY OF CARBON MONOXIDE

The non-invasive mobile device had been developed for determining the oxygen saturation of hemoglobin in arterial and venous blood as well as carboxyhemoglobin level in the blood. The developed device will reveal the poisoning with carbon monoxide in vivo directly on the ground. The device testing showed satisfactory operational results. The correctness of the data processing algorithm has been tested.

Keywords: CO-oximeter, CO-pulse oximeter, carboxyhemoglobin, oxyhemoglobin, saturation, microcontroller, led.

Introduction. The effective treatment of the carbon monoxide poisoning needs a fast identification. Invasive chromatographic and spectrophotometric methods require stationary equipment and hardly fit for use on the place. For fire service and ambulance, it is important to have a compact high-speed device of non-invasive measurement of carboxyhemoglobin concentration in the blood. For example, it can be a pulse oximeter.

The first pulse CO-oximeters appeared not so long ago. Nowadays there are serial pulse CO-oximeter, Rad-57 (Masimo Corporation, the USA) [5] and announced elaboration of a pulse oximeter, which measures HbCO. The last one is made by Nihon Kohden Corporation [7].

Pulse CO-oximeter Rad-57 measures fractional arterial saturation, concentration of carboxyhemoglobin and methemoglobin concentration. Eight wavelengths sensor in the visible range and implemented an original algorithm for signal processing (Masimo Rainbow SET (Signal Extraction Technology)) are used here. 160 volunteers including smokers were involved in a research for precision measuring of carboxyhemoglobin concentrations. It was done by comparison analysis of blood samples on the analyzer ABL-700. The research showed that in the range of HbCO concentration from 0 to 40 % the measurement accuracy is 2,8 % while a coefficient of correlation is 0,97.

Three wavelengths finger sensor was used in the Nihon Kohden pulse oximeter. Experiments, which included inhalation of an air mixture with CO, showed a quite high pulse oximeter (SpCO) and CO-oximetry (SaCO) data correlation (r = 0,92; P < 0,001).

The aim of this work is the develop of a non-invasive optoelectronic device for determining relative concentration of carboxyhemoglobin in the blood.

The spectroscopic method for the determination of carboxyhemoglobin. The hemoglobin molecules can be easily detected by spectrophotometric methods. The variable molecular structure of heme in various hemoglobin derivatives creates unique absorption spectrum [2]. The typical absorption spectra allow determining the concentration of each hemoglobin derivative in a mixture. It was used to develop a method of the measurement of the relative carboxyhemoglobin concentration [4].

The method is a modification of the pulse oximetry method. The number of Beer-Lambert equations in the system determines the number of parameters, which can be defined. The third-longest wavelength is entered to determine the carboxyhemoglobin concentration. Light intensity, which passes through biological tissue, is described by the next equations:

$$I_1 = I_{01} e^{-\left(\varepsilon_{\lambda 1}^{Hb} \cdot c_{Hb} \cdot d + \varepsilon_{\lambda 1}^{O_2} \cdot c_{O_2} \cdot d + \varepsilon_{\lambda 1}^{CO} \cdot c_{CO} \cdot d + \varepsilon_{\lambda 1} \cdot l\right)}$$

$$I_2 = I_{02} e^{-\left(\varepsilon_{\lambda 2}^{Hb} \cdot c_{Hb} \cdot d + \varepsilon_{\lambda 2}^{O_2} \cdot c_{O_2} \cdot d + \varepsilon_{\lambda 2}^{CO} \cdot c_{CO} \cdot d + \varepsilon_{\lambda 2} \cdot l\right)}$$

$$I_3 = I_{03} e^{-\left(\varepsilon_{\lambda 3}^{Hb} \cdot c_{Hb} \cdot d + \varepsilon_{\lambda 3}^{O_2} \cdot c_{O_2} \cdot d + \varepsilon_{\lambda 3}^{CO} \cdot c_{CO} \cdot d + \varepsilon_{\lambda 3} \cdot l\right)}$$

where I_1, I_2, I_3 – the intensities of light passed through the investigated object for three wavelengths respectively; I_{01}, I_{02}, I_{03} – the intensities of light radiated by (light-emitting-diodes) LEDs at three wavelengths respectively; $\varepsilon_{\lambda i}^{Hb}$, $\varepsilon_{\lambda i}^{O_2}$, $\varepsilon_{\lambda i}^{CO}$, $\varepsilon_{\lambda i}$ – the absorption coefficients of deoxyhemoglobin (Hb), oxyhemoglobin (HbO2), carboxyhemoglobin (HbCO) and bloodless tissue (depending on the wavelength); c_{Hb}, c_{O_2}, c_{CO} – the concentrations of deoxyhemoglobin, carboxyhemoglobin and oxyhemoglobin respectively; d – the thickness of the blood layer; l – the thickness of bloodless tissue.

Light intensity modulation by pulse wave of blood allows to exclude components, which do not pulse, (biological tissues) and it helps to get the expression of relative carboxyhemoglobin concentration such as [8]:

$$S_{HbCO} = f(\varepsilon_{\lambda i}^{CO}, \varepsilon_{\lambda i}^{Hb}, \varepsilon_{\lambda i}^{O_2}, R_{21}, R_{31}), \qquad (1)$$

where R_{21} – the coefficient of linear regression of logarithms (or ratio of modulation coefficients) values of light signals at the first and the second wavelengths; R_{31} – the coefficient of linear regression of logarithms (or ratio of modulation coefficients) values of light signals at the first and the second wavelengths on the third and the first wavelengths.

The analysis of the spectra shows that to detect the carboxyhemoglobin in the blood using the optical method in the visible range it is reasonable to use a radiation source in the range of 550 to 570 nm which has a quite narrow emission band with a maximum around 565 nm.

The L-53MGC (Kingbright) typed LEDs or their analogies in InGaAlP with λ_{max} = 568 nm are the most suitable for the range of commercially available LEDs.

Architecture and circuit design. We used the following architecture to accomplish the task: the microcomputer with a relatively high capacity which using UART interface connects to the microcontroller with a large set of necessary peripherals (ADC, DAC, digital inputs/outputs, etc.) was applied as a device for the collection and processing of data. The microcontroller manages the pulse oximetry sensor operations (selecting a

channel and adjusting the brightness), selects the reference voltage value of the 2nd stage of the amplifier of the current-voltage converter for cleaning some part of a constant component and measuring the output voltage.

The possibility of adding other sensors (the concentration of CO and CO_2 in exhaled air, etc) for a more accurate diagnosis of poisoning by carbon monoxide was provided. While developing the software, the most abstract level methods to operate with the peripherals and to control the microcontroller by the microcomputer were implemented.

We select the Raspberry Pi 2 model b as the microcomputer due to a large set of interfaces (CSI Camera interface, DSI Display interface, Ethernet, HDMI, MicroSD card reader, etc.) and high performance (4 cores architecture ARM Cortex-A7 900 MHz, 1 GB DDR2 RAM).

The STM32F100C8T6 microcontroller was used. Due to the high bit depth ADC and DAC (12 bit), it allows the measurement of the output signal from the amplifier with high accuracy and generating a reference signal in the 2nd stage of the amplifier.

Sensor for measuring relative concentrations of the hemoglobin forms has the same design as Palava pulse oximetry sensor and consists of 3 x light emitting diodes with wavelengths of 568, 660, 940 nm and a *BPW34* photodiode.

The control of the LED brightness is performed by using a digital-to-analog converter according to the scheme shown in Fig. 1. In this circuit, the transistors work in a key mode. Opening/closing of the transistors is implemented with a digital controller outputs *PA3, PA6, PA7*. The voltage at these outputs is 3.3 V. So, taking into account the bitness of the DAC, the resulting step change in voltage at the DAC output is $8 \cdot 10^{-4}$ V. In this way, the calibration of the pulse oximeter is provided depending on the physiological characteristics of the investigated area of the patient's body.

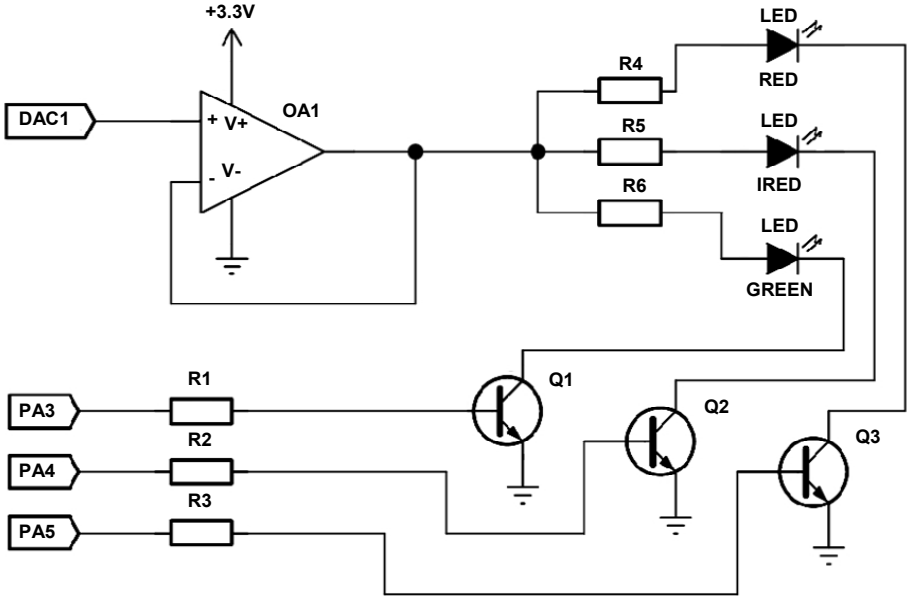

Fig. 1 The control scheme of LED

The amplifier circuit as shown in Fig. 2 consists of two cascades. The first stage is the current-voltage converter, which converts the received photodiode current of a few μA into a corresponding voltage of 10^{-3} V. The high-pass filter reduces interference from background light. To be sure that an output signal level of the amplifier is in the ADC working range we made the circuits with the output voltage control (ADC1) and the reference voltage generation (DAC2). The second stage is the amplification voltage scheme used the operational amplifier. It amplifies the voltage to the level of the operating range of the ADC.

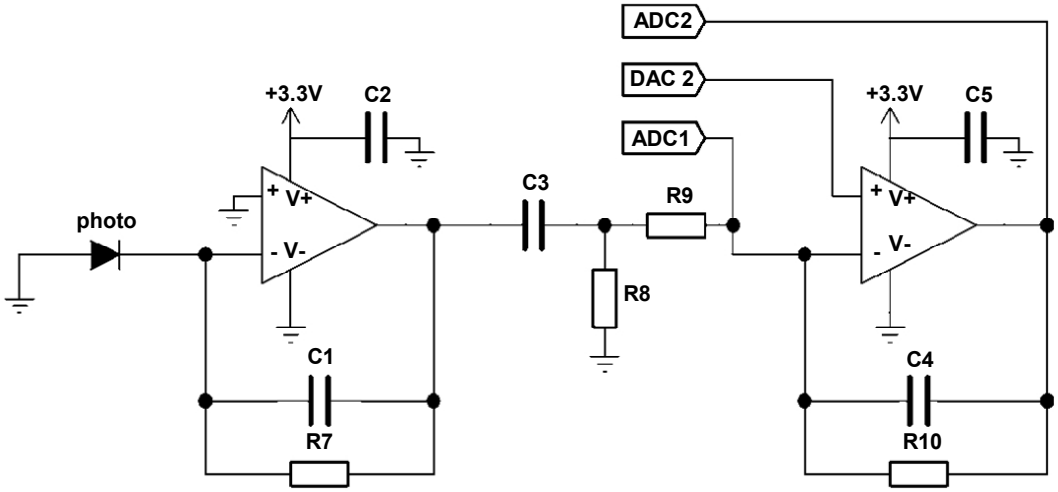

Fig. 2. The scheme of amplification

Through a non-frequency nature of interference which makes a basic error in the measurement of relative concentrations of hemoglobin forms, the use of classical filtering methods is ineffective. To solve this problem the method of adaptive filtering described in reference [1] was considered.

The adaptive filter consists of two parts: a digital filter with adjusting coefficients and the adaptive algorithm that is used to set or modify the filter coefficients.

The use of the adaptive filter is allowed to determine the level of SpO_2 and HbCO in the arterial blood by searching the maximum output power of the filter as follows [6]. At first, we generate a reference signal $N_r = rI_{ir} - I_r$ (where r – the ratio of the change in the intensity of the infrared to the red channel, I_{ir} – the intensity of infrared light passed through the investigated area, I_r – the intensity of the red light) by changing r from 1 to 100.

Then we supply a reference signal to the adaptive filter as a signal which contains information about the error and the raw signal from the red channel. From this data, we calculate the output power of the adaptive filter and determine the r value in which the output power of the filter reaches a maximum value. Obtained value r is used for the determination of oxygen saturation in the arterial blood.

This process can be described by the flowchart shown in Fig. 3.

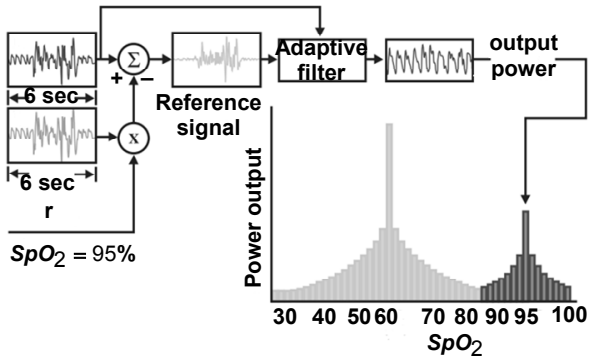

Fig. 3. The flowchart for finding the values of r_a and r_v

The *Free RTOS* operating system is used to manage the resources of the microcontroller. The use of the *Free RTOS* operation system simplifies the dispatching of threads, tracking of the digital inputs/outputs states, the reception and transmission of information via interfaces for data exchange, the works with constant memory and time control.

Since the Raspberry Pi single Board computer is a complex device so the Linux operating system is used to control of their resources. Due to high demands on the device start time the use of the existing operating system distributions through their redundancy and as a consequence unacceptable load time, which was 28-32 seconds has eliminated. To decrease the loading time we had to rewrite the makefiles and to compile the Linux kernel with a set of the Buildroot build tools. The result, the loading time reduces to 3.4 seconds.

To receive data from the controller and further processing and storage on the microcomputer the program in the programming language C++ using the Qt was created. The program allows determining the relative concentration of carboxyhemoglobin in the arterial blood and oxygen saturation of arterial and venous blood.

To test the ability of the device to detect changes in the concentration of HbCO was carried out an experiment in which the person that is not smoked for over 12 hours, was taken to plethysmogram to Smoking and 5 minutes after Smoking. For reasons of clarity, the Smoking process was carried out immediately after removal of the first plethysmogram. The results are shown in figure 4.

As can be seen from figure 4 it has changed the value of the coefficient R_{23} (between infrared and green channels). The change in this ratio is confirming the ability of the device to respond to changes of carboxyhemoglobin in the blood and is used to calibrate the device.

Calibration of the device is quite complicated and lengthy process that is costly, as time and material. For the calibration process cannot be overlooked and the value of R_{13} (between the red and green channels) through the strong similarity of the absorption spectra of the investigated forms of hemoglobin in the field of green-orange light, so the calibration was not carried out.

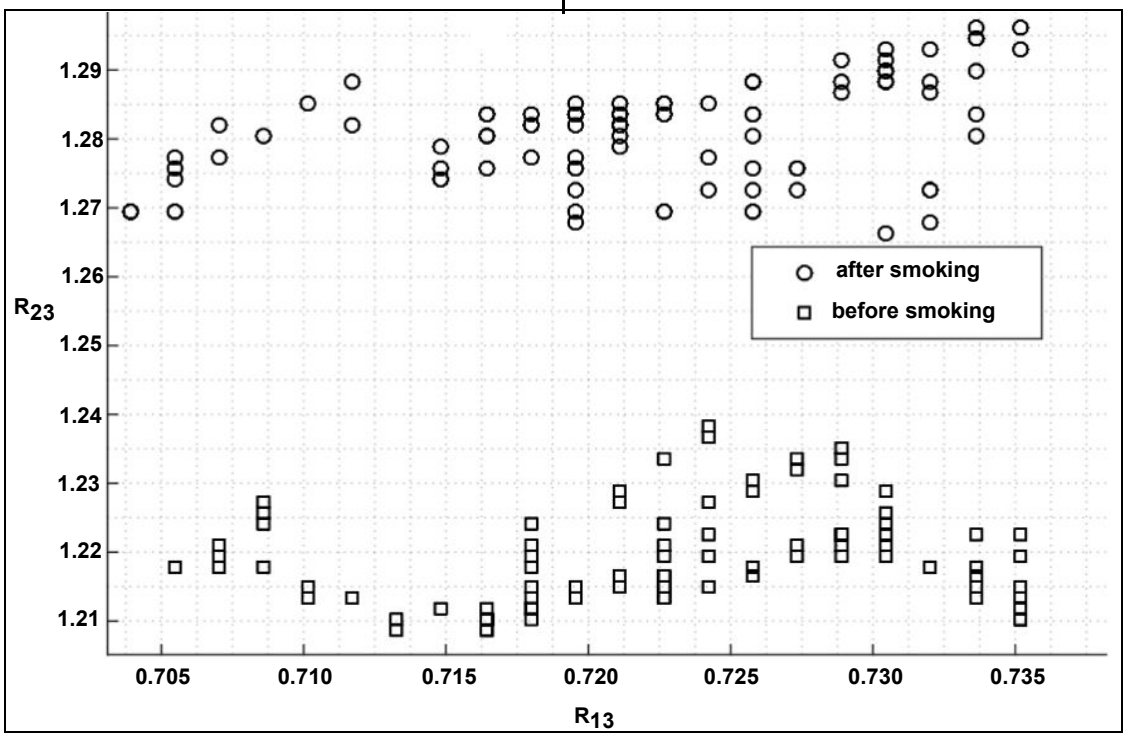

Fig. 4. A graph of the values of the coefficients R_{13}, R_{23} during the experiment with Smoking

To check the correctness of the implemented algorithm, the test plethysmograph was processed using our program and the implementation of the ICAMF (Mean Field Independent Component Analysis) method. The ICAMF method has the highest accuracy among the known methods (value SpO_2 average deviation of 2.6 % vs. 3.0 % in the DST (Discrete Saturation Transform) as was shown in the study of Technical University of Denmark [3]. The results of the comparison are shown in Fig. 5.

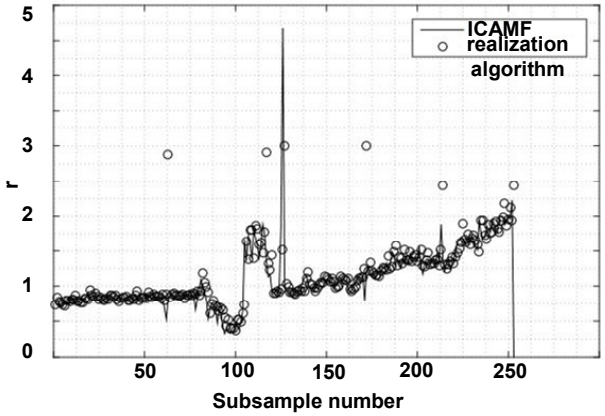

Fig. 5. The comparison between ICAMF method and the implemented algorithm

The value of the average deviation relative to ICAMF amounted to 4 %, which can be considered a satisfactory result.

Conclusion. Thus, the device for determining the relative concentration of carboxyhemoglobin in the arterial blood, and the oxygen saturation of arterial and venous blood using the non-invasive method was developed. The simultaneous determination of these parameters in vivo allows investigating the processes of the oxygen transport in the conditions of strong and moderate poisoning with carbon monoxide, including anthropogenic origin.

REFERENCE

1. *Ifeachor E. C.* Digital signal processing. A practical approach / E. C. Ifeachor, B. W. Jervis. 2nd ed. Prentice Hall, 2001. – P. 960.

2. *Blumenfeld L. A.* Hemoglobin / L. A. Blumenfeld // Chemistry. Soros educational journal, 1998. – № 4. – P. 33–38.

3. *Independent* Component Analysis Applied to Pulse Oximetry in the Estimation of the Arterial Oxygen Saturation (SpO_2) a Comparative Study : [electronic resource]. – URL: http://orbit.dtu.dk/files/4583254/Jensen.pdf.

4. *Mamilov S. A.* Photodissociate molecules of oxy-and carboxyhemoglobin in arterial blood / S. A. Mamilov, Yesman S. S., I. V. Glebova // Bulletin of Lviv University. The biology series, 2014. – Ed. 68. – P. 325–337.

5. *Masimo Co.* A New Noninvasive Parameter&$SpCO^{TM}$ – Pulse CO-Oximetry^{TM} : [electronic resource]. – URL: http://www.masimo.fr/pdf /whitepaper/LAB4090B.pdf.

6. *Masimo Co.* Signal Extraction Technology : [electronic resource]. – URL: http://www.masimo.fr/pdf/whitepaper/LAB1035R.pdf.

7. *Non-invasive* measurement of carboxyhemoglobin (HbCO) by new pulse oximeter in human volunteers / Y. Sato, K. Ikegami, Y. Kuno et al. // Abstracts of 22nd Internat. Symposium on Intensive Care and Emergency Medicine. – Brussels, 2002. – P. 189.

8. *Mamilov S. A.* Method of determining the relative concentration of carboxyhemoglobin in arterial blood : The Patent of Ukraine No 89354 / S. A. Mamilov, J. S. Keen, S. S. Yesman, 2010. – Bull. No 2/2010.

Submitted on 17.06.16

Д. Тітов, студ.,
Ю. Кияшко, студ.,
Т. Афанас'єва, канд. фіз.-мат. наук,
факультет радіофізики, електроніки та комп'ютерних систем,
Київський національний університет імені Тараса Шевченка, Київ,
С. Мамілов, канд. фіз.-мат. наук,
Національна академія наук України,
Інститут прикладних проблем фізики і біофізики, Київ

НЕІНВАЗИВНИЙ ОПТОЕЛЕКТРОННИЙ ПРИСТРІЙ ДЛЯ ВИЗНАЧЕННЯ ОТРУЄННЯ МОНООКСИДОМ ВУГЛЕЦЮ

Розроблено неінвазивний мобільний пристрій для визначення рівня насичення артеріальної та венозної крові киснем і вмісту карбоксигемоглобіну в крові, що дозволить виявляти отруєння монооксидом вуглецю in vivo безпосередньо на місці подій. Апробація пристрою показала задовільні результати його роботи. Перевірено коректність роботи реалізованого алгоритму для обробки даних.

Ключові слова: CO-оксиметр, CO-пульсоксиметр, карбоксигемоглобін, оксигемоглобін, сатурація, мікроконтролер, світлодіод.

Д. Титов студ.,
Ю. Кияшко студ.,
Т. Афанасьева, канд. физ.-мат. наук,
факультет радиофизики, электроники и компьютерных систем,
Киевский национальный университет имени Тараса Шевченко,
С. Мамилов[1], канд. физ.-мат. наук,
Национальная академия наук Украины, Киев,
[1]Институт прикладных проблем физики и биофизики, Киев

НЕИНВАЗИВНОЕ ОПТОЭЛЕКТРОНННОЕ УСТРОЙСТВО ДЛЯ ОПРЕДЕЛЕНИЯ ОТРАВЛЕНИЯ МОНООКСИДОМ УГЛЕРОДА

Разработано неинвазивное мобильное устройство для определения уровня насыщения артериальной и венозной крови кислородом и содержания карбоксигемоглобина в крови, что позволит выявлять отравления монооксидом углерода in vivo непосредственно на месте событий. Апробация устройства показала удовлетворительные результаты работы устройства. Проверенная корректность работы реализованного алгоритма для обработки данных.

Ключевые слова: CO-оксиметр, CO-пульсоксиметр, карбоксигемоглобин, оксигемоглобин, сатурация, микроконтроллер, светодиод.

UDC 535.33

T. Tmenova, Ph. D., stud.,
A. Veklich, D. Sci.,
V. Boretskij, Ph. D.,
Department of Physical Electronics,
Faculty of Radiophysics, Electronics and Computer Systems,
National Taras Shevchenko University of Kyiv, Kyiv

CALIBRATION OF SPECTRAL RESPONSE OF THE SDH-IV SPECTROMETER

In the last few years, low temperature plasmas have been used more and more in a great number of scientific and technological fields, and optical emission spectroscopy (OES) has been the most commonly used technique for their analysis. The usual optical system employed for plasma diagnostics is composed of a spectrometer or monochromator, detector and optical fiber or lenses, which must be calibrated to correct the different spectral responses of each component in this system. Therefore, methodological guidelines for determination and calibration of spectral response of optical instruments are presented through the calculation of spectral sensitivity of the high-aperture compact SDH-IV spectrometer in the spectral range from 345 to 605 nm. Calibration of spectrum was performed by fitting of measured emission of a tungsten ribbon lamp and halogen lamp to theoretically calculated values.

Keywords: spectral sensitivity, spectrometer, tungsten ribbon lamp, halogen lamp, blackbody, wavelength, emission coefficient.

Introduction. During the last half century, low-temperature plasmas have made a dramatic impact on society, significantly improved the quality of life, and provided challenging scientific problems. Examples are the fluorescent lights that can be found in almost every home; high-power switches that control the electrical grids; gas discharge lasers, including the red He-Ne laser, which was the first gas laser invented, and the high-power, infrared, CO_2 lasers that are used daily in surgery and metal working; and plasma sources that provide positive and negative ions for ion-beam accelerators. These ion sources are used to implant ions into materials, including semiconductor chips for the computer industry, and to harden bearings to increase the life and reliability of high-performance engines. Provided the opportunity, the field of low-temperature plasma will continue to make significant contributions [1].

In order to understand the possible advantages of a given plasma, it is necessary to know the energy available in it, mainly in the form of the kinetic energy of the electrons and heavy particles (such as atoms and ions), measurable by means of electron temperature Te and gas temperature Tg, respectively. Other parameters of the discharge, such as the electron (ne), atom (in several excited states, np), and ion (n+) densities, also determine its capability for the excitation or ionization of the atom and molecules introduced into plasma. Atom and ion densities describe the atomic state distribution function (ASDF) of the discharge, which informs how the atoms and ions are distributed in their different excited states. Moreover, this distribution describes the degree of thermodynamic equilibrium in plasma, which is related directly to the processes (internal kinetics) that take place during the discharge and the possibility of using plasma for different scientific and technological purposes.

Among all the techniques dedicated to the study of plasmas, based on analysis of the light emitted by plasma, optical emission spectroscopy (OES) is one of great interest due to its non-disturbing character which does not modify discharge kinetics.

Generally, the system employed in OES is made up of a monochromator that selects the wavelength of the electromagnetic radiation emitted by plasma to be registered, or a spectrometer, a detector that transforms the luminous signal into an electrical one and a system of lenses or an optical fiber that picks up the radiation emitted by plasma and drives it to the entrance slit of corresponding optical device.

The components of the optical system have a different intensity response to each wavelength. So, prior to its application in order to analyze the radiation emitted by any light source, its intensity calibration is required [2]. The latter can be performed in one of the two ways: either the absolute spectral responsivity of a detector with respect to a primary detector standard is determined, or the detectors (or, more generally, detector-based systems) are calibrated through using known sources of spectral radiation. The absolute determination of detector spectral responsivity requires sophisticated measurement equipment and methods, available only in a limited number of national metrology institutes (NMIs), therefore nearly all calibrations of instruments used for the measurement of thermal radiation are performed using accurately known sources of spectral radiation. In principle, two sources of calculated spectral radiation are available, either synchrotron sources calculable using the Schwinger equation or blackbody sources calculable using the Planck function [3]. In practice, due to the major investment required to acquire a synchrotron source, only the application of blackbody radiation offers a practical solution for instrument calibration at nearly all NMIs and calibration laboratories. Therefore, intensity calibration lies in the comparison between the radiation emitted by a standard light source, whose emission is known, and this radiation registered by the optical system.

In this paper, authors have determined a spectral sensitivity of the spectrometer SDH-IV in the spectral range 345–605 nm.

Theory. Blackbody radiation. Kirchhoff in 1860 introduced the theoretical concept of a perfect blackbody, the emission of which does not depend on its physical or chemical properties and its composition, and does depend only on temperature. Such body is expected to completely absorb all incident radiation, and neither reflect nor transmit any. This holds for radiation of all wavelengths and for all angles of incidence. A blackbody in thermal equilibrium (i.e. at a constant temperature) emits electromagnetic radiation called the blackbody radiation, which is described by Planck's law. The spectral radiance of a body, Bv, describes the amount of energy it gives off as radiation of different frequencies. It is measured in terms of the power emitted per unit area of the body, per unit solid angle that the radiation is measured over, per unit frequency. Planck showed that the spectral radiance of a body at absolute temperature T is given by:

$$B_{\nu}(\nu,T)=\frac{2h\nu^3}{c^2}\frac{1}{e^{\frac{h\nu}{k_BT}}-1}, \qquad (1)$$

where k_b is the Boltzmann constant, h is the Planck constant, and c is the speed of light in the medium, whether material or vacuum. The spectral radiance can also be measured per unit wavelength instead of per unit frequency. In this case, it is given by:

$$B_{\lambda}(\lambda,T)=\frac{2hc^2}{\lambda^5}\frac{1}{e^{\frac{hc}{\lambda k_BT}}-1}. \qquad (2)$$

In the limit of low frequencies (i.e. long wavelengths), Planck's law tends to the Rayleigh-Jeans law, while in the limit of high frequencies (i.e. small wavelengths) it tends to the Wien approximation [1].

Kirchhoff's law of thermal radiation. Idealized blackbodies do not exist in nature. To quantify how close a practical blackbody is to an ideal blackbody the concept of emissivity has been introduced. Emissivity is a measure of the deviation of the ability of a real surface to emit thermal radiation in comparison to an ideal blackbody. The emissivity of a real surface is, in principle, a function of wavelength, temperature and angle of view. Emissivity is measured by determining the ratio of the spectral radiance of the source/surface with respect to the spectral radiance of an ideal blackbody at the same temperature.

If we consider a system consisting of several bodies and residing in the state of thermal and radiative equilibrium, and one of the bodies is the blackbody, then one can say that the Kirchhoff's law of thermal radiation holds for such system. The law states that for any material at all, radiating and absorbing in thermodynamic equilibrium at any given temperature T, for every wavelength λ, the ratio of emissive power to absorptive power has a universal value, which is characteristic of a perfect blackbody, and is an emissive power which is here represented by Bλ(λ,T). It can be illustrated with the following relation:

$$\frac{B_1(\lambda,T)}{\alpha_1(\lambda,T)}=\frac{B_i(\lambda,T)}{\alpha_i(\lambda,T)}=\ldots=\frac{B_n(\lambda,T)}{\alpha_n(\lambda,T)}=f(\lambda,T)=B_{\lambda,T}, \quad (3)$$

where Bλ,T is a spectral radiance of the blackbody for the wavelength λ at temperature T, Bi(λ,T) and αi(λ,T) – spectral radiance and absorptivity of the i-th body at the absolute temperature T.

On the basis of Kirchhoff's law, spectral radiance of any body at all can be expressed through the spectral radiance of a blackbody:

$$B_i(\lambda,T)=\alpha_i(\lambda,T)\cdot B_{\lambda,T}. \quad (4)$$

From the radiant energy emitted, in turn, the temperature of bodies may be estimated, and that forms a principle on which optical pyrometry is based. Therefore, the temperature of the incandescent bodies is measured via optical methods without direct contact with body [4].

Optical pyrometry. Up to the present date, optical pyrometry methods are the only one used for measurements of high temperatures (above 2000 K). The calculation error in case of application of these methods comes up to a few percent.

Whereas the radiation of real bodies differs from that of the blackbody, measurement of their temperatures in accordance with the laws of blackbody emission has its peculiarities. The more selective is the radiation of real body, the more evident are these peculiarities. Depending on the applied law of radiation, following three types of temperatures are considered: radiant, color and brightness temperature. These temperatures are somehow related to the true body temperature. The latter is the temperature of thermometric body residing in the thermal equilibrium with the emitting body [1].

Radiant temperature. Radiant temperature can be obtained on the basis of the Stefan–Boltzmann law. Specifically, the Stefan–Boltzmann law states that the total energy radiated per unit surface area of a blackbody across all wavelengths per unit time (also known as the blackbody radiant exitance or emissive power), R_e is directly proportional to the fourth power of the blackbody's thermodynamic temperature T_r:

$$R_e=\sigma T_r^4. \quad (5)$$

The constant of proportionality σ, called the Stefan–Boltzmann constant derives from other known constants of nature. The value of the constant is

$$\sigma=\frac{2\pi^5 k_B^4}{15c^2h^3}=5.670373\times10^{-8}, \quad \mathrm{W^{-8}m^{-2}K^{-4}}.$$

Temperature, obtained from (5), is temperature of the blackbody. If body whose temperature is being measured is real, then radiative pyrometer will determine only its radiant temperature. The latter equals to the blackbody temperature, radiosity of which equals to that of the given body [1].

Color temperature. Color temperature of the body is the blackbody temperature, whereby the maximum of its emissive power coincides with that of the real body. Such temperature can be determined on the basis of the Wien's law. Once the wavelength corresponding to the emissive power maximum is determined, we have:

$$T_c=\frac{0.2898}{\lambda_{\max}}, \quad (6)$$

where Tc is the color temperature, λmax is the wavelength in cm.

Color temperature of the body differs from its true temperature. True temperature of the given body can be obtained from the following formula:

$$\frac{1}{T_{true}}=\frac{1}{T_c}+\frac{\ln\dfrac{b'_{\lambda_1}}{b_{\lambda_1}}:\dfrac{b'_{\lambda 2}}{b_{\lambda 2}}}{C_2\left(\dfrac{1}{\lambda_1}-\dfrac{1}{\lambda_2}\right)}, \quad (7)$$

where $b'_{\lambda 1}$ and $b'_{\lambda 2}$ are the emissive powers of the body for two different values of wavelength, respectively, $b_{\lambda 1}$ and $b_{\lambda 2}$ are the emissive powers of blackbody for the same wavelength values, C_2 = 0.01439 m·K [1].

Brightness temperature. Once the brightness of body in the range of wavelength λ, λ+dλ is determined, brightness temperature can be obtained using the Planck's law. Calculations of a numerical value of spectral brightness are complicated enough, therefore this procedure is limited by comparison of brightness of a studied body in wavelength range λ, λ+dλ and brightness of a standard emission source. Generally, such measurements are performed at wavelength 0.665 μm – an effective wavelength of a pyrometer.

Determination of body temperature by its brightness is the most common method of an optical pyrometry. It can be carried out using disappearing filament pyrometer. The simplest design is shown in Fig. 1. A thin wire (filament), placed at the focal plane of the objective lens, is heated by electric current. When seen through the eyepiece, the wire appears silhouetted in front of the hot luminous object under investigation. The user compares the brightness of the glowing filament with the object behind, and adjusts the current through the filament until it seems to "disappear" in front of the glowing object. At that point the filament and object are at the same temperature. The user then reads the temperature off the filament current control dial, which is calibrated by the filament's current-vs-temperature curve or in some instruments from a current-vs-temperature table [1].

If studied body is a blackbody, then temperature, determined in such way, will be its true temperature. If real body differs from a blackbody, then such temperature will be its brightness temperature. Relation between true and brightness temperatures can be expressed by the following equation:

$$T_{true}=\frac{C_2T_b}{\lambda T_b\ln\varepsilon_{\lambda,T}+C_2}, \quad (8)$$

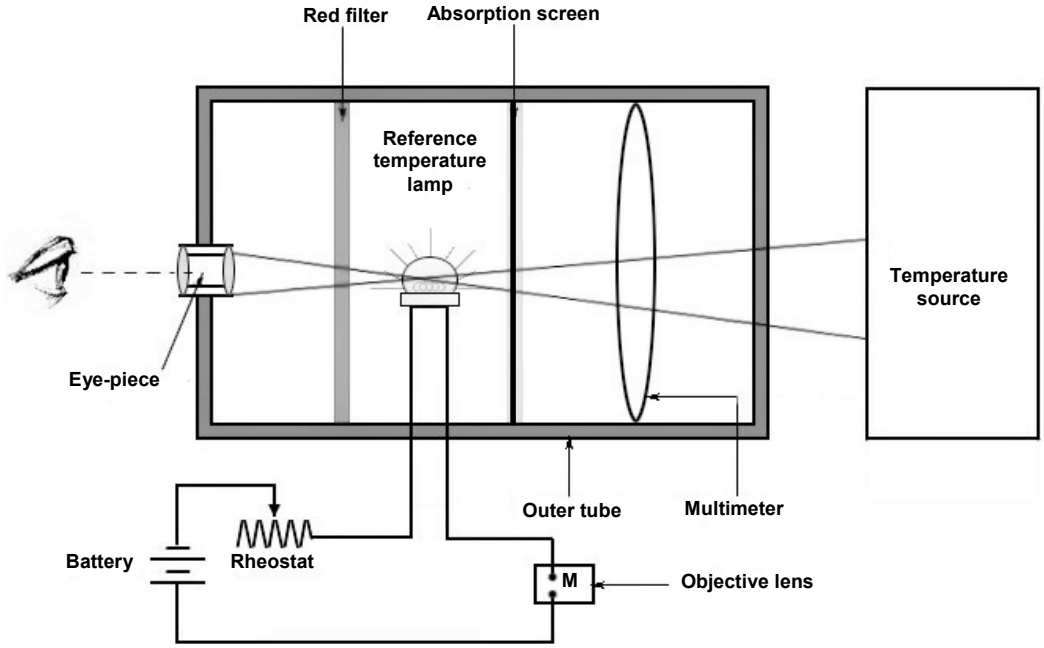

Fig. 1. Scheme of disappearing filament pyrometer [2]

where T_b is the brightness temperature, $\varepsilon_{\lambda,T}$ is the emissivity coefficient of the body.

Standard sources of emission. It would be convenient to use a standard emission source, emission of which is close to the emission of a perfect blackbody. Such radiation sources (artificial blackbodies) exist, but their exploitation is associated with significant experimental difficulties. Thus, they are mainly used in particular metrological laboratories for calibration of secondary standard light sources. As for today, the most commonly exploited secondary sources of radiation are tungsten ribbon lamps, commercial halogen lamps, deuterium lamps, etc.

According to the Kirchhoff's law, theoretical emissivity of the lamp at temperature T is given by:

$$B_e(\lambda,T) = \tau_0(\lambda)\varepsilon(\lambda,T)b(\lambda,T), \qquad (9)$$

where $\varepsilon(\lambda,T)$ is the emission coefficient of tungsten as a non-blackbody ($\varepsilon(\lambda,T)<1$), which depends on wavelength and true temperature of tungsten, $\tau_0(\lambda)$ is the transmission coefficient of the lamp's window, $b(\lambda,T)$ is the blackbody brightness at the same temperature T. As an example, emissivity of tungsten as a function of wavelength for different values of temperature are shown in Fig. 2 [4].

According to the brightness temperature definition:

$$b(\lambda,T_b) = B_e(\lambda,T) = \tau_0(\lambda)\varepsilon(\lambda,T)b(\lambda,T). \qquad (10)$$

Since the tungsten emission coefficient $\varepsilon(\lambda,T)$ depends on wavelength λ and true temperature of tungsten T, therefore the brightness temperature T_b depends on λ and T.

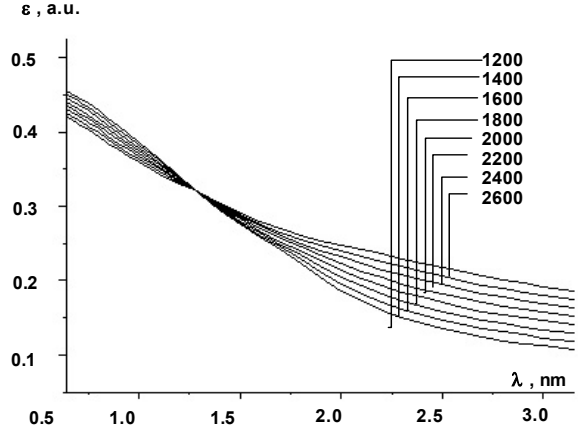

Fig. 2. Spectral emissivity of tungsten as a function of wavelength for different values of temperature [4]

Equations (10) and (2) allows us to find a relation between the brightness and true temperatures of tungsten:

$$\frac{1}{T}-\frac{1}{T_b}=\frac{\lambda}{c_2}\ln[\tau_0(\lambda)\varepsilon(\lambda,T)], \qquad (11)$$

which holds for $\lambda T<0.3$ cm·K (for instance, at $T < 3000$ K and $\lambda_0<1$ μm) within the error of 1 %.

Generally, the brightness temperature of tungsten ribbon lamps in the process of their calibration is being determined for the effective wavelength $\lambda_0 = 0.65$ μm. After substitution of λ_0 and c_2 into (11), the following formula is obtained:

$$\frac{1}{T}-\frac{1}{T_b}=1.041\times10^{-4}\lg[\tau_0(\lambda)\varepsilon(\lambda,T)], \qquad (12)$$

where $\tau_0(\lambda) \approx 0.92$ and $\varepsilon(\lambda,T)$ is the tungsten emission coefficient for $\lambda_0 = 0.65$ μm at temperature T.

Equation (12) allows to determine the true temperature of tungsten T upon condition that the brightness temperature T_b is known for the given standard lamp. Considering that the emission coefficient $\varepsilon(\lambda,T)$ weakly depends on the temperature, then, at a first approximation, the value of T' is determined from (12) for $\varepsilon(\lambda_0,T)$, and, afterwards, the value of T is determined for $\varepsilon(\lambda_0,T')$. The value of T, obtained in such manner, allows us on the basis of (9) to perform further calculation of absolute value of the tungsten lamp spectral emissivity $B_e(\lambda,T)$ for every wavelength λ using experimentally measured values of $\varepsilon(\lambda,T)$ and obtained values of $b(\lambda,T)$ for various λ and T. Theoretical values of $\varepsilon(\lambda,T)$ for tungsten are presented in Table 1 [5].

In process of calibration of tungsten ribbon lamps, operating current or voltage is registered, using which the lamp brightness temperature is determined, as well as other parameters of lamp's operation mode and setup (spatial orientation, polarity of the current source, the region of the radiating body that is being calibrated, etc.).

It is also worth noting that emission coefficient of tungsten $\varepsilon(\lambda,T)$ depends on chemical purity of the tungsten foil, quality of its surface and technology of its production. Therefore, the values $\varepsilon(\lambda,T)$ of real standard lamps may differ from that found in literature.

Moreover, it is also required to take into account the absorption in the glass, of which the lamp body is made, since it varies depending on the wavelength. The absorption spectrum of ПС-5 glass, of which the tungsten ribbon lamp used in calibration is made, can be found in Table 2 [5].

Brightness of the continuous spectra of tungsten incandescent lamps decreases rapidly in the UV region (<300 nm), therefore it is not reasonable to use them for work in this spectral region. As alternative, the hydrogen-discharge (deuterium) low-pressure lamps are usually applied.

Description of the optical system to be calibrated. The optical system is depicted in Fig. 3 and it was composed of the SDH-IV spectrometer with a 4-position manually switchable diffraction gratings turret. The second channel of spectrometer was set for measurements, so the registered spectral range was 345–605 nm. The CCDs used as detectors were Toshiba TCD 1304 AP linear image sensors. The radiation emitted by the light sources was collected by a lens with a focal distance F = 160 mm. Using the same lens, the light was focused on the entrance slit of the spectrometer. It should be noted that, according to the instrument ratings, spectral response of CCDs is the heterogeneous function of the wavelength.

Table 1

Spectral emissivity of tungsten for T = 2400 K

λ, μm	ε(λ,*T*)
0.3	0.468
0.325	0.468
0.35	0.467
0.375	0.466
0.4	0.464
0.425	0.462
0.45	0.459
0.475	0.455
0.5	0.45
0.525	0.446
0.55	0.441
0.575	0.436
0.6	0.431
0.625	0.428
0.65	0.424
0.6563	0.423
0.675	0.42
0.7	0.416
0.725	0.412
0.75	0.407
0.8	0.399
0.85	0.39
0.9	0.381
0.95	0.372
1	0.364
1.1	0.347
1.2	0.333
1.28	0.322
1.3	0.319
1.4	0.304
1.5	0.29
1.6	0.277
1.7	0.266
1.8	0.256
1.9	0.247
2	0.239
2.1	0.232
2.2	0.225
2.3	0.218
2.4	0.212
2.5	0.205
2.6	0.199
2.7	0.193
2.8	0.189
2.9	0.184
3	0.18
3.2	0.173

For measurements involving halogen lamp no lens was used, and the emission of lamp was directly focused on slit of spectrometer.

Emission sources and determination of the spectral response. Ribbon lamp. As standard sources of emission, both ribbon lamp and commercial halogen lamp were used. A ribbon lamp essentially consists of a tungsten ribbon wrapped in a glass shield. An electrical current passes through the thin ribbon, heating it and causing light emission (electromagnetic radiation). An emission temperature is associated with each electrical current passing through the ribbon.

The ribbon lamp used in this work was tungsten lamp with a window made of ПС-5 glass, whose schematic drawing is shown in Fig. 4.

Table 2

Absorption and transmission coefficients of ПС-5 glass

λ, nm	Absorption coefficient α(λ)	Transmission coefficient τ(λ), *d* = 1.58 mm
320	1.445	0.005
340	0.253	0.398
350	0.128	0.627
360	0.071	0.772
380	0.025	0.913
400	0.013	0.953
420	0.02	0.929
440	0.031	0.893
450	0.036	0.877
460	0.041	0.861
480	0.047	0.842
500	0.049	0.836
520	0.049	0.836
540	0.046	0.845
550	0.043	0.855
560	0.041	0.861
580	0.033	0.886
600	0.027	0.906
620	0.023	0.919
640	0.02	0.929
650	0.018	0.936
660	0.017	0.940
680	0.014	0.950
700	0.012	0.957
720	0.01	0.964
740	0.008	0.971
750	0.008	0.971
760	0.007	0.974
780	0.006	0.978
800	0.004	0.985
840	0.002	0.992
880	0.001	0.996
920	0	1
960	0	1
1000	0	1
1100	0	1
1200	0	1
1300	0	1
1400	0	1
1500	0	1
1800	0.001	0.996
2100	0.003	0.989
2400	0.006	0.978
2700	0.163	0.552
3000	0.156	0.566

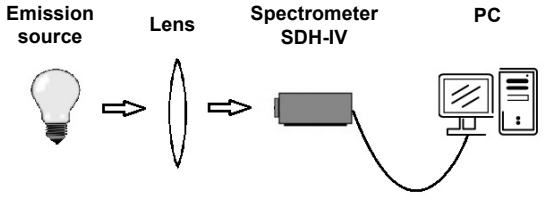

Fig. 3. Experimental setup scheme

Commercial halogen lamp. Invented by GE Lighting in 1958, the halogen lamp provides a highly efficient compact source of light that has revolutionized the world of lighting. This is also an incandescent lamp, consisting of a tungsten filament sealed in a small wrapper filled with a halogen gas such as iodine or bromine. This gas creates a reaction to avoid the evaporation of the tungsten towards the walls of the wrapper. Because the lamp must be very hot to create this reaction, the halogen lamp wrapper can be made of hard glass or fused quartz, instead of ordinary soft glass which would soften and flow too much at these temperatures. So, unlike the standard incandescent lamp, halogen lamps use a halogen gas that allows them to shine more brightly without sacrificing duration, at a smaller physical size and a lower economic cost.

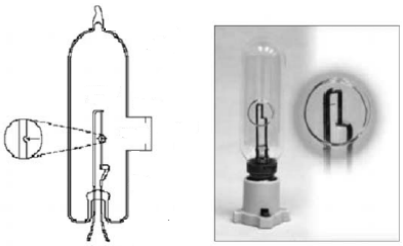

Fig. 4. Tungsten ribbon lamp

Currently there are many types of halogen lamps which are classified according to their bulb, filament and base. H4 halogen lamp is the one that has been used in this study. A schematic drawing of this kind of lamp is shown in Fig. 5.

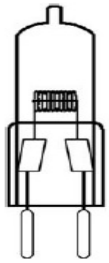

Fig.5. Schematic drawing of a H4 halogen lamp

Calibration procedure of the optical system using two emission sources: tungsten ribbon lamp and halogen lamp. On the basis of the foregoing, true value of spectral intensity for every wavelength (or intensity distribution by wavelengths) can be calculated according to the Kirchhoff's law for standard emission sources.

The supplied filament current of the ribbon lamp varied within the range 21.87–22.12 A. According to manufacturer, the brightness temperature of the tungsten filament T_b lies within the values 2176.78–2202.66 K. For calculations, the average brightness temperature T_b = 2189.22 K was used. With that in mind, from (11) and (12) true temperature of the tungsten filament was derived: T_{true} = 2410 K. Relation between brightness and true temperatures is illustrated in Fig. 6.

In case of halogen lamp, true lamp temperature is provided by manufacturer T_{true} = 2854 K, and lamp emission can be approximated to the electromagnetic radiation emitted by a blackbody.

Fig. 7 and Fig. 8 show the registered electromagnetic radiation emitted by tungsten ribbon lamp and by halogen lamp, respectively. These spectra were interpolated within the wavelength range 345–605 nm in order to smooth the dependences and take account of background noises, background emission was subtracted.

Fig. 9 depicts the blackbody spectral radiance calculated from (2) using values of true temperature obtained for tungsten ribbon lamp.

Emissivity of a tungsten ribbon was obtained from (9) using previously calculated values of blackbody spectral radiance $b(\lambda, T)$, interpolated values of tungsten emission coefficient $\varepsilon(\lambda, T)$ and transmission coefficient of lamp window glass $\tau(\lambda)$.

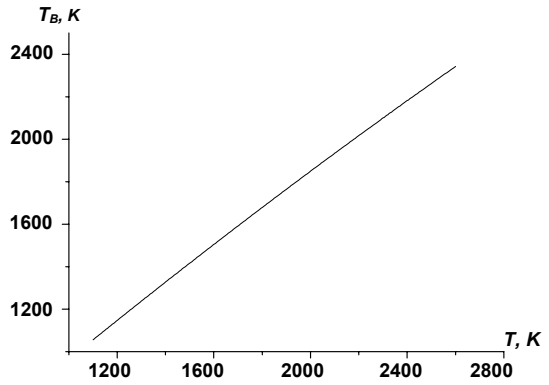

Fig. 6. Relation between brightness and true temperatures of tungsten ribbon

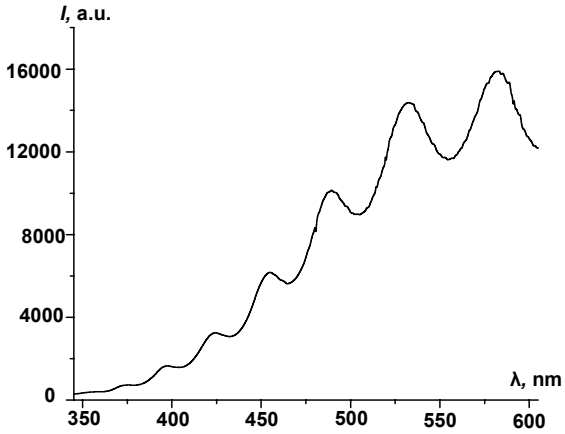

Fig. 7. Registered emission of a tungsten ribbon lamp in spectral range λ = 345-605 nm

Spectral response of spectrometer S (Fig. 10) was estimated as a ratio between tungsten emissivity and registered intensity of tungsten ribbon lamp emission.

In real laboratory experiments, it is not always reasonable to use the tungsten ribbon lamp every time for calibration of optical system prior to conduction of experiments. Therefore, application of a low-cost commercial halogen lamp would be more convenient. With that in mind, emission of a halogen lamp can be calibrated using previously obtained spectral response of the optical system. Fig. 11 shows calibrated intensity of a halogen lamp emission, calculated as a ratio of experimentally registered intensity of halogen lamp emission and spectral response obtained by using of the tungsten ribbon lamp.

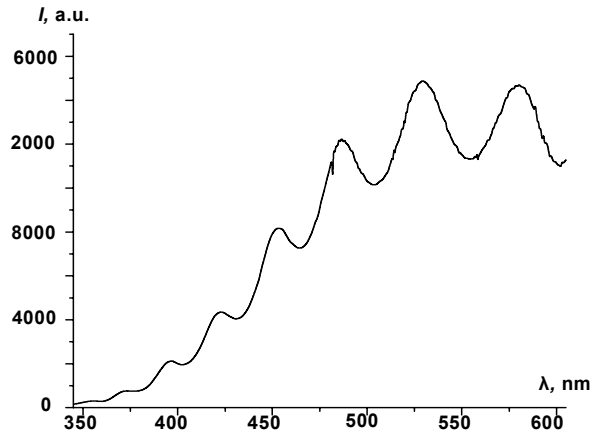

Fig. 8. Registered emission of a halogen lamp in spectral range λ = 345–605 nm

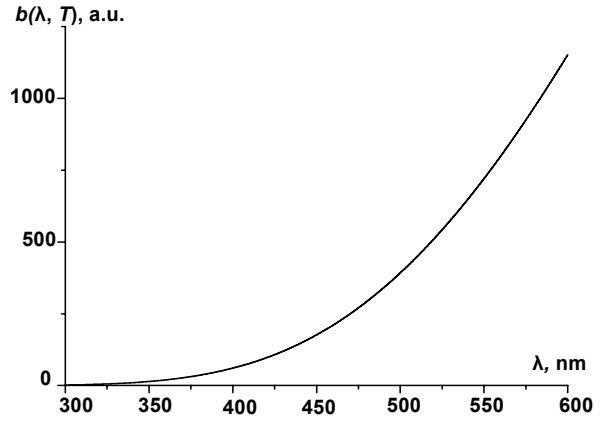

Fig. 9. Spectral radiance of blackbody at T = 2410 K calculated using tungsten ribbon lamp

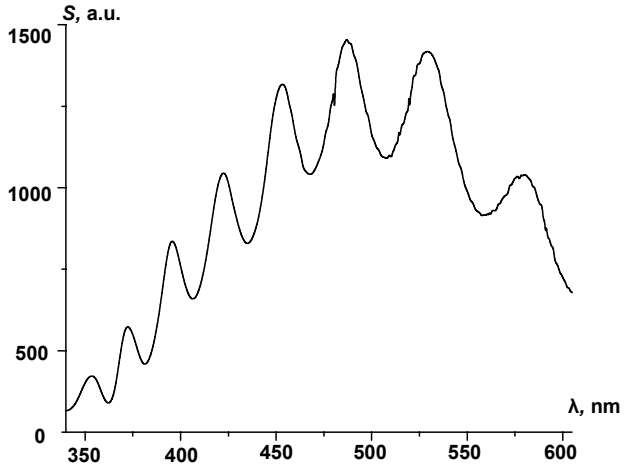

Fig. 10. Spectral response of SDH-IV spectrometer, calculated using tungsten ribbon lamp as a standard source of emission

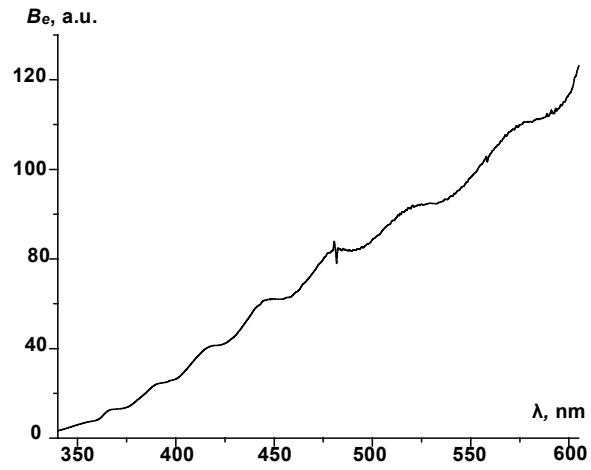

Fig. 11. Intensity of a halogen lamp emission, calibrated with previously obtained spectral response of an optical system

Conclusions. Spectral response of SDH-IV spectrometer was calculated using the tungsten ribbon lamp as a standard emission source.

Intensity of a halogen lamp emission was calibrated using this spectral response.

In summary, following procedure for evaluation of spectral response of an optical device can be recommended:

1. To set up the corresponding standard source of emission and focus its image on an entrance slit of spectral device. To determine brightness temperature T_b in accordance with the current.

2. To determine true temperature T_{true} using (11,12).

3. To calculate spectral radiance of blackbody $b(\lambda, T)$ for T_{true} using Planck's law (1,2).

4. To determine emissivity of a standard emission source $B_e(\lambda,T)$ at T_{true}, using tables of tungsten emission coefficient $\varepsilon(\lambda,T)$ dependence on wavelength and transmission coefficient of the lamp window glass $\tau(\lambda)$.

5. To measure spectral response of spectral device to emission of a standard light source as function of wavelength $I(\lambda)$.

6. To determine spectral sensitivity of spectral device as ratio $I(\lambda)/B_e(\lambda,T)$.

REFERENCES

1. *Barschevskiy B. U.* Kvantovo-opticheskie yavleniya / B. U. Barschevskiy. – Moskwa : Vissh. shkola, 1982.

2. *Hartmann J.* High-Temperature Measurement Techniques for the Application in Photometry, Radiometry and Thermometry / J. Hartmann // Phys. Rep., 2009. – Vol. 469. – P. 205–269.

3. *Primary* Sources for Use in Radiometry, in Optical Radiometry / J. Hollandt, J. Seidel, A. Migdall, M. Ware. – Amsterdam : Elsevier Academic Press, 2005.

4. *Veklich A. N.* Determination of spectral sensitivity of optical devices : Methodical guidelines for students of Faculty of Radiophys. / A. N. Veklich, I. L. Babich. – Kyiv: National Taras Shevchenko University of Kyiv, Faculty of Radiophys., 2006.

5. *Yubero C.* Using a halogen lamp to calibrate an optical system for UV-VIS radiation detection / C. Yubero, C. Garcia, D. Calzada // Optica Applicata, 2008. – Vol. 38, № 3. – P. 353–363.

Submitted on 04.08.16

Т. Тменова, асп.,
А. Веклич, д-р фіз.-мат. наук,
В. Борецький, канд. фіз.-мат. наук,
кафедра фізичної електроніки,
факультет радіофізики, електроніки та комп'ютерних систем,
Київський національний університет імені Тараса Шевченка, Київ

КАЛІБРУВАННЯ СПЕКТРАЛЬНОЇ ЧУТЛИВОСТІ СПЕКТРОМЕТРА SDH-IV

Упродовж останніх років низькотемпературна плазма знаходить все більшого застосування в наукових та технологічних сферах, при цьому, найбільш поширеним методом для діагностики такої плазми є оптична емісійна спектроскопія (ОЕС). Зазвичай найпростіша оптична система для визначення та дослідження параметрів плазми складається зі спектрометра чи монохроматора, оптичного датчика та оптоволокна або системи лінз. Усі елементи системи мають бути попередньо відкаліброваними з метою коригування різниці у спектральних відгуках кожного з них. Запропоновано методичні вказівки для визначення та калібрування спектральної чутливості оптичних приладів на прикладі розрахунків спектрального відгуку високоапертурного компактного спектрометра SDH-IV у діапазоні довжин хвиль від 345 до 605 нм. Як еталонні джерела випромінювання для калібрування спектра використано вольфрамову стрічкову і галогенову лампи.

Ключові слова: спектральна чутливість, спектрометр, вольфрамова стрічкова лампа, галогенова лампа, чорне тіло, довжина хвилі, коефіцієнт випромінювання.

Т. Тменова, асп.,
А. Веклич, д-р физ.-мат. наук,
В. Борецкий, канд. физ.-мат. наук,
кафедра физической электроники,
факультет радиофизики, электроники и компьютерных систем,
Киевский национальный университет имени Тараса Шевченко, Киев

КАЛИБРОВКА СПЕКТРАЛЬНОЙ ЧУВСТВИТЕЛЬНОСТИ СПЕКТРОМЕТРА SDH-IV

На протяжении последних лет низкотемпературная плазма находит всё большее применение в науке и технике, при этом, наиболее распространённым методом диагностики такой плазмы является оптическая эмиссионная спектроскопия (ОЭС). Простейшая оптическая система для определения и исследования параметров плазмы состоит из спектрометра или монохроматора, оптического датчика и оптоволокна или системы линз. С целью корректировки разницы спектральных откликов каждого из элементов оптической системы она должна быть предварительно откалибрована. Предлагаются методические рекомендации для определения и калибровки спектральной чувствительности оптических приборов, что показано на примере расчёта спектрального отклика высокоапертурного компактного спектрометра SDH-IV в диапазоне длин волн от 345 до 605 нм. В качестве эталонных источников излучения для калибровки спектра использованы вольфрамовая ленточная и галогенная лампы.

Ключевые слова: спектральная чувствительность, спектрометр, вольфрамовая ленточная лампа, галогенная лампа, черное тело, длина волны, коэффициент излучения.

UDC 621.315.592

O. Khylko, Stud.,
Department of Theoretical Foundation of High Technologies,
Institute of High Technologies,
Taras Shevchenko National University of Kyiv, Kyiv

SCATTERING OF SURFACE PLASMON POLARITON BY TWO-DIMENSIONAL SEMICONDUCTOR NANOSTRIPE. EFFECTIVE SUSCEPTIBILITY OF TWO-DIMENSIONAL NANOSTRIPE

Local-field intensity calculation of infinity-long nanostripe on the surface with excited surface plasmons is proposed. Calculation is performed using Green's function method in the frame of concept of effective susceptibility using near-field approximation. The method of analytically calculation of effective susceptibility of two-dimension nanostripe was considered. The main characteristic of the proposed approach is maximal using analytical calculations. Obtained results are universal and could be able to calculate local-field intensity of any low-dimension rectangular nanostripe with any aspect ratio or material of nanostripe or surface.

Keywords: surface plasmon polaritons, surface waves scattering, effective susceptibility, semiconductor nanostripe.

Introduction. Surface plasmon polaritons (SPPs) are electromagnetic surface waves propagating along metal-dielectric interfaces with their intensity maximum in the surface and exponential decaying perpendicular to the surface [5]. In recent years SPP propagating features has been intensively studied. Theoretical research of SPP scattering [1,3] shows how to calculate scattered field intensity far from the scatterer. But sometimes we need to know local-field distribution near the scatterer. Of course, we can use numerical methods such as FDTD method [2], but it requires huge computational resources. In this article theoretical study of SPP scattering by infinitely long nanostripe using Green's Function method is presented. The main characteristic of the proposing approach is maximal using analytical calculations. Calculation is performed using concept of effective susceptibility [6, 7], which is a characteristics of both nano-object and material and it is a linear response on external field.

Effective susceptibility of infinitely-long nanostripe. The system under consideration represents an infinitely-long homogeneous nanostripe (Fig. 1) placed along y-axis with susceptibility χ_p placed on the surface with dielectric constant ε_1 (in the region $z<0$) and upper semi space has dielectric constant ε_2 (in the region $z>0$). Of cause, considered nanostripe has determined length, but we assume that length of nanostripe much greater than wave length and SPP width. The response of that system on external field can be found using Lippmann-Schwinger equation in the frame of concept of effective susceptibility [6]:

$$E_i(\mathbf{R}) = E_i^0(\mathbf{R}) + k_0^2 \int_V d\mathbf{R}' G_{ij}(\mathbf{R},\mathbf{R}') \chi_{jk}(\mathbf{R}') E_k^0(\mathbf{R}'), \quad (1)$$

$$G_{ji}^D(\mathbf{R},\mathbf{R}') = \frac{1}{4\pi k_0^2 R^3}\left[-\delta_{ij} + 3\frac{R_i R_j}{R^2}\right], \quad (2)$$

$$G_{ji}^I(\mathbf{R},\mathbf{R}'') = \frac{\varepsilon_2-\varepsilon_1}{\varepsilon_2+\varepsilon_1}\frac{1}{4\pi k_0^2 R^3}\left[-\delta_{ij} + 3\frac{R_i R_j}{R^2}\right], \quad (3)$$

where $G_{ij}(\mathbf{R},\mathbf{R}')$ is the sum of direct (2) and indirect (3) part of Green's function with near-field approximation [7], $\mathbf{R}'' = \{x', y', -z'\}$ and $R = \sqrt{(x-x')^2 + (y-y')^2 + (z+z')^2}$. And effective susceptibility is:

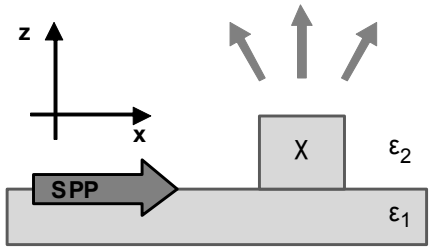

Fig. 1. Schematic of the scattering system: an external SPP propagating along the dielectric-metal interface (x-axis) is scattered by a rectangular nanostripe

$$\chi_{ij}(\mathbf{R}) = \frac{\chi_{ij}(\mathbf{R})}{\delta_{ij} - S_{ij}(\mathbf{R})}, \quad (4)$$

$$S_{ij}(\mathbf{R}) = k_0^2 \int_V d\mathbf{R}' G_{ij}(\mathbf{R},\mathbf{R}') \chi_{jk}(\mathbf{R}'), \quad (5)$$

Taking into account that nanostripe is infinitely-long along y-axis and homogeneous let us integrate eq. (5):

$$S_{ij}(\mathbf{R}) = \chi_{jk} k_0^2 \int_{s'} ds' \int_{-\infty}^{+\infty} dy' G_{ij}(\mathbf{R},\mathbf{R}'), \quad (6)$$

$$S_{ij}(\mathbf{R}) = \chi_{jk} k_0^2 \int_s ds' G_{ij}^{2D}(x,z,x',z'), \quad (7)$$

where $G_{ij}^{2D}(x,z,x',z')$ is Green's function (photon propagator) of two-dimensional system with an interface between two media and it is

$$G_{ij}^{2D}(x,z,x',z') = \frac{1}{2\pi k_0^2} \times \begin{bmatrix} g_{11} & 0 & g_{13} \\ 0 & 0 & 0 \\ g_{31} & 0 & g_{33} \end{bmatrix}, \quad (8)$$

$$g_{11} = \frac{(x-x_0)^2 - (z-z_0)^2}{((x-x')^2 + (z-z')^2)^2} + \kappa \frac{(x-x_0)^2 - (z+z_0)^2}{((x-x')^2 + (z+z')^2)^2}, \quad (9)$$

$$g_{13} = \frac{2(x-x_0)(z-z_0)}{((x-x')^2 + (z-z')^2)^2} - \kappa \frac{2(x-x_0)(z+z_0)}{((x-x')^2 + (z+z')^2)^2}, \quad (10)$$

$$g_{31} = \frac{2(x-x_0)(z-z_0)}{((x-x')^2 + (z-z')^2)^2} + \kappa \frac{2(x-x_0)(z+z_0)}{((x-x')^2 + (z+z')^2)^2}, \quad (11)$$

$$g_{33} = -\frac{(x-x_0)^2 - (z-z_0)^2}{((x-x')^2 + (z-z')^2)^2} + \kappa \frac{(x-x_0)^2 - (z+z_0)^2}{((x-x')^2 + (z+z')^2)^2}, \quad (12)$$

where $\kappa = (\varepsilon_2 - \varepsilon_1)/(\varepsilon_2 + \varepsilon_1)$. After all, effective susceptibility can be easily analytically calculated.

$$\chi_{ij}(\mathbf{R}) = \frac{\chi_{ij}}{1 - c_{11}\chi_{11} - c_{33}\chi_{33} - c_{13}c_{31}\chi_{11}\chi_{33} + c_{11}c_{33}\chi_{11}\chi_{33}} \times \times \begin{bmatrix} 1 - c_{33}\chi_{33} & 0 & c_{13}\chi_{11} \\ 0 & 1 & 0 \\ c_{31}\chi_{33} & 0 & 1 - c_{11}\chi_{11} \end{bmatrix} \quad (13)$$

$$c_{11}(x,z) = \frac{1}{2\pi}\left(\begin{array}{l} -\arctan\left(\frac{z-z_1}{x-x_1}\right) + \arctan\left(\frac{z-z_1}{x-x_2}\right) + \\ +\arctan\left(\frac{z-z_2}{x-x_1}\right) - \arctan\left(\frac{z-z_2}{x-x_2}\right) + \\ +\kappa\left(\arctan\left(\frac{z+z_1}{x-x_1}\right) - \arctan\left(\frac{z+z_1}{x-x_2}\right)\right) - \\ -\kappa\left(\arctan\left(\frac{z+z_2}{x-x_1}\right) - \arctan\left(\frac{z+z_2}{x-x_2}\right)\right) \end{array} \right) \quad (14)$$

$$c_{13}(x,z) = \frac{1}{4\pi}\left(\begin{array}{l} -\ln\left((x-x_1)^2 + (z-z_1)^2\right) + \ln\left((x-x_2)^2 + (z-z_1)^2\right) + \\ +\ln\left((x-x_1)^2 + (z-z_2)^2\right) - \ln\left((x-x_2)^2 + (z-z_2)^2\right) - \\ -\kappa\left(\ln\left((x-x_1)^2 + (z+z_1)^2\right) - \ln\left((x-x_2)^2 + (z+z_1)^2\right)\right) + \\ +\kappa\left(\ln\left((x-x_1)^2 + (z+z_2)^2\right) - \ln\left((x-x_2)^2 + (z+z_2)^2\right)\right) \end{array} \right) \quad (15)$$

$$c_{31}(x,z) = \frac{1}{4\pi}\left(\begin{array}{l} -\ln\left((x-x_1)^2 + (z-z_1)^2\right) + \ln\left((x-x_2)^2 + (z-z_1)^2\right) + \\ +\ln\left((x-x_1)^2 + (z-z_2)^2\right) - \ln\left((x-x_2)^2 + (z-z_2)^2\right) + \\ +\kappa\left(\ln\left((x-x_1)^2 + (z+z_1)^2\right) - \ln\left((x-x_2)^2 + (z+z_1)^2\right)\right) - \\ -\kappa\left(\ln\left((x-x_1)^2 + (z+z_2)^2\right) - \ln\left((x-x_2)^2 + (z+z_2)^2\right)\right) \end{array} \right) \quad (16)$$

$$c_{33}(x,z) = \frac{1}{2\pi}\left(\begin{array}{l} \arctan\left(\frac{z-z_1}{x-x_1}\right) - \arctan\left(\frac{z-z_1}{x-x_2}\right) - \\ -\arctan\left(\frac{z-z_2}{x-x_1}\right) + \arctan\left(\frac{z-z_2}{x-x_2}\right) + \\ +\kappa\left(\arctan\left(\frac{z+z_1}{x-x_1}\right) - \arctan\left(\frac{z+z_1}{x-x_2}\right)\right) \\ -\kappa\left(\arctan\left(\frac{z+z_2}{x-x_1}\right) - \arctan\left(\frac{z+z_2}{x-x_2}\right)\right) \end{array} \right) \quad (17)$$

Here, x_1, x_2, z_1, z_2 are coordinates of the sides of the nanostripe (Fig.2.). In addition, it should be noted that $\chi_{yy} = \chi_{yy}$ which corresponds to a bulk material.

Numerical calculation. Let us consider the case when external field is surface plasmon polariton (SPP) that propagating along x-direction and perpendicular to the nanostripe that leads to SPP's scattering. Using eq. (1) we can easily calculate response of nanostripe on the SPP. In this case external field is [4]:

$$E_i^0(\mathbf{R}) = \exp(ik_{spp}x - ik_{spp}Z_s z) \times [Z_s, 0, 1], \quad (18)$$

where SPP's wave number is $k_{spp} = (\omega/c)\sqrt{\varepsilon_1\varepsilon_2/(\varepsilon_1 + \varepsilon_2)}$ and $Z_s = -i\sqrt{\varepsilon_2/(-\varepsilon_1)}$. Let us calculate local-field intensity distribution at the nanostripe. For example, SPP propagating along gold-air interface with $\varepsilon_1 = -20.13 + 0.29i$ (for $\lambda = 632$ nm) and $\varepsilon_2 = 1$ respectively.

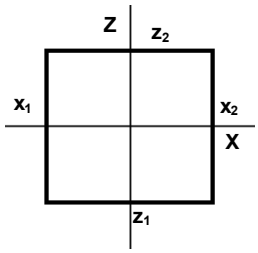

Fig. 2. The coordinates of the sides of the nanostrpipe

For stripe were used axial dimensions: $h_x = h_z = 100$nm, h_y much greater than wave length and SPP width, and material is silicon $\chi_p = 14.045 + 0.008i$. The results of numerical calculations of local-field intensity are presented on Fig. 2.

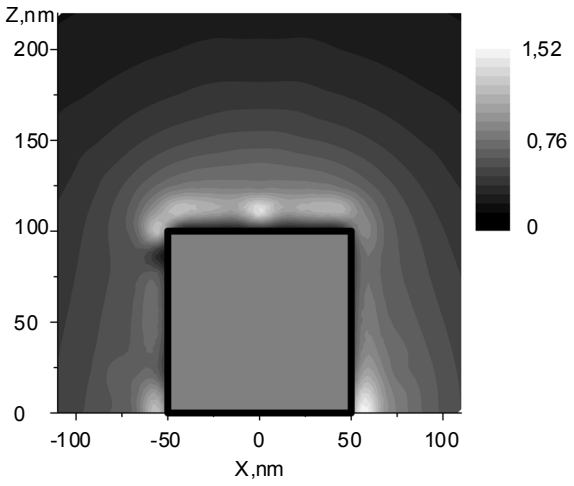

Fig. 3. Local-field intensity distribution at the nanostripe with excited SPP. Density axis represent intensity (arbitrary units) and it changes from black to white color

One can see the local-field intensity distribution is very inhomogeneous with “hot spots” – local-field enhancement on the stripe surface.

Conclusions. The method of analytical calculation of effective susceptibility of infinity-long rectangular nanostripe and local-field intensity distribution is proposed. Developed approach is universal and could be able to find local-field distribution for any low-dimension nanostripe with any aspect ratio or material of the nanostripe or surface.

REFERENCES

1. *Bozhevolnyi S. I.* Vectorial model for multiple scattering by surface nanoparticles via surface polariton-polariton interactions / S. I. Bozhevolnyi, T. Sondergaard // Phys. Rev. B67, 2003. – 165405.

2. *Sharp* plasmonic resonance on gold gratings in amplitude and phase domains / S. Chen, G. Li, W. Wong et al. // App. Optics, 2012. – Vol. 51, № 36. – P. 8563–8566.

3. *Surface* plasmon polariton scattering by finite-size nanoparticles / A. B. Evlyukhin, S. I. Bozhevolnyi, G. Brucoli et al. // Phys. Rev. B76, 2007. – 075426.

4. *Evlyukhin A.* Surface plasmon polariton scattering by small ellipsoid particles / A. Evlyukhin, S. Bozhevolnyi // Surface Sci., 2005. – Vol. 590. – P. 173–180.

5. *Heinz Raether*. Surface plasmons on smooth and rough surfaces and on gratings / Heinz Rether. – Berlin : Springer, 1988.

6. *Lozovski V*. Near-field images calculations of exciton clouds interacting with defects under semiconductor surface / V. Lozovski, O. Khylko // Quantum Matter, 2014. – Vol. 3. – P. 1–14.

7. *Lozovski V*. Near-field visualization of dynamical processes of semiconductor surface / V. Lozovski, V. Vasilenko // Ultramicroscopy, 2008. – Vol. 109. – P. 39–43.

Submitted on 24.10.15

О. Хилько, студ.,
кафедра теоретичних основ високих технологій,
Інститут високих технологій,
Київський національний університет імені Тараса Шевченка, Київ

РОЗСІЯННЯ ПОВЕРХНЕВОГО ПЛАЗМОН-ПОЛЯРИТОНУ НА ДВОВИМІРНІЙ НАПІВПРОВІДНИКОВІЙ НАНОСМУЖЦІ. ЕФЕКТИВНА СПРИЙНЯТЛИВІСТЬ ДВОВИМІРНОЇ НАНОСМУЖКИ

Запропоновано метод розрахунку інтенсивності локального поля навколо нескінченно довгої наносмужки на поверхні зі збудженим поверхневим плазмоном. Розрахунок проведено за допомогою методу функцій Гріна в межах концепції ефективної сприйнятливості з використанням наближення ближнього поля. Розглянуто метод аналітичного розрахунку ефективної сприйнятливості двовимірної наносмужки. Основною характеристикою запропонованого підходу є максимальне використання аналітичних розрахунків. Отримані результати універсальні, і тому їх можна використати для обчислення інтенсивності локального поля навколо будь-якої низькорозмірної прямокутної наносмужки, з будь-яким співвідношенням сторін та будь-яким матеріалом наносмужки чи поверхні.

Ключові слова: поверхневий плазмон поляритон, розсіяння поверхневих хвиль, ефективна сприйнятливість, напівпровідникова наносмужка.

А. Хилько, студ.,
кафедра теоретических основ высоких технологий,
Институт высоких технологий,
Киевский национальный университет имени Тараса Шевченко, Киев

РАССЕЯНИЕ ПОВЕРХНОСТНОГО ПЛАЗМОН-ПОЛЯРИТОНА НА ДВУХМЕРНОЙ ПОЛУПРОВОДНИКОВОЙ НАНОСПОЛОСКЕ. ЭФФЕКТИВНАЯ ВОСПРИИМЧИВОСТЬ ДВУХМЕРНОЙ НАНОПОЛОСКИ

Предложен метод расчета интенсивности локального поля вокруг бесконечно долгой нанополоски на поверхности с возбужденным поверхностным плазмоном. Расчет производится с помощью метода функций Грина в рамках концепции эффективной восприимчивости, используя приближение ближнего поля. Рассмотрен метод аналитического расчета эффективной восприимчивости двухмерной нанополоски. Основной характеристикой предложенного подхода является максимальное использование аналитических расчетов. Полученные результаты являются универсальными и могут быть использованы для вычисления интенсивности локального поля вокруг любой низкоразмерной прямоугольной нанополоски, с любым соотношением сторон и любым материалом нанополоски или поверхности.

Ключевые слова: поверхностный плазмон поляритон, рассеивание поверхностных волн, эффективная восприимчивость, полупроводниковая нанополоска.

Наукове видання

ВІСНИК

КИЇВСЬКОГО НАЦІОНАЛЬНОГО УНІВЕРСИТЕТУ ІМЕНІ ТАРАСА ШЕВЧЕНКА

РАДІОФІЗИКА ТА ЕЛЕКТРОНІКА

Випуск 1(24)

Статті подано в авторській редакції

Оригінал-макет виготовлено ВПЦ "Київський університет"

Формат 60x84$^{1/8}$. Ум. друк. арк. 7,5. Наклад 300. Зам. № 216-7993.
Вид. № Рф1. Гарнітура Arial. Папір офсетний. Друк офсетний.
Підписано до друку 23.01.17

Видавець і виготовлювач
Видавничо-поліграфічний центр "Київський університет"
01601, Київ, б-р Т. Шевченка, 14, кімн. 43
☎ (38044) 239 3222; (38044) 239 3172; тел./факс (38044) 239 3128
e-mail: vpc@univ.kiev.ua
http: vpc.univ.kiev.ua
Свідоцтво суб'єкта видавничої справи ДК № 1103 від 31.10.02